Department of Metallurgy & Materials Science

1-9064

CONTRACT REPORT NO. OSU81-00274

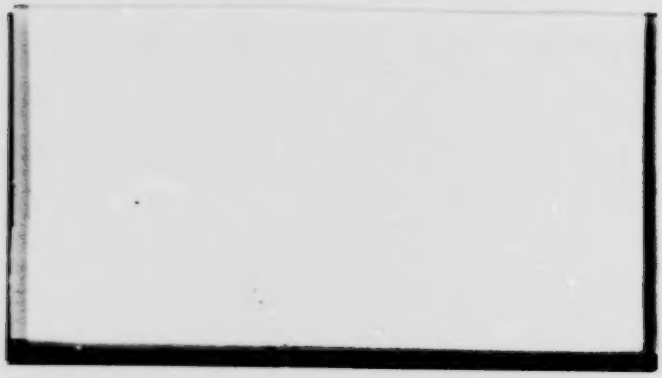

University of Toronto

MICROMEDIA
OCT 2 5 1984

151 pp

WETTING BEHAVIOUR OF MOLTEN $PbCl_2$-ALKALI CHLORIDE MIXTURES

BY

TORSTEIN ARNFINN UTIGARD

ABSTRACT

A high temperature X-ray fluoroscopy unit was designed and built for the purpose of carrying out contact angle and surface/interfacial tension measurements. The contact angles formed between liquid $PbCl_2$ - alkali chloride mixtures and graphite, alumina, quartz, zirconium oxide, boron nitride and inconel were measured. Alumina, quartz and inconel were completely wetted by all the salt mixtures used in this study, while the contact angles on graphite were between 120° to 140° when an argon atmosphere as used. Introduction of dry chlorine gas did not affect the contact angle on graphite while the introduction of air or dry air lead to a rapid decrease in the contact angle both on graphite and amorphous carbon.

Asymmetrical sessile drops were formed on the ZrO_2 and BN plaques with contact angles ranging from 20° to 105°. The surface roughness and porosity were assumed to be the main reasons for the contact angle hysteresis.

The thermodynamic status of the contact angle has been discussed and it was concluded that the non-ideality of real surfaces is the main reason for the discrepancy in the contact angle measurements between different laboratories.

Difficulties were encountered in the surface tension measurements due to the diffuse outline of the drop profile caused by the penetration properties of X-ray photons. The surface tension was measured for two ternary mixtures containing 40 mol % $PbCl_2$.

TABLE OF CONTENTS

		Page
ABSTRACT		
CHAPTER 1:	INTRODUCTION	1
	1.1 Surface and Interfacial Energy in Metallurgical Processes	4
	1.2 Interfacial Hydrodynamics	4
	1.3 Importance of Wetting in Metallurgical Processes	5
CHAPTER 2:	METHODS FOR MEASURING CONTACT ANGLE	8
	2.1 Sessile Drop and Adhering Bubble	9
	2.1.1 Theoretical considerations of the sessile drop	12
	2.1.2 Measurements of contact angle from photographs	17
	2.1.3 Errors due to asymmetry in the drop profile	18
	2.1.4 Drop size	19
	2.2 Wilhelmy-Gravitational Method	19
	2.2.1 Advantages and disadvantages of the Wilhelmy technique	23
	2.3 Capillary Rise at a Vertical Plate	24
	2.4 Choice of Experimental Technique	27
	2.5 Fundamentals of Radiographic Imaging	27
CHAPTER 3:	THEORY	29
	3.1 Contact Angle and Surface Tension	29
	3.2 Young Equation and Laplace Equation	30
	3.3 Limitations of the Classical Theory of Capillarity	33

		Page
3.4	Rough and Heterogeneous Surfaces	36
3.5	Methods of Estimating Surface Tension of Solids	39
3.6	Surface Tension of Molten Salt	48
3.6.1	Surface tension of mixtures	49
3.7	X-Ray Radiography	54
CHAPTER 4:	EXPERIMENTAL SECTION	57
4.1	Apparatus	57
4.1.1	Furnace	57
4.1.2	Container for sessile drop	64
4.1.3	X-ray unit	64
4.2	The Image Intensifier Tube	66
4.3	Effect of the Photographic Emulsion on Resolution	68
4.4	Error Sources	69
4.5	Preparation of Graphite Basal Support	70
4.6	Preparation of Al_2O_3, SiO_2, ZrO_2 and BN Plaques	73
4.7	Purification of Salt Mixtures	75
4.8	Experimental Procedure	76
CHAPTER 5:	RESULTS	80
5.1	Contact Angle Measurements on Graphite	80
5.2	Contact Angle Measurements on Al_2O_3, SiO_2, ZrO_2, BN and Inconel	99
5.3	Surface Tension Measurements	103

		Page
CHAPTER 6:	DISCUSSION	111
	6.1 Contact Angle Measurements on Graphite	111
	6.2 Effect of Time on the Contact Angle	117
	6.2.1 $PbCl_2$-KCl and $PbCl_2$-NaCl binary system	119
	6.2.2 $PbCl_2$-KCl-NaCl and $PbCl_2$-KCl-LiCl mixtures	119
	6.3 Surface Tension of Graphite	120
	6.4 Contact Angle on Al_2O_3, SiO_2, ZrO_2, BN and Inconel	121
	6.5 Surface Tension	123
	6.6 Error Sources due to Image Recording and Analysis	125
CHAPTER 7:	CONCLUSIONS	127
Appendix ONE:	Radiation intensity across a spherical drop	130
Appendix TWO:	Effect of focal spot on the intensity distribution	131
Appendix THREE:	Specifications for X-ray anode	132
Appendix FOUR:	Surface characteristics of two different graphite disks and of a polycrystalline alumina (Al_2O_3) disk	133
Appendix FIVE:	Stated purity and analysis of chemicals	134
Appendix SIX:	Ternary phase diagram of $PbCl_2$-KCl-LiCl and $PbCl_2$-KCl-NaCl(3)	135
Appendix SEVEN:	Density of two ternary mixtures (136)	136
Appendix EIGHT:	Vapour pressure of pure and mixed chlorides	137
Appendix NINE:	Effect of the gas atmosphere on the wetting of graphite	138
REFERENCES		140

CHAPTER 1

INTRODUCTION

The objective of the present investigation was to study some aspects involved in the development of a process to produce lead from lead chloride. Presently, lead smelters have problems in meeting environmental regulations with regards to sulphur oxide and lead pollution (1,2). As an alternative method for the production of lead, fused salt electrolysis of $PbCl_2$ has been reported (1,3,4) to be promising.

Molten lead chloride by itself is not a suitable electrolyte because it dissolves lead (5), has a relatively high melting point (501°C) and vapour pressure (3,6). It is therefore necessary to combine $PbCl_2$ with alkali metal chlorides to reduce the melting point of the electrolyte, to reduce the fuming and to reduce the dissolution loss of lead. To produce lead in the molten state, electrolysis must be conducted above its melting point (327°C) and thus a suitable operating temperature range might be from 400 to 450°C.

An electrolyte consisting of $PbCl_2$, KCl, NaCl and LiCl seems to be the most suitable with respect to the chemical and the physical properties (1,3). Mixtures of $PbCl_2$ - LiCl or $PbCl_2$ - NaCl show better conductivity than a mixture of $PbCl_2$ - KCl, but additions of KCl reduce the volatilization loss of lead chloride more than the corresponding additions of NaCl or LiCl. This is assumed to

be due to the formation of the $PbCl_4^{2-}$ complex which will be more stable in mixtures containing KCl (7,8,9). The investigations carried out by Wong and Haver (1) showed that the best overall electrolyte composition was in the ternary system $PbCl_2$ - KCl - LiCl. One main problem with this system is that LiCl is very hygroscopic. An electrolyte consisting of $PbCl_2$ - KCl - NaCl does not lead to this problem, but it has the disadvantage of having a slightly lower molar conductivity.

In the literature, surface tension values of pure $PbCl_2$ (10,11), KCl (12,13,14), NaCl (14,15,16) and LiCl (17,18) can be found and also values of the different binary systems have been published (15,17,11,12,19). However, no reported surface tension values exist for the $PbCl_2$-alkali chloride ternary systems. Similarly, a literature search on these systems indicated that no published data exist on the wetting properties and contact angle measurements.

Because of this lack of information, it was decided to study the wetting properties of the $PbCl_2$-alkali chloride binary and ternary systems. Contact angle measurements of potential fused salt electrolytes on different solids such as alumina, quartz and graphite, have therefore been carried out. Surface tension values of some of these salt mixtures were simultaneously found with the use of the sessile drop method.

The information obtained from this investigation is also expected to be of value in understanding and developing other processes where metal is produced by electrolysis of its halide.

Examples of such processes are the production of Mg from $MgCl_2$ (20), the production of Zr from $ZrCl_4$ (21) and the production of Al from $AlCl_3$ (22).

Likewise, liquid/gas surface tensions affect froth stability while liquid/liquid interfacial tensions play an important role when a second liquid phase, such as oil, is used in the flotation process. A factor which is beginning to receive considerable attention in flotation is the "induction time" required for an interface to reach equilibrium. This induction time affects the strength of a bubble/particle contact as a function of bubble age and it also affects froth and oil/water emulsion stability.

When a solid particle, under the action of gravity, approaches an interface between two liquids, or between a gas and liquid, it may either take up an equilibrium position at the interface, or pass through, depending on the size of the particle, the densities of both particle and fluid phases, the interfacial tension, and the contact angle at the fluid/fluid/solid boundary. If the density of the particle is intermediate to the densities of the two fluids, the particle will take up an equilibrium position at the interface. If, however, the particle is either denser or less dense than both fluids, it will be found that particles smaller than a certain size take up a position at the interface, whereas particles larger than this critical size cannot be supported by the interface.

Systems of this kind are extremely important in flotation of minerals, and in emulsions stabilized by solid particles. Especially in flotation, the problem of the critical size for floatability of a particle plays an essential role.

1.1 Surface and Interfacial Energy in Metallurgical Processes

Surface and interfacial energies are important in most metallurgical and chemical processes. Wherever chemical or physical reactions occur between two phases the energy of the interface between them is an important factor because it determines in part, the size and the shape of the interface. The surface tension γ is defined by

$$\gamma = \left(\frac{\partial F}{\partial A}\right)_{T,P} \tag{1.1}$$

where A is the surface area and F is the free energy.

In pyrometallurgical processes, gas/liquid surface tension and liquid/liquid interfacial tension are both important. The relative magnitude of these two interfacial tensions influences slag/metal emulsion and slag/foam stability, and thus greatly affect reaction rates between slags, metals and gases (23,24). They also influence metal losses in slag due to physical entrapment and emulsion formation (25,26).

In the field of the froth flotation, the solid/gas surface tension affects the willingness of a solid particle to adhere to a gas bubble and hence it affects the ability of any mineral to be floated.

1.2 Interfacial Hydrodynamics

Interfacial phenomena have no effect on the thermodynamic equilibria between metals, slags and gases, but they may exert profound effects on the rates of reactions which occur across interfaces involving these phases (23,27). There are in principle two ways in

which surface active materials may influence the rates of reactions occurring across interfaces (28,29). Non-reacting surface active solutes may tend to keep reactants which are less surface active out of the interface and so retard reaction. They do this by raising the free energy of the reactants of the interface and thereby introducing an additional (chemical) resistance term in the rate equation. Surface active solutes may either slow down or increase mass transfer rates across the interface because of their effects on surface tension.

Interfacial phenomena may even promote spontaneous flow where potential energy of unequilibrated phases is converted into the kinetic energy of fluid motion. An example of such flow promotion is the Marangoni effect of "interfacial turbulence" (24,29), and often violent convection accompanying the transfer of heat and mass across a fluid interface. Interfacial turbulence may also upset the circulation within metal drops falling through salts and slags (23). The presence of surfactants may also decrease the rate of fall of metal drops by decreasing or even suppressing internal circulation (28). The rate of mass transfer into or out of the drop will be decreased by this decrease in circulation which has the effect of reducing the overall rate of reaction.

1.3 Importance of Wetting in Metallurgical Processes

The conditions that determine wetting and spreading of a liquid on a solid are not only of basic scientific interest but also of importance in understanding the development of a metal/metal bond

during welding, soldering and brazing, glass/metal bonds in protective coatings on metals, formation of metal/fibre and powder composite materials (30,31,32,33). The wetting of an electrode by the fused electrolyte during electrolysis and formation of gas products, is another important industrial aspect. The well known anode effect, which occurs during electrolysis of aluminium, is a phenomena where the wetting properties play an important role (34,35).

When a body comes into contact with a liquid, spontaneous impregnation can occur if the process is accompanied by a loss of free energy by the porous body - impregnating liquid system. During the advance of the liquid front in the porous body, the area of the liquid-gas interface remains practically constant. The only change during impregnation is that the solid-gas interface is replaced by the solid-liquid interface. The condition for impregnation then becomes

$$\gamma_{SL} - \gamma_{SV} < 0 \qquad (1.2)$$

γ_{SL}: solid-liquid interfacial tension

γ_{SV}: solid-vapour surface tension

Due to the difficulty and uncertainty of a theoretical estimation and experimental determination of these quantities, it is preferable to exclude them from the criterion of impregnability and replace them by quantities accessible to measurement. This is done by making use of Young's equation:

$$\gamma_{LV} \cos\theta = \gamma_{SV} - \gamma_{SL} \qquad (1.3)$$

where θ is the contact angle measured from the liquid phase side. The condition for spontaneous impregnation is then written in the form

$$\cos\theta > 0 \quad \text{or} \quad \theta < 90° \tag{1.4}$$

Thus, the sign of the cosine of the contact angle determines impregnation. Spontaneous impregnation is only possible for $\theta<90°$. It is however necessary to bear in mind the contact-angle hysteresis (36). A measured contact angle is not necessarily the same equilibrium contact angle as the one used in equation (1.4). In estimating the rate of impregnation, the advancing contact angle should be used. This advancing contact angle is always larger than Young's equilibrium contact angle if hysteresis occurs.

CHAPTER 2

METHODS FOR MEASURING CONTACT ANGLE

Surface tension of liquids can be measured by many methods and an investigator can choose the method which suits his needs best, with regards to accuracy, convenience, speed, cost, etc. Some of these techniques are also applicable to the measurement of liquid/liquid interfacial energies simply by replacing the gas phase with a second liquid phase. The most common methods for measurement of surface tension are:

Capillary rise method (37,38)

Maximum bubble pressure method (11,17,39)

Levitation technique (47,48)

Drop weight method (49,50)

Sessile drop method (43,44,45,46)

Pendant drop method (51,52)

Detachment methods (40,41,42)

These methods are all well described in the literature, and surface tension values obtained by different investigators correspond fairly well with each other. Because the main object of this study was to measure contact angles and not surface tension values, a review will be given only for techniques which can be used to measure contact angles.

A review of the 3 following methods will be given:

Sessile drop or adhering gas bubble

Wilhelmy-Gravitational method

Capillary rise at a vertical plate.

2.1 Sessile Drop and Adhering Bubble

The method of the sessile drop, alternatively, of the adhering gas bubble is at the present the most widely used technique for measurements of contact angles (see Figure 2.1).

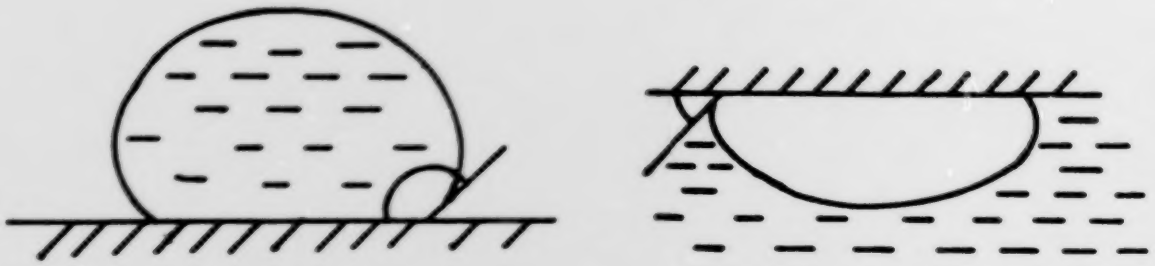

Sessile drop Adhering bubble

Figure 2.1. Illustration of a sessile drop and an adhering bubble.

The general procedure for the sessile drop method is to form a drop of liquid resting on a horizontal plane surface. From photographs of the drop profile, both the surface tension of the liquid and the contact angle can be measured. It is, in general, the most convenient method if high accuracy is not required, and it has the two major advantages of requiring only very small quantities of liquid and that samples as small as a few cube millimeters can be used.

Another advantage of the sessile drop is that it is easy to study the effects which a change in the gas phase will have on the surface tension and the contact angle. The sessile drop method is also ideal

for studying aging effects or other time-dependent effects since the arrangement can be left completely undisturbed and static for any time interval while photographs are taken periodically.

The adhering gas bubble has the advantage that the gas in the adhering bubble can be saturated with the vapour of the liquid much easier than the gas phase around the sessile drop. If the sessile drop consists of a mixture of liquids with very different vapour pressures, the composition of the sessile drop may change with time. It is therefore preferable to use an enclosed chamber when one of the components is highly volatile. A very practical reason for using an enclosure is that evaporation may cause the liquid to retract, so that a retreating or an intermediate contact angle is observed unintentionally (see chapter about contact angle hysteresis).

It is commonly claimed that the accuracy of the sessile drop method is ±2%. It would be better to call this a matter of precision; agreements between independent laboratories using this method have in the past been as poor as 5% (53).

When visual observation of the sessile drop is possible, the contact angle can be measured either by using a telescope equipped with a goniometer eyepiece (53), or by taking a photograph from which the angle can be measured at leisure (53,54). The greater precision with photographic measurements is balanced by a decrease in convenience when dynamic effects are taken into account. The reproducibility of individual drops is commonly poor, such that for any high accuracy, a large number of photographs would be required.

Difficulties arise when the ambient liquid is not transparent in which case the drop shape cannot be seen directly. The same problem also arises when high temperature systems like molten salts, slags or metals are studied. These high temperatures limit the choice of construction materials. Non-transparent materials such as graphite and aluminium oxide are often used for making crucibles in which the system of interest is placed.

Another possibility is then to form the image of the liquid drop on a photographic film by using a horizontal beam of X-rays (43,45,55). With the use of X-rays, it is possible to also measure the contact angle formed by an adhering gas bubble (see Figure 2.1). It is a practical method to study the wetting of electrodes during gas formation at either the anode or the cathode in electrolytes where a visual inspection is impossible. One example is to study the wettability of the anode during the electrolysis of aluminium. It is also possible to measure the interfacial energy between two liquids by replacing the gas above the sessile drop by a second liquid with a density lower than that of the sessile drop.

The use of a horizontal X-ray beam in combination with a vertical reaction tube makes it easy to examine the symmetry of the drop simply by rotating the drop and by taking photographs from different angles.

The most serious disadvantage of the X-ray technique is that the drop outline tends to become diffused rather than sharply defined (45,55). This is due to the fact that more X-ray photons are absorbed when the beam passes through the center of the drop than when the beam passes

through the drop close to the edge (see Appendix ONE) (56). Despite this difficulty, good agreement with other methods has been obtained as shown by Eremenko (57) and others (43,58).

2.1.1 Theoretical considerations of the sessile drop

When the radii of curvature are sufficiently large, compared to the thickness of a non-homogeneous film separating two bulk phases, the pressure difference across the curved interface is described by the Laplace equation (59,60):

$$\gamma_{LV}\left(\frac{1}{R_1} + \frac{1}{R_2}\right) = \Delta p \qquad (2.1)$$

where R_1 and R_2 are the principal radii of curvature of the surface at the point considered and γ_{LV} is the interfacial tension.

The pressure difference is a linear function of elevation when gravity is the only external force.

$$\Delta p = \Delta p_0 + (\Delta\rho)gz \qquad (2.2)$$

Δp_0 is the pressure difference at a selected datum plane, $\Delta\rho$ is the density difference between the two phases, g is the gravitational acceleration and z is the vertical height measured from the datum plane.

The following equation can be found by combining the two equations above:

$$\gamma_{LV}\left(\frac{1}{R_1} + \frac{\sin\phi}{x}\right) = \frac{2}{R_0} + (\Delta\rho)gz \qquad (2.3)$$

At the origin, the two radii of curvatures are identical and are designated by the symbol R_0. R_1 turns in the plane of the paper and $R_2 = x/\sin\phi$ rotates perpendicular to the plane of the paper. ϕ is the turning angle measured between the tangent to the interface at the point (x,z) and the datum plane (Figure 2.2).

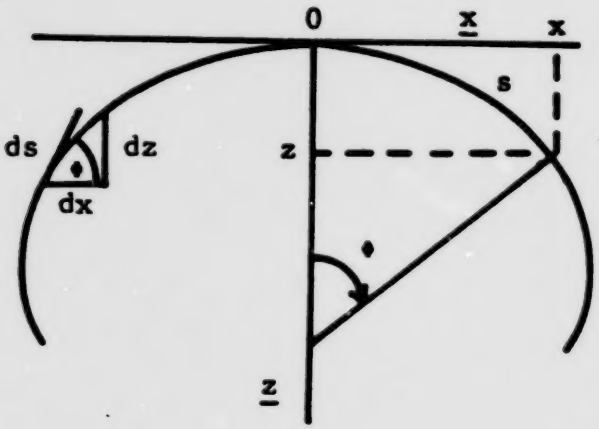

Figure 2.2. Definition of coordinate system for a sessile drop.

A geometrical consideration given by Rotenberg et al. (61) yields the following set of first order differential equations:

$$\frac{dx}{ds} = \cos\phi \qquad (2.4)$$

$$\frac{dz}{ds} = \sin\phi \tag{2.5}$$

$$\frac{d\phi}{ds} = \frac{2}{R_0} + \frac{(\Delta\rho)gz}{\gamma_{LV}} - \frac{\sin\phi}{x} \tag{2.6}$$

s is the arc-length parameter.

Boundary conditions for these equations are:

$$x(0) = z(0) = \phi(0) = 0 \tag{2.7}$$

The complete shape of the curve may be obtained by integrating simultaneously these three differential equations.

Until recently, the sessile drop method required measurements of a few preselected critical points (51,62,63) which are compatible with the use of tables by Bashfort and Adams (64). These preselected points are critical since they correspond to special features such as maximum diameter and height of the drop, and must be determined with high precision.

Another method that appears attractive is based on the fact that for sufficiently large enough drops, the height is independent of the drop size. Then

$$\cos\theta = 1 - \frac{\Delta\rho g h^2}{2\gamma_{LV}} \quad \text{and} \quad \gamma_{LV} = \frac{\Delta\rho g h'^2}{2} \tag{2.8}$$

where h, h' and θ are defined in Figure 2.3. The pitfall of this method is the requirement that the drop be large (65,66).

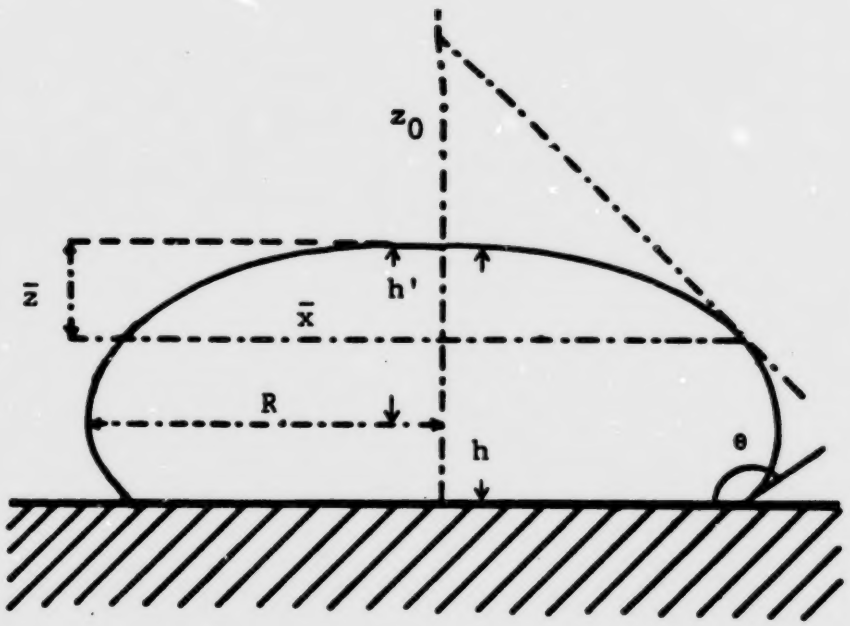

Figure 2.3. Profile of a sessile drop showing the measurements necessary to calculate the surface tension by the following method(63).

$$\gamma_{LV} = \rho \cdot g \cdot R^2 (0.052/f - 0.1227 + 0.0481 \cdot f)$$

where

$f = {}^{z_0}/_{R} - 0.4142$, $Z_0 = \bar{x} - \bar{z}$, g = acceleration due to gravity

ρ = density difference between the liquid and the gas ,

γ_{LV} = surface tension of the liquid.

Maze and Burnet (67,68) developed a numerical algorithm in which a calculated sessile drop shape is made to fit an experimentally measured shape, by varying two parameters until a best fit is obtained. But there are different deficiencies in their algorithm and a new computational procedure has been developed by Rotenberg et al. (61). As input for this algorithm only density, the local gravity and several coordinate points in a coordinate system where the origin is placed at will, are required. This algorithm works both for pendant as well as sessile drops, and also when the contact angle is less than 90°. For determination of contact angles, the vertical coordinate of the three phase lines need to be specified.

With this algorithm, it is assumed that the drop is totally symmetrical and only one unique value of the contact angle will be calculated. To calculate this contact angle and also the surface tension, only coordinate points on the top half of the drop outline are necessary. Any distortion in this region of the drop will therefore be serious and the calculated contact angle value will not correspond to the measured value found from a photograph. In such cases, the measured value from a photograph must be used because a distortion of the upper surface will not perturb the liquid in the region on the contact line with the solid (69). The shape of the drop in the vicinity of the solid surface is completely controlled by energetics of the three interfaces (solid-vapour, solid-liquid and liquid-vapour) and the topography of the solid (53).

2.1.2 Measurements of contact angle from photographs

When the contact angle is measured from a photograph, the observer must imagine the curve that would be present if the drop edge continued past the solid surface. This cannot be done with great accuracy, or even with great consistency, between one observer and another. So it is better, with a photograph, to locate the center of the circular arc that is tangent to the drop profile, draw a radial line, and obtain θ as the angle between the line and the normal to the surface (see Figure 2.4).

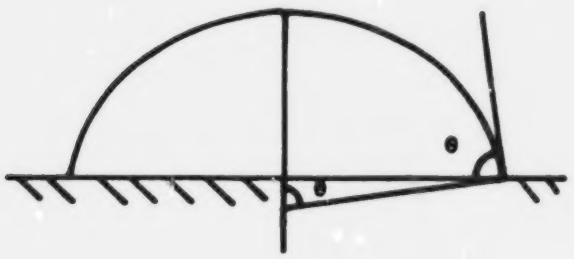

Figure 2.4. Determination of contact angle from a photograph. Locate the center of the circular arc that is tangent to the drop profile, draw a radial line, and obtain θ as the angle between the line and the normal to the surface.

An elementary trigonometric construction shows that if C is the cord of a segment of a circle (i.e., the base of the silhouette of a spherical cap) and h is the height, then (70)

$$\frac{2h}{C} = \tan \frac{\theta}{2} \qquad (2.9)$$

If a drop of liquid is used, it must be very small, so that the gravitational distortion is negligible. This requirement can be satisfied if the surface tension of the liquid is relatively large compared to the weight of the drop, such as for a small drop of liquid metal with high surface tension. This technique is however, not recommended because of the drop-size effect mentioned later in this chapter.

2.1.3 Errors due to asymmetry in the drop profile

The main source of geometric errors in the sessile drop technique is due to asymmetries in the drop profile. They usually develop upon melting or temperature changes, because the motion of the liquid drop on the substrate may not be uniform in all directions when contact angle hysteresis is present. Another reason for asymmetry is contamination of the drop or the substrate.

Large contact angles are desirable for measuring surface tension, and for most previous methods of calculating the surface tension a contact angle larger than 90° was necessary. Experiments were therefore preferably carried out on non-polished fine-grained substrates (43) to obtain large advancing contact angle values. This would automatically lead to large contact angle hysteresis which would increase the possibility of an asymmetrical profile. Contact angle measurements were therefore usually carried out starting at the lower temperatures and continued only during the initial heating cycle to avoid the hysteresis which is observed to occur on cooling (71).

2.1.4 Drop size

The effect of size of the sessile drop on contact angle was studied by Good and Koo (72) and by Boruvka and Neumann (73). They found that the variation in contact angle with drop size seemed to be related to the existence of contact angle hysteresis. When hysteresis is appreciable, the contact angle was found to decrease with decreasing drop size, below a critical size. Figures 2.5 and 2.6 show the effect of inhomogeneity in the substrate on the solid/liquid/gas three phase line and its effect on the contact angle.

This phenomena may also explain why the contour of the sessile drop near the solid support is usually more diffuse than other parts of the drop, and it makes accurate contact angle measurements difficult to obtain.

2.2 Wilhelmy-Gravitational Method

If a smooth, vertical plate is brought into contact with a liquid, as indicated in Figure 2.7, the liquid will exert a downward force on the plate (74), which is given by

$$F = P\gamma_{LV} \cos\theta \qquad (2.10)$$

where P is the perimeter of the plate.

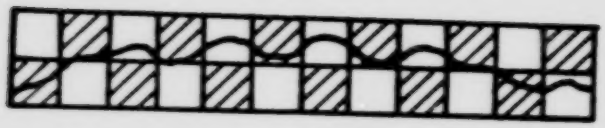

Figure 2.5. Schematic drawing of tortuosity of a three-phase line for a drop on a solid surface consiting of regular patches of surface having different surface energies. Intrinsic contact angle on the crosshatched area is higher than that on nonshaded area.

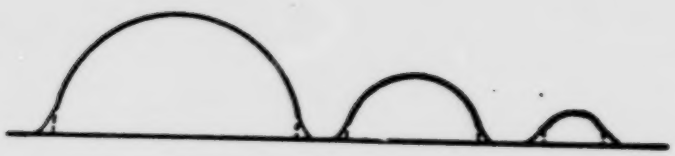

Figure 2.6. Schematic drawing of profiles of drops on a heterogeneous solid surface. The dashed line is the hidden profile for regions of liquid-vapour surface where the surface is coming down to low-energy areas on the solid.

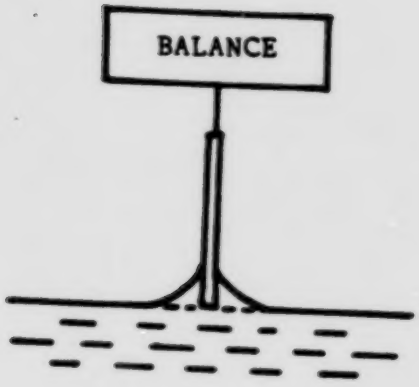

Figure 2.7. Vertical plate method.

Plate extends perpendicular to plane of paper; zero net depth of immersion.

If the depth of immersion is not zero, so that a volume V of liquid is displaced,

$$F = P\gamma_{LV} \cos\theta - V\Delta\rho g \qquad (2.11)$$

where $\Delta\rho$ is the difference in density between the two fluids (75). To evaluate the contact angle, the surface tension γ_{LV} must be known. If the plate is not effectively smooth, it will not be suitable for determination of the contact angle of the liquid on the solid. A basic experimental set up (53) is shown schematically in Figure 2.8.

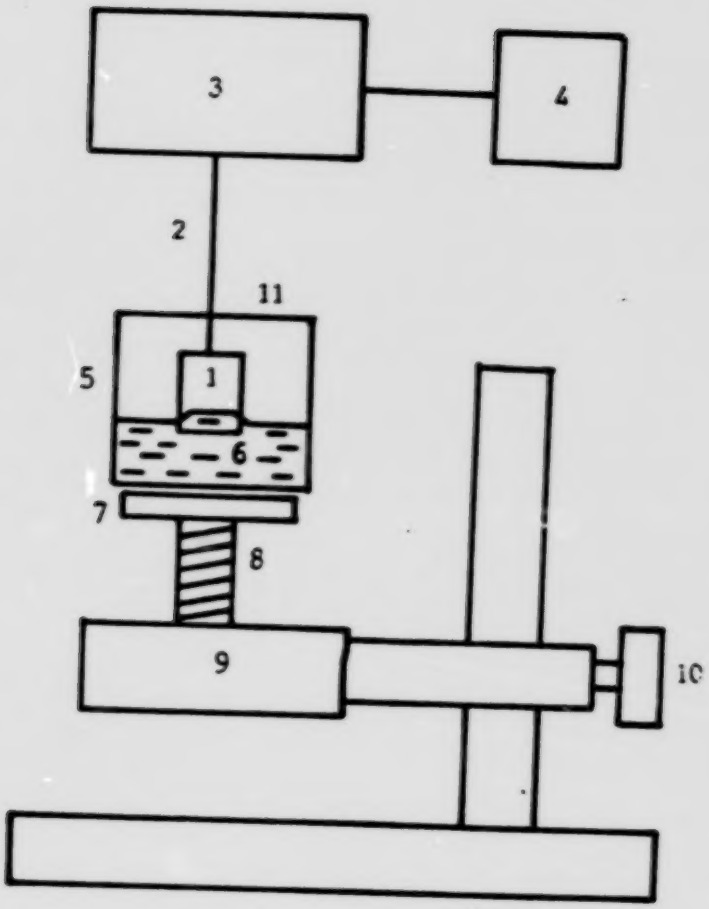

Figure 2.8. Apparatus for Wilhelmy technique.

1) measuring plate, 2) rod, 3) electrobalance, 4) recorder, 5) measuring cell, 6) liquid, 7) movable platform, 8) screw or gear mechanism, 9) motor, 10) clamp and support, 11) lid.

Advancing and receding conditions are established as follows (53): After suspending the plate from the electrobalance, the table is raised from an initially low position to such a height that the surface of the liquid is approximately 1 mm below the lower edge of the plate. Then the table is raised slowly by means of the screw. After contact is established between the plate and the liquid, the motor is stopped immediately. The resulting configuration is one of advancing contact angle. The depth of immersion is zero, so that equation (2.10) may be used.

Receding conditions may be established by immersing the plate to some depth and subsequently withdrawing the plate through exactly the same distance. This may be done by timing the immersion and the withdrawal or by measuring the depth of immersion and withdrawal by means of a cathetometer.

2.2.1 Advantages and disadvantages of the Wilhelmy technique

The advantage of this method is that the measurement of an angle is reduced to the measurement of a weight, which can be performed with much higher accuracy than the reading of an angle from a photograph. The method has the further advantage that it can be completely automated.

While the Wilhelmy method at first sight seems to be an ideal method for obtaining high-precision contact angles, it has several drawbacks that restrict the usefulness of the method. One disadvantage is that large amounts of liquid have to be used. The crucible containing the liquid must be sufficiently large that the liquid surface

has a horizontal region in the center of the crucible which is wider than the plate. To satisfy this requirement, a crucible diameter larger than 5 cm may be necessary and a furnace with a large region of uniform temperature must be used.

One other disadvantage is that the high sensitivity of an electrobalance employed in this method can be exploited only if the perimeter of the plate is constant. Furthermore, the plate must have the same composition and morphology at all surfaces-front, back, and both edges. Also, absorption of the vapour of the liquid at various parts of the gravimetric system other than the plate may change the recorder readings. With the relative high vapour pressure of $PbCl_2$ it was expected that this could be a problem if this technique had been used in the present study.

2.3 Capillary Rise at a Vertical Plate

In this technique, the solid surface is aligned vertically and brought into contact with the liquid as in the Wilhelmy technique. But instead of the capillary pull, the capillary rise h at the vertical surface is measured (see Figure 2.9).

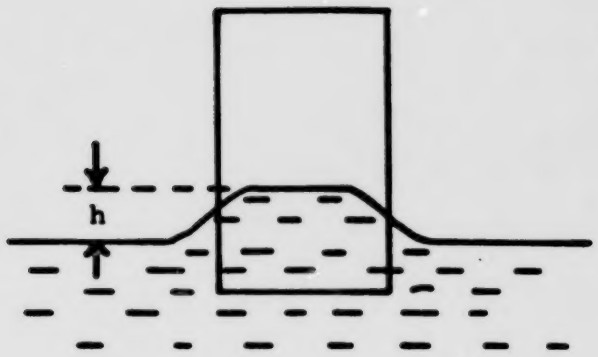

Figure 2.9. Capillary rise at a vertical plate.

This method has been found to be particularly effective for measuring contact angles as a function of the rate of advance and retreat and for determining the temperature coefficient of the contact angle.

For an infinitely wide plate, an integration of the Laplace equation (2.1) yields

$$\sin\theta = 1 - \frac{\Delta\rho g h^2}{2\gamma_{LV}} \tag{2.12}$$

For practical purposes, plates that are about 2 cm wide (53) satisfy the theoretical requirement of "infinite width".

This method also requires large amounts of liquid and a large region of uniform temperature. To measure the capillary rise h, a horizontal reference area of the liquid is necessary. Another problem is the optical measurements necessary to measure the capillary rise. For high-temperature studies this leads to difficult design and construction problems. With an apparatus design for use in the temperature interval from -80 to +80°C, Neumann and co-workers have obtained very accurate and reproducible values of contact angles (76,77).

One main disadvantage with indirect methods such as the capillary rise or the Wilhelmy method is that the surface tension of the liquid must be known. While this restriction does not usually present severe problems with most liquids, there may be a serious uncertainty for solutions of different liquids and especially for solutions of surface active substances.

The joint use of the capillary rise method and the Wilhelmy method makes it possible to determine contact angle and liquid surface tension at the same time (53). Eliminating γ_{LV} from equations (2.10) and (2.12), leads to

$$\cos\theta = \frac{4Fg\Delta\rho h^2 P}{4F^2+P^2(\Delta\rho)^2 h^4 g^2} \qquad (2.13)$$

Measuring F and h as described above and knowing the density of the liquid and the perimeter P of the plate, the contact angle can be calculated from equation (2.13). Alternatively, θ may be eliminated from equations (2.10) and (2.12) to obtain the liquid surface tension

$$\gamma_{LV} = \left(\frac{F}{Ph}\right)^2 \frac{1}{\Delta\rho g} + \frac{\Delta\rho g h^2}{4} \qquad (2.14)$$

2.4 Choice of Experimental Technique

The sessile drop method was adopted as the experimental technique in view of its experimental simplicity, its application to high temperature measurements and because a suitable X-ray source to record the image of the drop profile, was available. Other important advantages of the sessile drop method compared to the Wilhelmy method and the capillary rise method, are that the knowledge of the surface tension of the liquid is not necessary, that only small amounts of liquid are required and that a relatively small region of uniform temperature around the drop is sufficient.

Usually (44,78) an image of the drop profile is obtained by using a collimated light source. However, in this study a X-ray radiography technique (43,45) was choosen. The main reasons for this decision were:

1) a suitable X-ray source was available,
2) liquids containing lead give high contrast X-rays images,
3) the symmetry of the drop could be examined by rotating the vertical reaction tube,
4) it is suited to study liquid/liquid interfacial tensions and to study the wetting of electrodes during electrolysis.

2.5 Fundamentals of Radiographic Imaging

The principle of imaging with X-rays is to pass a beam of X-rays through the system of interest producing absorption of some parts of the beam while allowing the remainder to pass through. The transmitted

beam so obtained is allowed to fall on an image receptor, such as a film or an image intensifying unit (79,80,81).

When X-ray photons pass through matter, they may either be transmitted, absorbed or scattered. Which of these occurs depend both on the nature of the material and the energy of the photon. Photons of sufficient energy which pass through the system without any interaction are called primary X-ray photons, and they are essential in the imaging process.

If the voltage used to generate the X-ray beam is too low, that is, if the photon energy is too low, the attenuation may be total and no image is formed. On the other hand, if the voltage is too high there may be little difference in the attenuation of the beam by the different parts of the system with very little difference in the transmitted radiation intensities. This lack of contrast will render the image useless, as the information it contains cannot be visually retrieved. It is thus necessary to select the correct beam energy and intensity for the particular application.

CHAPTER 3

THEORY

3.1 Contact Angle and Surface Tension

Surfaces play an important role in chemical reactions. For example, catalytic reactions take place on surfaces, the magnitude of the surface tension is important in the flotation of minerals, surface tension is an important factor when spray or mist is formed, wetting is important in electrolytic reactions and formation of good seals, absorption of gases and liquids on solids is technologically important (30,31,82,83).

One of the exciting aspects of surface thermodynamics is that it is possible to correlate macroscopic surface properties with a physical model of the surface. Although such models cannot be proved or disproved by thermodynamics, it nevertheless offers a reasonable interpretation of the results and possibilities to predict what is going to happen for unknown systems.

In the absence of gravity or other forces, liquid surfaces will take a spherical shape due to the action of forces which to a certain extent can be compared to the forces that act when a balloon is blown up. The important difference is that the force is constant irrespective of the extent of surface expansion. The surface tension is given as force per length or energy per area.

3.2 Young Equation and Laplace Equation

Even though surface tension of solids versus gases and liquids are generally poorly known, they are used in the famous wetting equation of Young. Provided that $\gamma_{SV} \leq \gamma_{SL} + \gamma_{LV}$ and $\gamma_{SV} \leq \gamma_{LV} + \gamma_{SV}$, a liquid drop will form a definite angle with a solid:

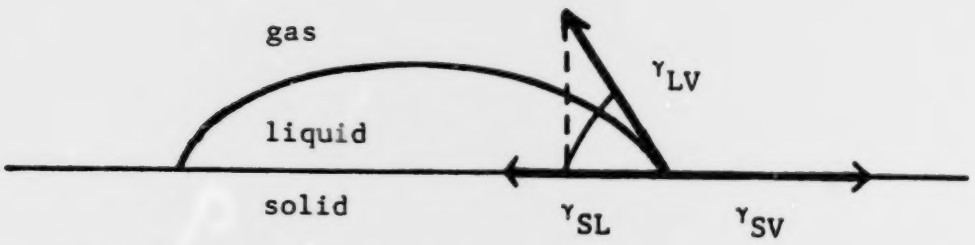

Figure 3.1. Illustration of Young's equation.
Where: γ_{LV} is the liquid-vapour surface tension, γ_{SV} is the solid-vapour surface tension, γ_{SL} is the solid-liquid interfacial tension and θ is the contact angle.

Young's equation is obtained by equating the horizontal components:

$$\gamma_{LV} \cos\theta = \gamma_{SV} - \gamma_{SL} \qquad (3.1)$$

Of these quantities γ_{LV} and θ are readily measurable. The surface tension of the liquid can be measured by a number of techniques. For example, by freeing a rod of known diameter from the surface or by measuring the maximum bubble pressure while forcing a gas bubble through a tube into a liquid. θ can be measured by taking a photo-

graph of the drop. The difference $\gamma_{SV}-\gamma_{SL}$ is then obtained from Young equation, but usually the quantities γ_{SV} and γ_{SL} can not be determined separately.

The relations which can occur as a result of the forces represented in Young's equation (3.1) are shown graphically in Figure 3.2, in which the interfacial tension γ_{SL} is plotted against cosθ for difference values of γ_{LV}. For this case a solid of surface tension 1000 mJ/m^2 is considered. Several important points emerge.

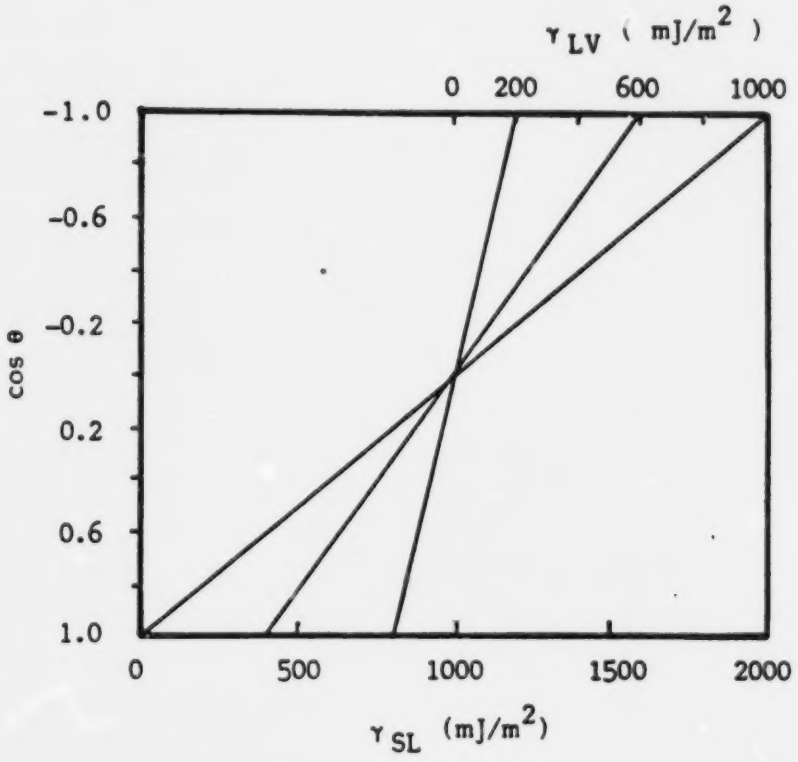

Figure 3.2. Relations between γ_{SL} , γ_{LV} and cosθ for a solid with γ_{SV} assumed to be 1000 mJ/m^2.

(1) When $\theta=90°$, $\gamma_{SV}=\gamma_{SL}$ whatever the value of γ_{LV}.

(2) If $\theta<90°$ ($\cos\theta>0$) a decrease in γ_{LV} causes a decrease in θ at a constant value of γ_{SL}. If $\theta>90°$ ($\cos\theta<0$) then a decrease in γ_{LV} produces an increase in θ for a constant γ_{LV}. This second point is not always realized, it being generally assumed that lower γ_{LV} promotes wetting when $\theta>90°$. In practice, this is generally the case, since it is due to the change in γ_{SL} which more than offsets the decrease in γ_{LV}.

(3) θ can never be zero if $\gamma_{LV}>1000$ mJ/m^2 for this particular solid.

(4) For low energy surfaces, θ can only be zero with liquids of low surface tension provided $\gamma_{SL}<\gamma_{SV}$.

(5) If γ_{LV} is low then γ_{SL} can have quite high values approaching that of γ_{SV}, even when θ is zero.

(6) The lower the value of γ_{LV}, the greater the change in θ for a given change in γ_{SL}.

Young's equation is deceptively simple and the equation has been a source of many arguments (84,85). Its extensive use reflects, however, its general acceptance in spite of the fact that it has never been verified experimentally due to the difficulties in determining the surface tension of solids. Further, the fact that the vertical components of the forces are not equated has been used as an argument against the equation.

Minimizing the overall free energy as carried out by Gibbs (59), of a system consisting of a liquid in contact with a solid, yields the Laplace equation of capillarity

$$\gamma_{LV}\left(\frac{1}{R_1} + \frac{1}{R_2}\right) = \Delta p \qquad (2.1)$$

R_1, R_2: Radius of curvature

Δp : Pressure difference across the interface

γ_{LV} : Liquid-vapour surface tension

The Laplace equation describes the shape of the liquid/vapour and liquid/liquid interface away from the solid/liquid interface. Young's equation, on the other hand, is an equilibrium condition which involves properties which are a function of the solid.

3.3 Limitations of the Classical Theory of Capillarity

With his thermodynamic theory of capillarity, Gibbs (59) developed as the main equilibrium condition the Laplace equation. Together with the Young's equation and the Neumann triangle relation, these equations are considered as the basic equations of surface thermodynamic.

Because of the very small thickness of interfaces, Gibbs represented an interface by a single (mathematical) surface - the Gibbs dividing surface (see Figure 3.3). The first step is to extrapolate the bulk properties from the interior of each bulk phase up to the dividing surface. In the next step the actual quantities of internal energy, entropy and masses inside an interface is considered. The excess of these quantities over the extrapolated bulk quantities is attributed to the dividing surface in the form of surface densities, which is distinguished from the bulk densities by the subscript (A).

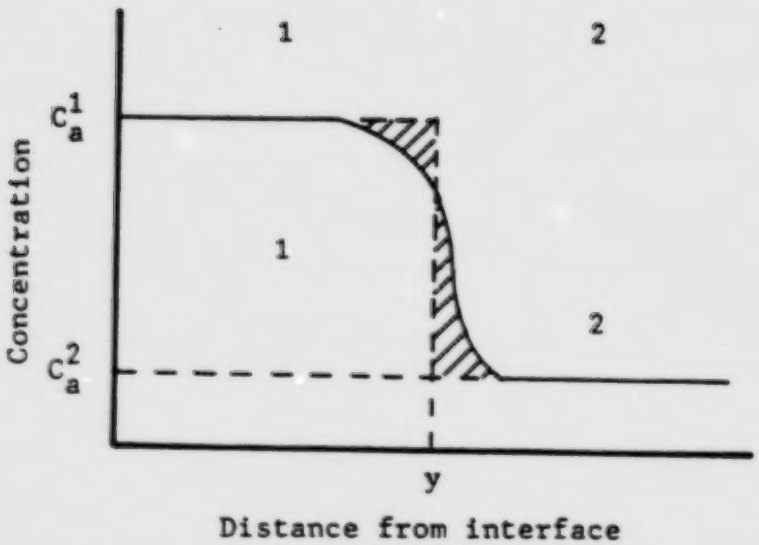

Figure 3.3. Illustration of concentration change through an interface.

The fundamental equation used by Gibbs to describe curves interfaces is given by

$$dE^A = TdS^A + \gamma dA^A + \Sigma\mu_i^A \cdot dN_i^A + \frac{1}{2}(C_1+C_2)d(c_1+c_2) + \frac{1}{2}(C_1-C_2)d(c_1-c_2) \qquad (3.2)$$

where: $c_1 = \frac{1}{R_1}$ and $c_2 = \frac{1}{R_2}$,

$C_1 = \left(\frac{\partial E^A}{\partial c_1}\right)$ and $C_2 = \left(\frac{\partial E^A}{\partial c_2}\right)$

N_i^A: excess surface consentration

μ_i^A: chemical potential of i in the interfaces

For moderate curvature Gibbs assumed that $c_1 \simeq c_2$ and that $d(c_1-c_2) \simeq 0$. C_1 and C_2 will depend on the choice of the dividing surface, and it was chosen by Gibbs such that $C_1+C_2=0$. The main limitation centers therefore around the curvature terms, and his treatment is not adequate for regions of high curvatures of the liquid/vapour interface. One example of such a situation is capillary condensation.

Gibbs remarked that a closer approximation in the theory might be attained by taking special account of the lines in which surfaces of discontinuity meet and that such a treatment might be entirely analogous to the treatment of interfaces. This was later done by Boruvka and Neumann (84) and they introduced the line tension σ to take into account these effects.

$$\sigma = \left(\frac{\partial E^L}{\partial L}\right) \tag{3.3}$$

The main results of their treatment are a generalized Laplace equation and a generalized Young equation. The generalized Laplace equation is given by

$$J_{LV}\gamma_{LV} + 2K_{LV}C_{1LV} = \Delta P \tag{3.4}$$

where

$K_{LV} = c_1 \cdot c_2 \quad (c_1=1/R_1 \text{ and } c_2=1/R_2)$

$J_{LV} = c_1+c_2$

$C_{1LV} = \left(\frac{\partial E^A}{\partial J_{LV}}\right)$

ΔP = pressure difference across the interface

After neglecting all remaining curvature and contact angle potentials, this equation reduces to the classical Laplace equation. The reduced form of the generalized Young equation is given by

[illegible]

where

σ : line tension

K_{gs}: geodesic curvature (84)

γ_{SV}: solid-vapour surface tension

γ_{SL}: solid-liquid interfacial tension.

These generalized equations have so far been of no practical use because of the difficulties in evaluating any value to the line tension (84) and the curvature potential (84,86,88). The most important aspect of this analysis is that it shows that Gibbs treatment is not strictly mathematically and thermodynamically correct and that the Laplace and Young equations might not be adequate for all capillary systems.

3.4 Rough and Heterogeneous Surfaces

In the treatment by both Gibbs (59) and Boruvka and Neumann (44) it was assumed that the solid was smooth, homogeneous, isotropic and nondeformable. Most real solids do not meet these restrictions and the controversy over the validity of Young's equation and thus the thermodynamic status of contact angles is understandable.

The equilibrium contact angle θ is an unique function of the interfacial tensions γ_{LV}, γ_{SV} and γ_{SL}. But in the vast majority of cases, experimentally observed contact angles are not unique and there normally exists a range of contact angles, quite often as large as 50° to 90°, over which any one contact angle gives rise to a mechanically stable liquid meniscus. Normally, the largest and smallest of these angles are recorded and termed the advancing contact angle θ_a and receding contact angle θ_r, respectively. The difference between the advancing and receding contact angle is called the contact angle hysteresis.

Wenzel (89) recognized that Young's equation may not be an equilibrium condition for the physical interaction between a solid and a liquid. He argued that if a solid surface is rough, the interfacial free energy γ_{SL} and γ_{SV} should not be referred to as the geometrical area, but to the actual area. This leads to the so-called Wenzel equation

$$r \cos\theta_y = \cos\theta_w \tag{3.6}$$

$$r = \frac{\text{actual area}}{\text{geometrical area}}$$

The same type of reasoning was applied to heterogeneous and porous surfaces by Cassie and Baxter (90). A heterogeneous solid surface is one which contains domains of different surface free energies. For a solid surface consisting of two types of domains, the intrinsic contact angles being θ_{e1} and θ_{e2} with respect to a given liquid, Cassie (91) obtained

$$\cos\theta_c = \sigma_1 \cdot \cos\theta_{e1} + \sigma_2 \cdot \cos\theta_{e2} \qquad (3.7)$$

where σ_1 and σ_2 are the fractional surface areas of the two types of surfaces and θ_c the Cassie contact angle.

One of the main difficulties with relations like the Cassie equation and the Wenzel equation is that they appear to conflict with experimental observations. Wenzel's equation predicts that the contact angle on a rough surface should be smaller than the contact angle on a smooth surface if the contact angle on the smooth surface is smaller than 90°, while if the contact angle on the smooth surface is larger than 90°, the contact angle on the rough surface should be larger.

The concept of metastable states was first introduced by Good (92) and later by Neumann and Good (93). Neumann and Good considered a vertical plate of infinite width dipping into a liquid. Surfaces that were smooth, but energetically heterogeneous, were given a thermodynamic treatment. It was shown that the free energy curve has a sawtooth structure corresponding to a number of metastable equilibrium states between θ_{e1} and θ_{e2} (θ_{e1} and θ_{e2} are the contact angles on the two domains). It was also shown that the absolute minimum in the free energy is found to be given by the Cassie equation, but due to the large number of metastable states on both sides of θ_{e1} it is rather difficult to determine it experimentally. The experimental advancing contact angle θ_a is equal to the contact angle of the low energy component θ_{e1}. θ_a is equal to θ_{e1} because the first metastable state occurs at $\theta=\theta_{e1}$. A similar argument for the receding contact angle θ_r leads to θ_r being equal to θ_{e2}.

Eick et al. (94) carried out a similar free energy analysis on a rough solid surface. A free energy curve with several metastable states was found. When an absolute minimum in the free energy is present, the corresponding contact angle is equal to the contact angle predicted by the Wenzel equation. Due to the large number of metastable states, it is impossible to know when the contact angle is equal to the Wenzel contact angle. The advancing contact angle will normally be the first metastable contact angle and have the largest possible value. The receding contact angle is normally the last metastable equilibrium if such a metastable state exists, otherwise the receding contact angle is equal to zero. It must be noted that the above mentioned contact angles are macroscopic experimentally determined contact angles, and not microscopic, local equilibrium contact angles.

This free energy analysis showed that for several stated conditions the receding contact angle was zero. This fact is used in several methods to calculate the surface tension by assuming zero contact angle. Capillary rise in a tube, Du Nuoy ring method and the pin method are all methods where the contact angle is assumed to be zero.

3.5 Methods of Estimating Surface Tension of Solids

Most of the existing methods for estimating surface tension of solids depend on very specific properties, e.g. cleavability (95) or negative strain rates of metals at temperatures close to the melting point (96). The more recent developments in the methods of determining surface tension of solids based on contact angle measurements will be discussed first.

Ward and Neumann (97) showed, using strictly thermodynamic arguments, that an equation of state exists between γ_{SV}, γ_{SL} and γ_{LV} for a two-component three-phase system when the surface of the solid is assumed to be rigid, smooth and homogeneous, and when there is no dissolution of solid nor absorption of liquids or gases by the solid. Their argument is only valid as long as γ_{LV} is larger than γ_{SV} because they assumed no absorption of gases on the solid surface.

It was shown (98) for specific solids, that a plot of $\gamma_{LV}\cos\theta$ versus γ_{LV} resulted in a smooth curve for each particular solid, which could be represented by a second-order polynomial

$$\gamma_{LV}\cos\theta = a(\gamma_{LV})^2 + b\gamma_{LV} + c \tag{3.8}$$

These equations were found based on low temperature experiments with organic solids such as hexatriacontane and cholesteryl acetate (97), and no claim was made by the authors that these equations should apply to systems like mercury/polymers and glass melts/metals.

The following empirical formulation of the equation of state was given by Neumann et al. (98).

$$\gamma_{SL} = \frac{\gamma_{SV}+\gamma_{LV}-2\beta(\gamma_{SV}\cdot\gamma_{LV})^{1/2}}{1-2\alpha(\gamma_{SV}\cdot\gamma_{LV})^{1/2}} \tag{3.9}$$

$$\cos\theta = \frac{2(\alpha\gamma_{SV}-\beta)(\gamma_{SV}\cdot\gamma_{LV})^{1/2}+\gamma_{LV}}{\gamma_{LV}(2\alpha(\gamma_{SV}\cdot\gamma_{LV})^{1/2}-1)} \tag{3.10}$$

$\alpha = 0.0075$

$\beta = 1.000$

Several investigators have found linear relationships between $\cos\theta$ and γ_{LV} for different specific solids such as Al_2O_3 (99,100), $UO_{2.0}$ (30) and graphite (99). Due to the scatter in the data and the usually small range of surface tension values used by each investigator, no specific relation has so far been found. Two examples of such plots (100,101) are shown in Figure 3.4 and in Figure 3.5.

A rearrangement of the second-order polynomial by Neumann et al. (98) gives the following equation

$$\cos\theta = a \cdot \gamma_{LV} + b + \frac{c}{\gamma_{LV}} \quad . \tag{3.11}$$

For small values of c and large values of γ_{LV}, this equation approaches a linear equation. Livey and Murray (30) have carried out an extensive study of the wetting properties of solid oxides and carbides by liquid metals. Data from this study has been used to calculate $\gamma_{LV}\cos\theta$ for different liquids at different temperatures on $UO_{2.0}$. A plot of $\gamma_{LV}\cos\theta$ versus γ_{LV} is shown in Figure 3.6. The data can be approximated by a straight line. However, it must be mentioned that some of the data in this report did not fit this plot and are not shown in Figure 3.6. The reason for this might be that different gas atmospheres were used (argon or vacuum) or that the temperature range (from 200°C to 1500°C) was too large.

To collect sufficient data to test such a relation, data from different investigators are necessary which again involves several problems. The specific solid used by one investigator is not necessarily

Figure 3.4. Cosine of contact angle versus surface tension of (A) liquid Ag for systems Ag/AlN and Ag/TiC and (B) liquid Cu for systems Cu/AlN and Cu/TiC(after S.K. Rhee (100)).

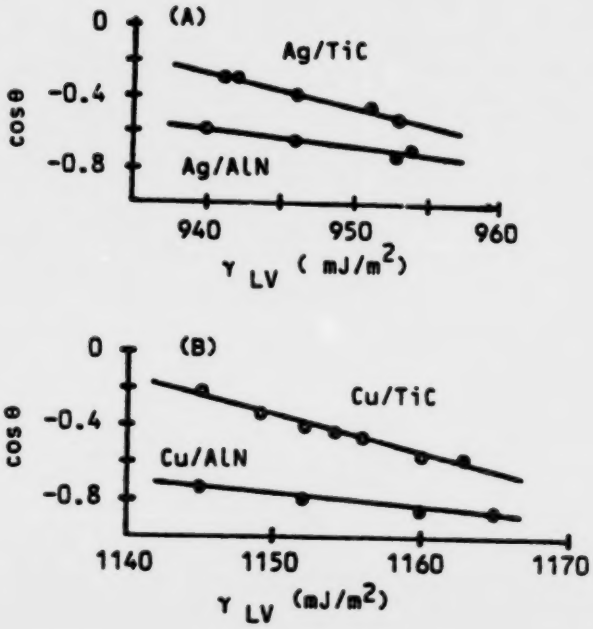

Figure 3.5. Cosine of of the contact angle versus surface tension for liquid transition metal sessile drops on solid sapphire at 1500 °C under vacuum (after Eberhart(101)).

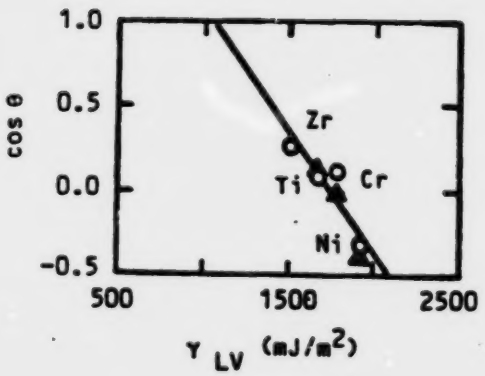

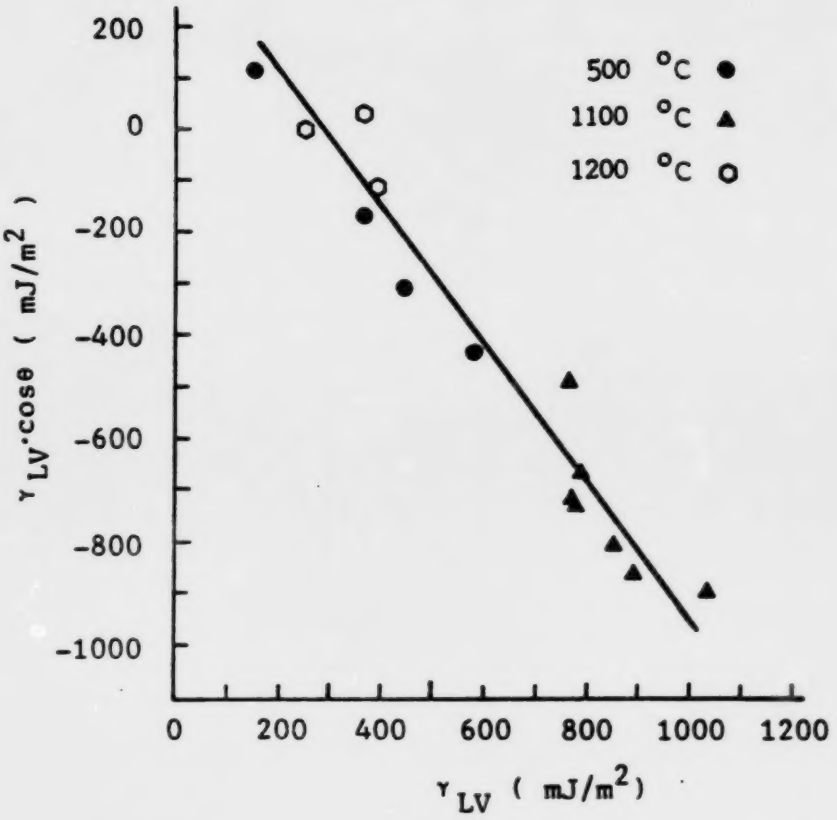

Figure 3.6. $\gamma_{LV}\cos\theta$ as a function of the surface tension γ_{LV} of various liquids on UO_2(Data are taken from Table 3 and 4 in publication by D.T. livey and P. Murray(30)). The different liquid metals were Sn, Al, Pb, Bi and Cu and the experiments were carried out under vacuum or under an argon atmosphere.

the same as the solid used by another with regards to roughness, homogeniety and composition. Different authors may also have different ideas concerning the equilibrium contact angle, the advancing contact angle and so forth. An illustration of these problem is shown in Figure 3.7, where the contact angle is plotted as a function of both the temperature and the roughness of the substrate (102).

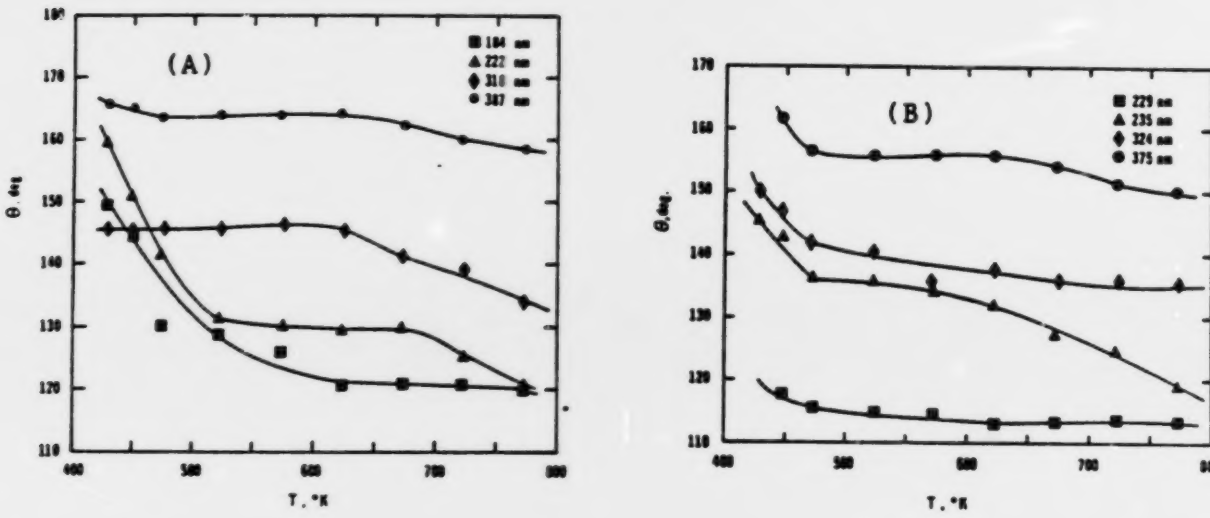

Figure 3.7. The variation of contact angle with temperature for the In-Nb system(A) and for the In-Zr system(B)(102).

The importance of roughness on the value of the contact angle is clearly shown, even though these two examples might be extremes. With the lack of detailed experimental procedure and actual observations of the contact angle, it is usually impossible to judge the values given by the different authors. The conclusion of this treatment

is that it is very interesting but that a series of experiments with the objective to test this relation must be carried out. A smooth solid, where no contact angle hysteresis is observed, must be used together with different liquids with a wide range of surface tension values.

Another method to find a relation between θ and γ_{LV} is to use Good's interaction parameter (103) which is defined as

$$\phi = \frac{\gamma_{SV}+\gamma_{LV}-\gamma_{SL}}{2\sqrt{\gamma_{SV}\gamma_{LV}}} \tag{3.12}$$

Combining Good's interaction parameter with Young's equation, leads to

$$\gamma_{SV} = \frac{\gamma_{LV}(1+\cos\theta)^2}{4\phi^2} \tag{3.13}$$

In simple cases, ϕ can be calculated from molecular properties of the two phases: the polarizabilities, dipole moments and ionization energies. Wu (104) used another approach to find γ_{SV} from this equation. He plotted a similar expression versus γ_{LV} based on a series of experimentally known values of θ and γ_{LV}. All the above methods are limited to systems where γ_{LV} is larger than γ_{SV}, which limit their use. Most estimations of surface tension of solid metals and oxides are in the range from about 500 to 2500 mJ/m^2 (105).

Several methods to estimate the surface tension of solids are based on experiments involving the mechanical destruction (cleavage, dispersion and so forth) of solids. McCammond et al. (106) found a clear relation between the fracture strength of glass rods and the polarity of the liquid in which the rods were tested. They related this relationship to the surface tension of the glass rods. A cleavage method for measuring surface tension of crystals was carried out by Gilman (95). The values of LiF and MgO were in good agreement with simple ionic lattice theory and the values for CaF, BaF, Si and Zn seem consistent with their binding energies.

A theory by Skapski (107) gives a relation between the surface tension of nonionic solids from the arrangement of their next neighbours, the heat of fusion, and the surface tension of the liquid at the melting point. A commonly used method is Udin's method (96) of zero creep in fine wires at temperatures over $0.9T_M$ (T_M=absolute melting temperature). The method involves the determination of the stress necessary to balance the contracting force set up by the surface tension.

A simple relation which has been widely used is Antonow's rule (108).

$$\gamma_{SL} = \gamma_{LV} - \gamma_{SV} \tag{3.14}$$

Combining this equation with Young's equation, leads to

$$\gamma_{SV} = \gamma_{LV}(1+\cos\theta)/2 \tag{3.15}$$

The correctness of this rule can be questioned because the above equation always gives values of γ_{SV} equal or smaller than γ_{LV}. It also predicts a direct relation between γ_{SV} and γ_{LV} which seems incorrect due to the generally accepted small values of the spreading pressure π (109). The spreading pressure is defined as

$$\pi = \gamma_S - \gamma_{SV}$$

where γ_S is the solid surface tension in vacuum. π is therefore the reduction in surface tension of the solid due to absorption of liquid.

3.6 Surface Tension of Molten Salt

Today, values of the surface tension of most pure molten salts are known. Theories to predict surface tension of pure salts are therefore more of theoretical than practical interest. Mayer and coworkers (110-113) developed a theory to calculate the surface tension of pure salts based on the molecular relationship between surface tension and compressibility and also from a theory of corresponding states. This molecular theory has given surface tension values close to the experimental values for certain salts, but the deviation from the experimental value is generally too large to give it any practical value.

Due to the large number of binary, ternary and quaternary molten salt systems of both theoretical and practical interest, it is of great value to have methods to estimate surface tension of different mixtures based on values for the pure salts and/or their binary mixtures.

When discussing experimental values of surface tension and different theoretical and empirical models, the accuracy limit of the experimental data must be considered. A recent study (114) was undertaken to determine the accuracy limits of the experimentally obtained surface tension values for a number of salts. For KNO_3 it was set to ±0.25% while for NaCl it was set to ±1.5% rather than the previously stated accuracy limit of ±0.1%. This difference in the accuracy limit might be due to the higher experimental temperatures for the NaCl measurements, but it might also be due to difficulties in purification of the NaCl.

3.6.1 Surface tension of mixtures

Surface tension is generally not expected to be an additive quantity as given by the relation

$$\gamma_{LV} = x_1 \cdot \gamma_1 + x_2 \cdot \gamma_2 \tag{3.16}$$

where x_1 and x_2 are mole fractions and γ_1 and γ_2 are the surface tension of the pure components. This behaviour is usually explained qualitatively by the fact that the surface layer of the liquid is enriched in the component of lower surface tension, thereby minimizing the free energy of the system.

According to Guggenheim (115), the following expression applies to the surface tension of an ideal solution of two components where a is the surface area per mole:

$$\exp(-\gamma_{LV} \cdot a/RT) = \sum_i x_i \cdot \exp(-\gamma_i \cdot a_i/RT) \tag{3.17}$$

Usually, the value of a is calculated by assuming equal packing density in the surface and bulk phase. This equation has been found to give reasonable estimates of binary and ternary alkali earth chloride mixtures (116) and in binary alkali halide systems (40), when mole fractions have been replaced by volume fractions [Φ],

$$\Phi = \frac{V_i \cdot x_i}{\sum_i V_i \cdot x_i} \tag{3.18}$$

and the surface area per mole is replaced by the surface area per mole anion-cation pair [A].

$$A = \left(\sum_i \Phi_i \cdot V_i\right)^{2/3} \tag{3.19}$$

With these modifications (40), this equation may be written as:

$$\exp(-\gamma_{LV}A/RT) = \sum_i \Phi_i \cdot \exp(-\gamma_i A_i/RT) \tag{3.20}$$

where $A_i = \left(\frac{M_i}{\rho_i}\right)^{2/3}$

Guggenheim (115) also derived an expression to calculate the surface tension of regular solutions:

$$\exp(-\gamma_{LV}a/RT) = \sum_i x_i \cdot \exp(-\gamma_i a/RT) \cdot \exp\left\{\frac{(1-x_i)^2 mw}{RT}\right\} \tag{3.21}$$

where w/RT=b is the regular solution interaction parameter and m expresses the number of neighbours in the adjant layer. When dealing with molten salt mixtures, however, it is generally accepted that nearest neighbours as well as next nearest neighbours will be changed during the mixing process. The regular solution formula is therefore not directly applicable.

In a different approach Eberhart (117) assumed the surface tension to be a linear function of the surface mole fractions y_i, i.e.,

$$\gamma_{LV} = \sum_i y_i \cdot \gamma_i \tag{3.22}$$

A separation factor, S, for the enrichment of the surface layer was defined as

$$S = \frac{b_1/b_2}{a_1/a_2} \tag{3.23}$$

where b and a are the activities in the surface layer and bulk liquid, respectively. Combining these two equations and assuming the activities to be equal to concentrations, he obtained the following expression:

$$\gamma_{LV} = \frac{Sx_1 \cdot \gamma_1 + x_2 \cdot \gamma_2}{Sx_1 + x_2} \tag{3.24}$$

The two dimensionless quantities ξ and R were defined as

$$\xi = \frac{\gamma_{LV} - \gamma_1}{\gamma_2 - \gamma_1} \tag{3.25}$$

$$R = \frac{x_2}{x_1} \tag{3.26}$$

Rearranging equation (3.25), one finds that a plot of ξ versus ξ/R should be linear with slope -S.

$$\xi = -S(\xi/R) + 1 \tag{3.27}$$

This method is therefore an interpolation formula and it has no relevance to correctness of the interpretation of S. A consequence of this model is that, if the surface tension is known for a mixture 1 and 2 and for 2 and 3 at the same temperature, then the surface tension of the mixture 1 and 3 can be calculated at the same temperature.

$$S(1,2)S(2,3) = S(1,3)$$

Grjotheim et al. (40) found that this model gave a very satisfactory fit to the experimental surface tension values for some alkali halide binary mixtures. They mentioned, however, that for systems with strong interactions as in the $MgCl_2$-Alk.Cl systems it may not be suitable.

Bertozzi et al. (42,118) found that the maximum deviation from linearity of the surface tension in charge symmetrical mixtures was a linear function of a size parameter D.

$$\gamma_{LV} = x_1 \cdot \gamma_1 + x_2 \cdot \gamma_2 - K \cdot x_1 \cdot x_2 \cdot D$$

$$D = \left(\frac{d_1 - d_2}{d_1 + d_2}\right)^2$$

d_1, d_2: cation-anion center distances

x_1, x_2: mole fractions

K : constant

In a later paper Bertozzi and Soldani (42) proposed that the size-charge parameter D given by Kleppa and Hersch (119) could be used to describe the surface tension values for mixtures of alkali earth halides and alkali halides.

$$D = \left[\left(\frac{r_1}{z_1} - \frac{r_2}{z_2}\right)/(d_1+d_2)\right]^2 \qquad (3.29)$$

Goodisman (120) developed a method to estimate the surface tension of molten salt mixtures which takes into account the effect of long-range coulombic forces. He claimed that these forces are of greater importance in lowering the surface tension of a mixture from the mean value, than the fact that the composition near the surface is enriched in the component of lower surface tension. By combining the effect of the enrichment with the effect of the long-range coulombic forces for a mixture with a common anion, he obtained the following expression:

$$\gamma_{LV} = \sum_i \left(\frac{\rho_i}{\bar{\rho}_i}\gamma_i - \gamma_i x_i\right) - \frac{RT}{a}\ln\left(\sum_i \cdot x_i \cdot \exp(-\gamma_i a/RT)\right) \qquad (3.30)$$

x_i = mol fraction of specie i

ρ = bulk density

$a = \rho^{-2/3}$

$\bar{V}_i$ = partial molar volume of specie i

$\bar{V} = \sum_i x_i \cdot \bar{V}_i$

$\rho_i = x_i/\bar{V}$ and $\bar{\rho}_i = 1/\bar{V}_i$

$\frac{\rho_i}{\bar{\rho}_i} = \phi_i$ (see (3.18))

This expression gives a very satisfactory fit of the experimental surface tension values for a series of alkali halide binary systems. However, this is not always the case and the deviation between the experimental and the calculated values, as shown below, is as large as 11%.

TABLE 3.1: Calculations of surface tension for various mixtures (after J. Goodisman (120)).

Systems	Measured surface tension (mJ/m^2)	Calculated surface tension (mJ/m^2)
0.5 KBr + 0.5 NaBr 1100 K	89.8	89.7
0.5 KBr + 0.5 CsBr 1073 K	76.2	76.4
0.5 KF + LiF 1173 K	152.0	169.0
0.2 KCl + 0.8 AgCl 1073 K	129.3	141.1
0.6 KCl + 0.4 AgCl 1073 K	103.5	110.4
0.45 CsCl +0.55 LiCl 1000K	88.2	97.2
0.5 NaCl + 0.5 LiCl 1100 K	115.7	116.8

3.7 X-Ray Radiography

As radiation of wave length passes through a material, the intensity is decreased exponentially with thickness according to the following equation.

$$I = I_o \exp(-\mu\rho x) \tag{3.31}$$

I_o = the initial intensity of the beam

μ = mass absorption coefficient of the material for a specific wavelength of X-ray

ρ = density of material

x = thickness

Contrast can be developed when the X-ray beam passes through materials of different densities, absorption coefficients or thickness. The contrast between two parts of a X-ray beam passing through two different materials A and B with same thickness x is given as

$$\text{contrast} = I_A/I_B = \exp[-((\mu\rho)_A-(\mu\rho)_B)x] \qquad (3.32)$$

Thus to maximize the contrast, materials of different absorptivity per unit length ($\mu\rho$) should be used and the thickness of the material should be as large as possible.

Because the absorption coefficient of lead is much larger than for sodium, potassium or lithium, liquids containing large amounts of $PbCl_2$ should be used to obtain high-contrast X-ray images of the sessile drop profile. For a given liquid, as low intensity X-rays (lower anode voltage) as practically possible should be used. This is due to the increase in the absorption coefficient for a given material with decreasing energy of the X-ray photons, and more X-ray photons are absorbed by the liquid drop. But a lower limit of the anode voltage is set by the thickness, density and absorption coefficient of the different construction materials through which the X-rays must also pass. The furnace was therefore constructed in such a manner to minimize the amount of X-ray absorbed by the construction materials.

Because of the non-rectangular shape of the sessile drop, the intensity of the X-ray beam passing through the drop will increase towards the outside edge (see Appendix ONE). This leads to lower contrast and a more diffused drop profile. The contrast due to this geometrical situation can be improved by decreasing the photon energy, but a lower limit exists as mentioned above.

CHAPTER 4

EXPERIMENTAL SECTION

4.1 Apparatus

The apparatus used in this study consists basically of three main units: a furnace, a X-ray source and an image recording system. A schematic diagram of the apparatus is shown in Figure 4.1.

Because of health hazards with the use of X-rays, the experiments were performed in a lead shielded room and all operations were performed from outside by remote control.

4.1.1 Furnace

A split graphite resistor furnace (121) was used as shown in Figure 4.2. This type of furnace was chosen because the graphite heating element absorbs only small amounts of high-energy X-rays and also because temperatures in excess of 1700°C can be obtained.

Argon gas with less than 10 ppm oxygen was purified with copper chips at 450°C and dried with drierite (anhydrous $CaSO_4$). This purified argon gas was used as an inert gas in the reaction tube. It was also used to fill the interior of the furnace to prevent reactions between the graphite heating element and oxygen.

In the preliminary studies, an alumina reaction tube with a wall thickness of a 2.5 mm was used. By replacing it with a quartz tube with wall thickness of 2.0 mm, the X-ray anode voltage could be reduced from about 65 kV to about 50 kV and higher contrast X-ray images were obtained. This tube could be evacuated or filled with any gas mixture

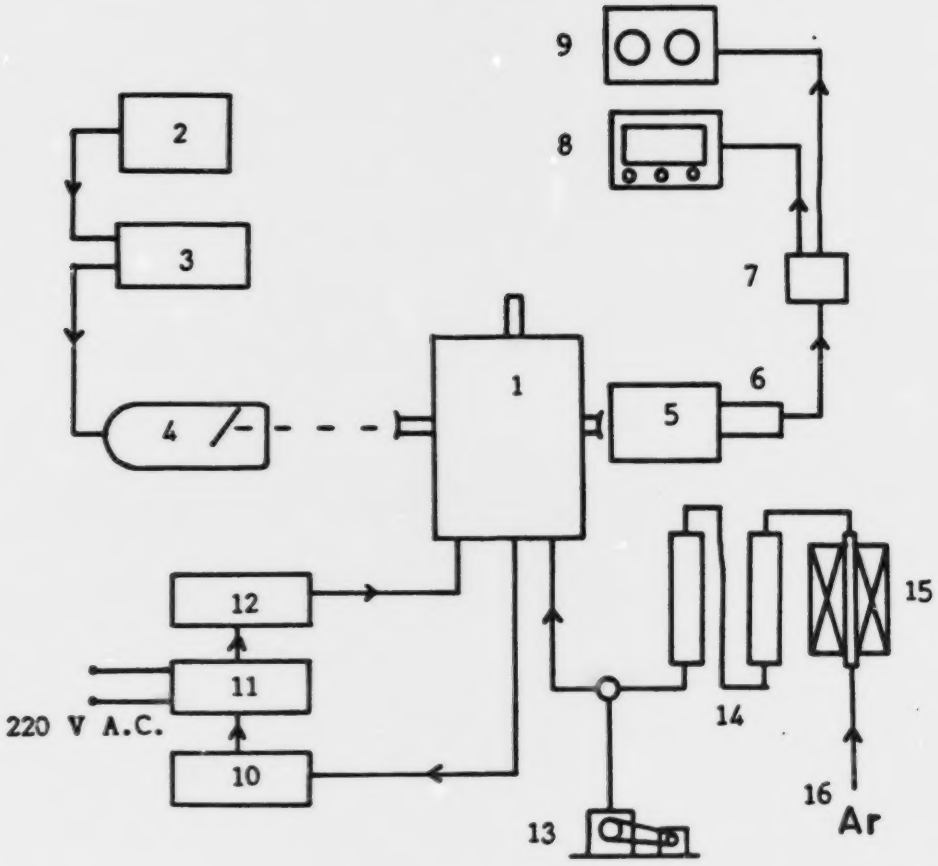

Figure 4.1. Schematic representation of X-ray radiographic apparatus.

1) Furnace, 2) X-ray controlling unit, 3) X-ray generator, 4) X-ray anode, 5) Image intensifier, 6) TV camera, 7) Electronic image distributor, 8) TV monitor, 9) Video recorder, 10) Temperature controller, 11) Power controller, 12) Step-down transformer, 13) Rotary pump, 14) Tubes filled with drierite, 15) Cu getter furnace, 16) Ar gas.

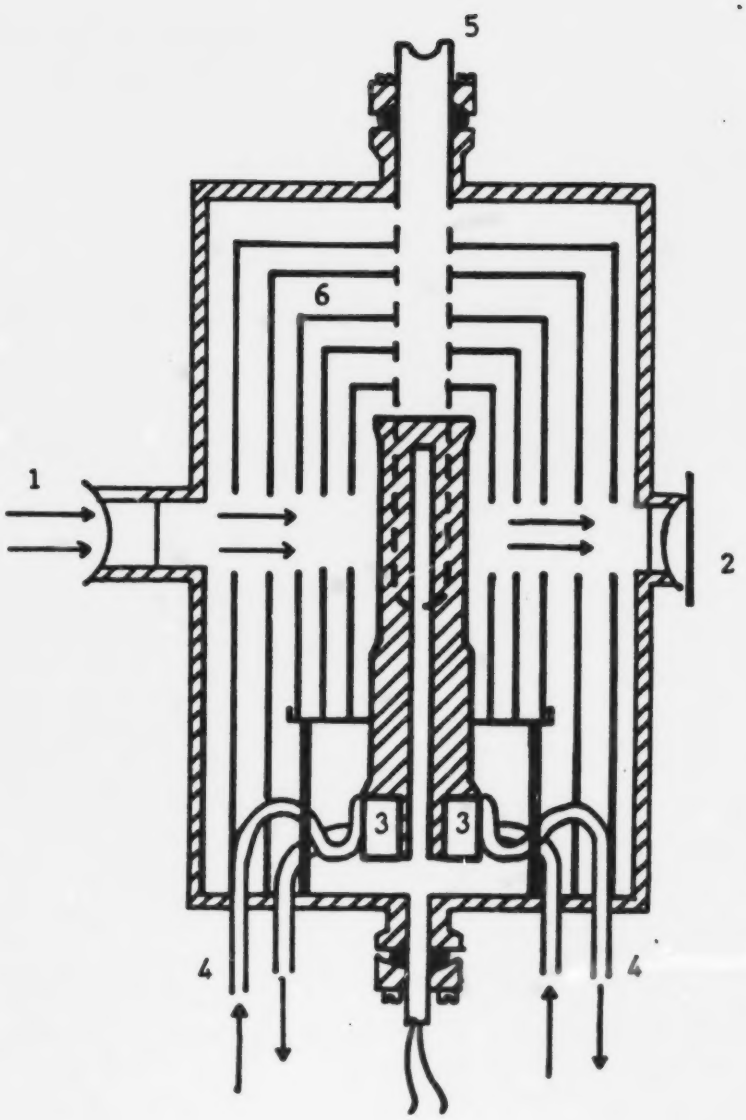

Figure 4.2. Split-tube graphite resistor furnace.

1) X-ray beam, 2) X-ray film, 3) Water-cooled copper clamps, 4) water-cooled copper tubing, 5) Quartz reaction tube, 6) Inconel and molybdenum radiation shields.

independently of the main furnace.

Five radiation shields of molybdenum and inconel were used to reduce the heat loss from the furnace. Spherical holes were cut in these shields to allow the X-ray beam to pass through. Pyrex windows on two sides of the furnace allowed the X-ray beam to pass through with relatively little absorption. Thin aluminum foil was used as a radiation shield to prevent the windows from heating up (see Figure 4.3).

The temperature controlling and power supplying system is shown schematically in Figure 4.4. Power was supplied to a $10/_1$ step-down transformer (max. 6.3 kW, 210 V, 30 A). The transformer was placed close to the furnace to minimize the power loss in the connecting leads. The transformer, the heating element's contact blocks and the outer furnace shell were all water-cooled. The maximum temperature fluctuation inside the furnace was found to be less than ±2 K at 1000 K and this temperature was maintained with a power input of about 3 kW.

The main disadvantage with this type of furnace is the relatively large temperature gradient in the vertical direction. Five horizontal slots were cut into the lower half of the heating element to decrease this gradient by minimizing the heat loss due to conduction down the element and to increase the electrical resistance in this lower and colder part of the heating element.

The sessile drop and the drop support were assumed to be at the same temperature due to the small size of both the drop and the support (Figure 4.5). Because of aging of the graphite heating element, the temperature profile changed slightly with time. The temperature profile in the region of the sessile drop was measured by three different thermocouples once every month.

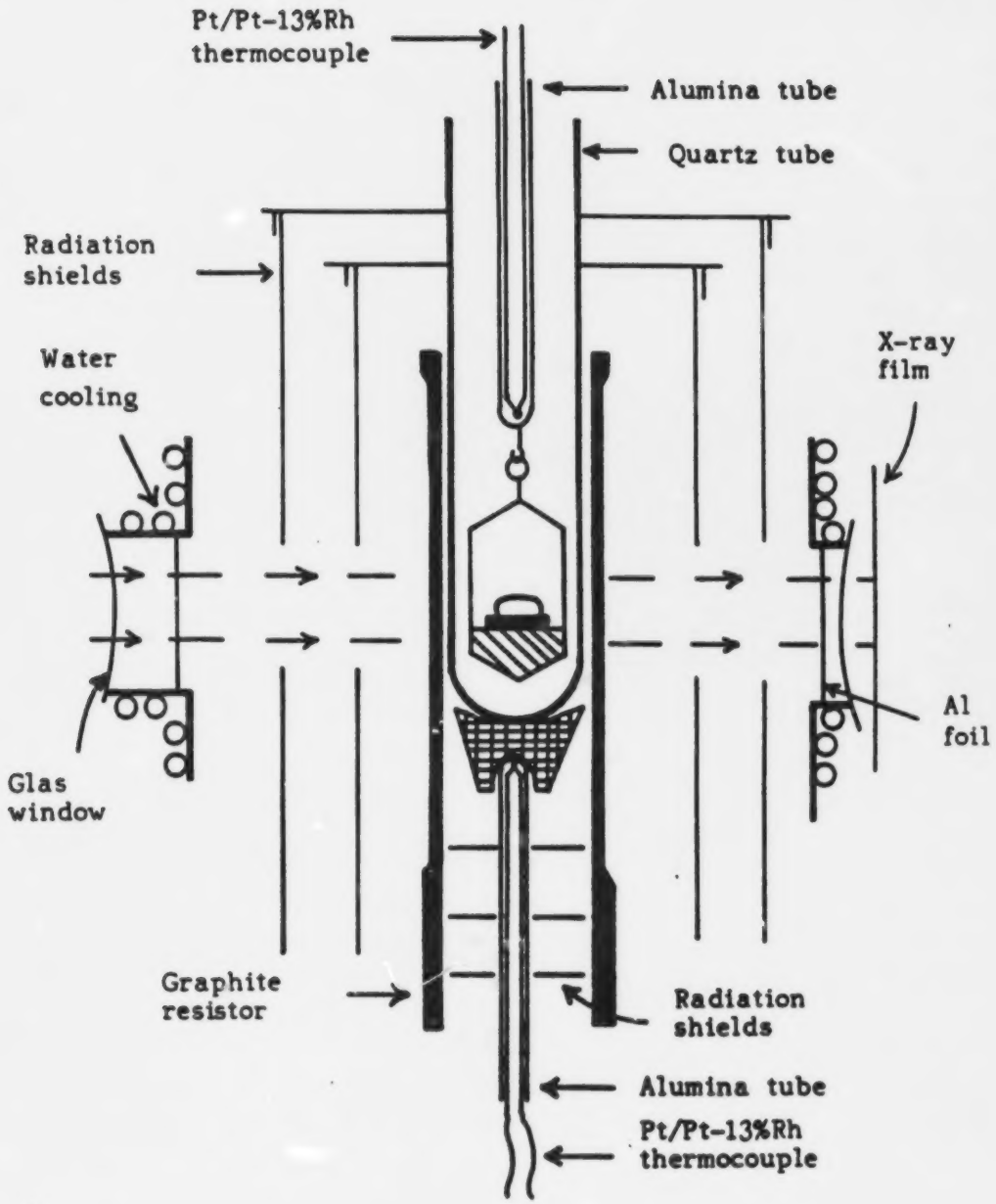

Figure 4.3. Schematic diagram of interior of the furnace.

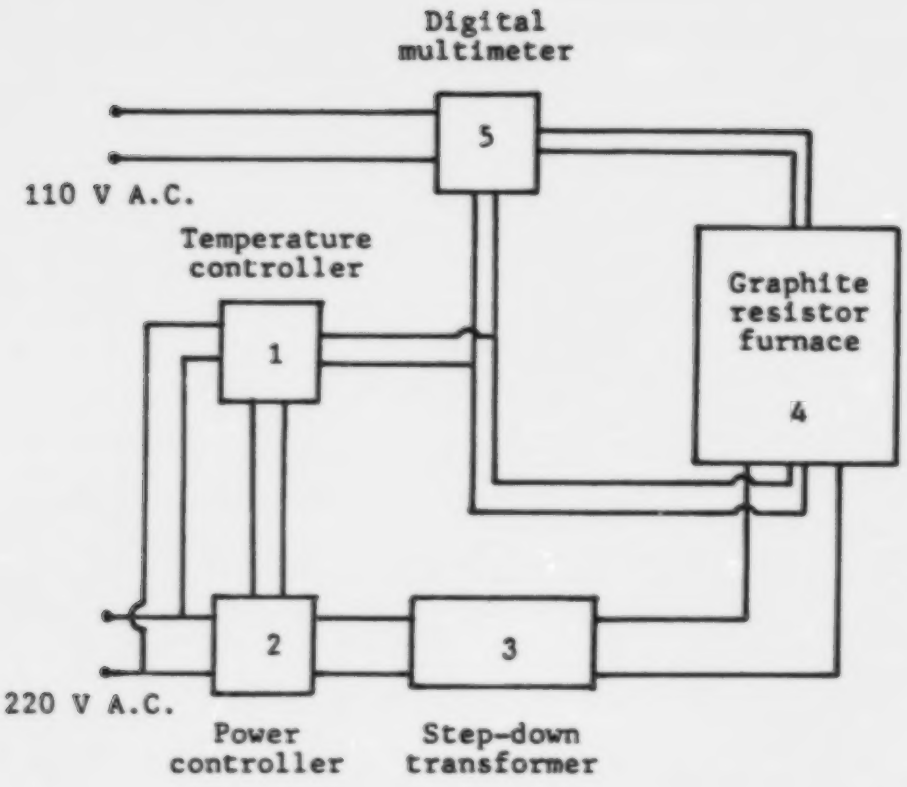

Figure 44. Schematic diagram of temperature controlling system.

1) P.I.D. temperature controller from Thermo Electric(360403117)
2) Phase/Amp series PA1 power controller from Halmar Electronics(Model number PA1-2450).
3) Water-cooled step-down transformer(10:1).
4) Graphite resistor furnace.
5) 160 Digital Multimeter, Keithley Instruments.

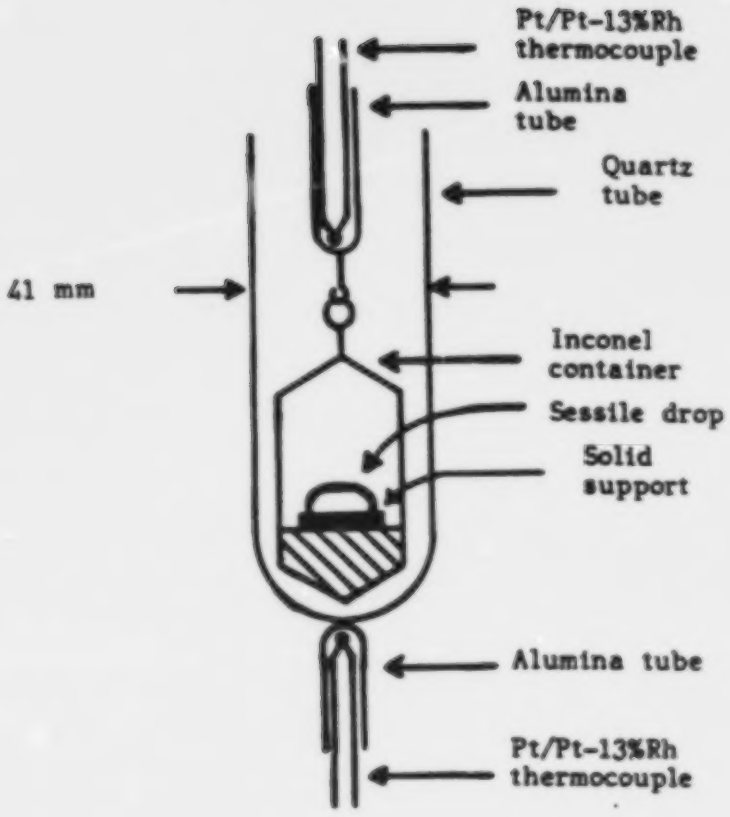

Figure 4.5. Experimental assembly for the sessile drop experiments.

The reproducibility in the temperature measurements was found to be within ±5 K, which also was assumed to be the uncertainty in the temperature measurements of the sessile drop.

4.1.2 Container for Sessile Drop

During the preliminary experiments, the sessile drop studies were carried out in graphite crucibles. It was difficult to polish the bottom of the cruicibles and to keep the base of the crucibles horizontal. Due to these problems, a new crucible design was made and tested as shown in Figure 4.5.

With this inconel container, small polished plaques could be placed on the horizontal support. Another advantage with this design was that the X-ray beam did not have to pass through any additional material such as crucible walls. Depending on the size of the sessile drop, it was possible to rotate the container up to about 90° to study the drop symmetry.

4.1.3 X-Ray Unit

The X-ray beam was generated by a medical type tube with a tungsten anode. Specifications for the X-ray anode are given in Appendix THREE.

The X-ray anode and the furnace were rigidly mounted on the same bench to avoid any accidental change in alignment. The distance between the X-ray anode and the object could be varied from 0.35 to 0.66 m, but the longest distance (0.66 m) was always used in these experiments. The direction of the X-ray beam could be varied both in the horizontal and vertical direction.

The central beam location was found by measuring the intensity while changing the beam direction. The intensity was found to be fairly uniform in the central region of the beam, and the position which gave the highest intensity was used.

The X-ray generator and control unit were located in a separate control room while the X-ray anode and the furnace were located in a small lead shielded chamber. This was necessary because the X-rays used in this work (40-90 kV) have very high ionization coefficients in biological tissues. X-ray leakages were checked by a standard X-ray dosimeter and radiation levels outside the chamber (< 0.1 $mR/_{hr}$) were well below the maximum value allowed by the International Commission on Radiological Protection (2.5 $mR/_{hr}$).

Radiation emanating from an "ideal" point source will show any point of the object as a point on the image. This is not so in practice because the focal spot of the X-ray tube has a finite area. Appendix ONE shows how this diffuse area (non-uniform intensity distribution) can develope, and Appendix TWO shows the intensity distribution when an ideal absorber is used as an object.

Because of the relatively large size of the focal spot (diameter ≥ 3.8 mm), pure resolution was obtained. In order to improve the image resolution, it was necessary to decrease the diameter of the focal spot. The effective focal spot was decreased by placing a lead pinhole of appropriate small diameter in front of the focal spot at the X-ray tube. Lead sheets with apertures of various diameters were tried and a hole diameter of 1.0 mm was found to give the best result with respect to both the resolution and the intensity of the beam.

This optimal hole diameter depends on other experimental conditions such as the type of X-ray film, the use of intensifying screens, object size, etc., but in this study a 1.0 mm diameter pinhole was always used.

4.2 The Image Intensifier Tube

Two important types of image intensifier tubes are available, (i) single field and (ii) dual field. In this study a dual field tube was used. With the dual field image intensifier tube, it is possible to change the degree of magnification of the output phosphor image. In fact the output phosphor image size is many times smaller than the input phosphor image, so it is more correct to speak of various degrees of minimization (79).

A dual field image intensifier is shown in Figure 4.6. In comparison with a single field type, it has an additional focussing system. When this additional electrode system is not used, the dual field intensifier behaves as a single field type. When the additional electrode is used, electrons from just the middle 5 cm diameter area of the input side are collected instead of those from the whole 7.2 cm diameter area.

The X-rays entering the input phosphor are those that have been transmitted by the system which is under study. This transmitted X-ray beam forms the initial image on the fluorescent layer forming the input phosphor. Cesium iodide is the material used as the input phosphor fluorescent layer, which emits blue on irradiation.

The photocathode adjacent to the input phosphor is excited by the input phosphor light emission and converts the light image into an electron image. The electrons are accelerated towards the output

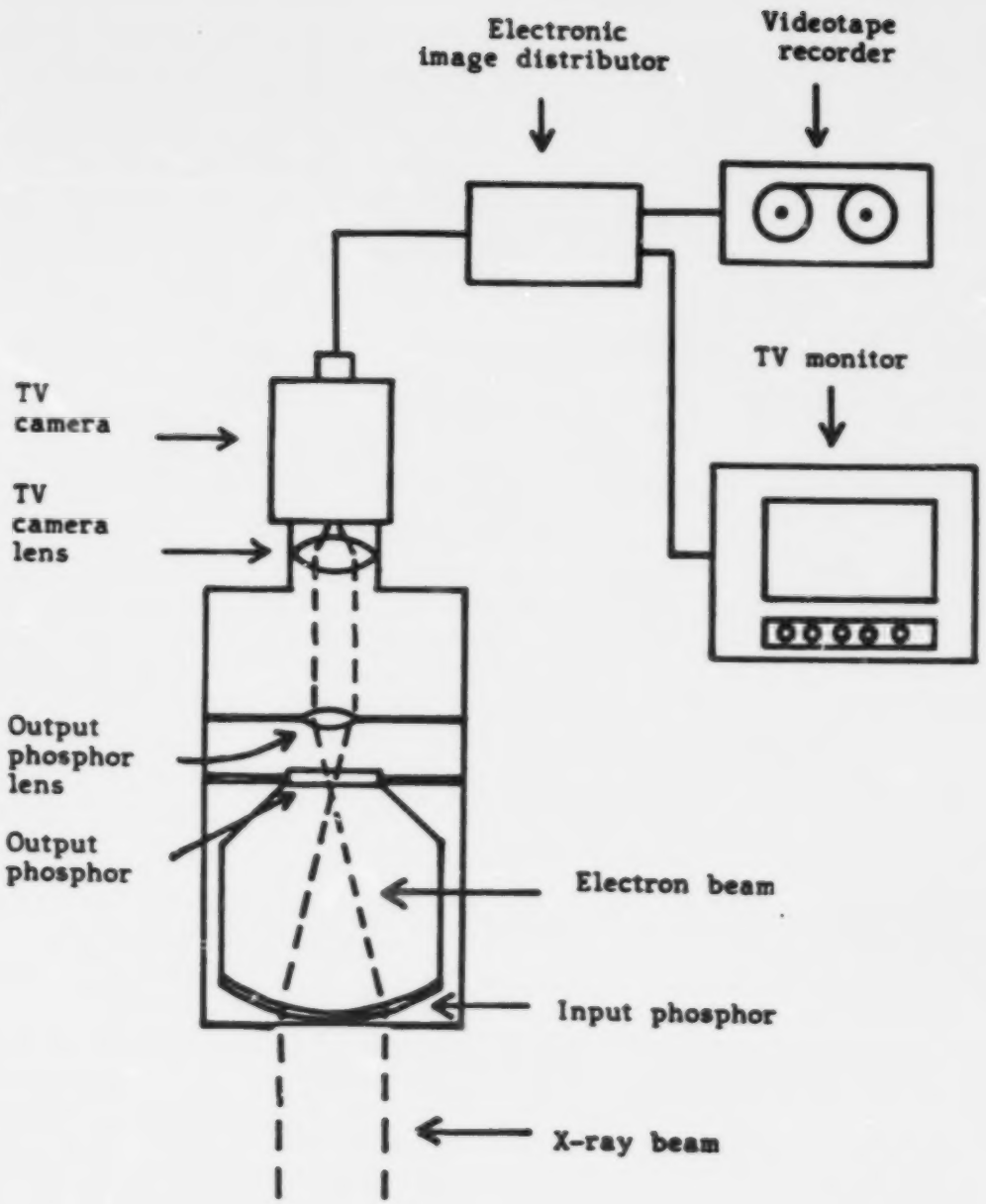

Figure 4.6. Photofluorography system.

phosphor upon which they are focussed under the influence of the focussing electrodes. The output phosphor is silver-activated zinc cadmium sulphide and fluoresces green. It is this image which is either photographed or displayed on a TV monitor via a TV camera. Since the output phosphor image is predominantly green, monochromatic film is not suitable to photograph it. Orthochromatic or panchromatic emulsion must be used.

Since virtually all the electrons collected from the input phosphor reach the output phosphor, the density of electrons per unit area at the output phosphor is much greater than at the input phosphor. Very approximately the brightness (intensity) of light at the input and output phosphors is proportional to the electron density per unit area. Thus the brightness of the image at the input phosphor will be much less than at the output phosphor. This light amplification is an important factor. The intensity of the X-ray beam does not need to be as high as in the case when an image intensifier is not used. This also means that the X-ray equipment can be used over a longer period of time without getting too hot. The exposure time for taking pictures with a film camera in combination with an image intensifier tube is much shorter than the time needed for taking pictures with a X-ray film.

4.3 Effect of the Photographic Emulsion on Resolution

The resolution of X-rays is potentially extremely high because of their very short wave-length, but we lose this resolution on the photographic plate. The quality of a picture on the plate is affected by the so-called adjacent effect. These phenomena are related with the developing of the high resolution plate and are well known (122).

Images at the grain boundary between a heavily exposed and a lightly exposed area may be affected by these effects. Near the boundary the diffusion of developer from the unexposed area will lead to a higher density of the film. The darker line on the high density side of the boundary is usually called a border effect, whereas the faint line within the low density part is referred to as a fringe effect (79). The actual image on the film and its resolution and contrast also depend on the properties of the film itself.

The use of high-speed intensifying screens decreases the image resolution even more (79), but their use decreases the exposure time considerably.

It was found that the factors which limited the resolution and the image quality in these experiments were the size of the focal spot, the non-rectangular shape of the object, the distance between the object and the film, the lower limit of the anode voltage and the physical properties of the liquid such as the density and the absorption coefficient.

4.4 Error Sources

The two main error sources in the sessile drop technique are drop distortions due to irregularities of the substrate surface and contaminations of the sessile drop liquid.

In order to derive the surface tension and the contact angle of a liquid drop, it is necessary to produce an image of the drop profile undistorted by any irregularities of the substrate surface. Such a profile can only be obtained when the drop possesses a well-

defined axis of symmetry. It is therefore very important that the solid plaque on which the seesile drop is formed, is properly prepared.

4.5 Preparation of Graphite Basal Support

Plaques with a thickness of about 3-5 mm were made from a graphite rod of 12.7 mm diameter. The density of the grapite was 1870 kg/m^3. Graphite plaques with a density of 1650 kg/m^3 were used in some preliminary experiments. Due to the large porosity and especially the large size of pores, contact angle hysteresis was observed. It was decided that further experiments with graphite plaques should only be carried out on plaques with a density of 1870 kg/m^3.

Figs. 4.7.1-4.7.4 show scanning electron microscope (SEM) pictures of polished plaques of graphite with a density of 1870 kg/m^3 and 1650 kg/m^3. Surface characteristics for plaques of these two different graphite qualities are shown in Appendix FOUR. These graphite plaques were polished with 1 μm alumina powder to a mirror-like finish and ultrasonically cleaned in water for about 5-10 hours. They were kept in 2N HNO_3 for about 24 hours to oxidize any metallic impurities on the surface (123) and ultrasonically cleaned in distilled water for another 5-10 hours.

The plaques were dried at 120°C under vacuum (1 kPa) for about 18 hours. It was later observed that sessile drops of liquids with high $PbCl_2$ content were covered with graphite powder and the contact angle decreased with time. Sessile drops of liquids without any $PbCl_2$ were found to be partially covered with graphite but in these cases no significant decrease in the contact angle was observed. This problem

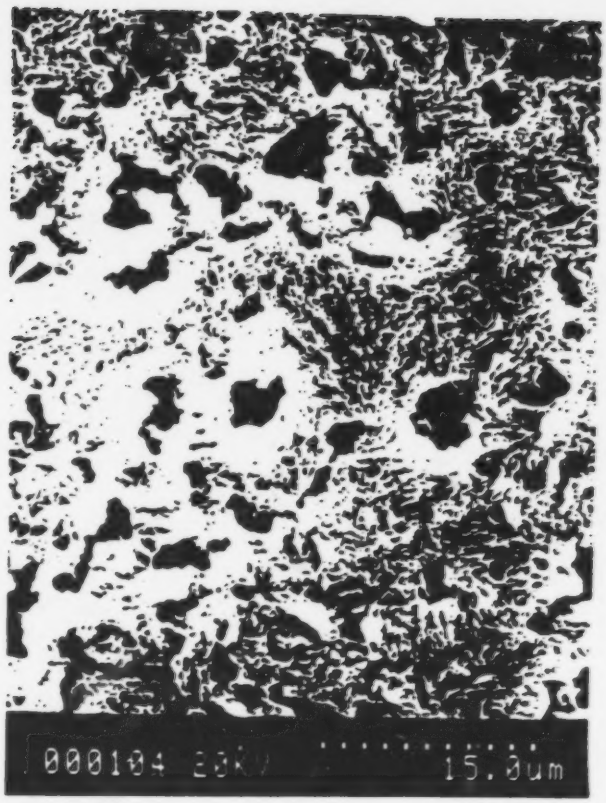

Figure 4.7.1.

SEM picture of the surface of a graphite plaque with a density of 1870 kg/m^3.
Magnification: 2000

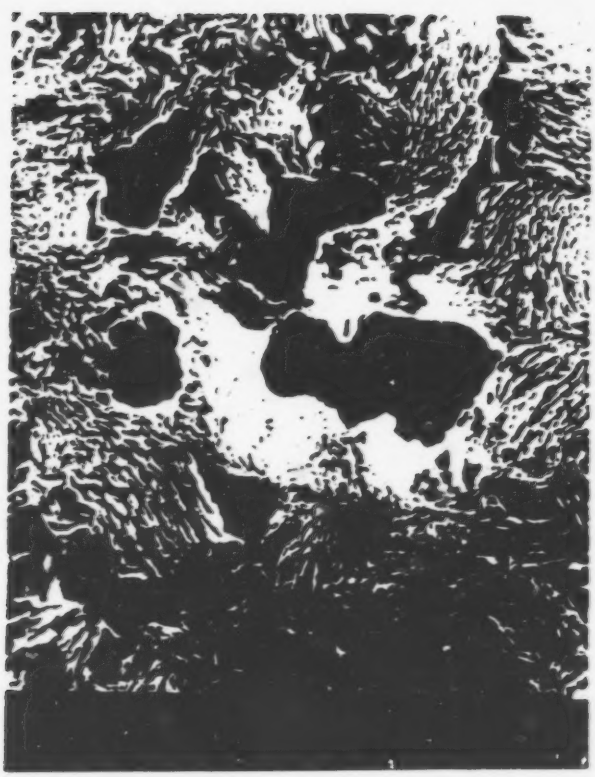

Figure 4.7.2.

SEM picture of the surface of a graphite plaque with a density of 1870 kg/m^3.
Magnification: 6700

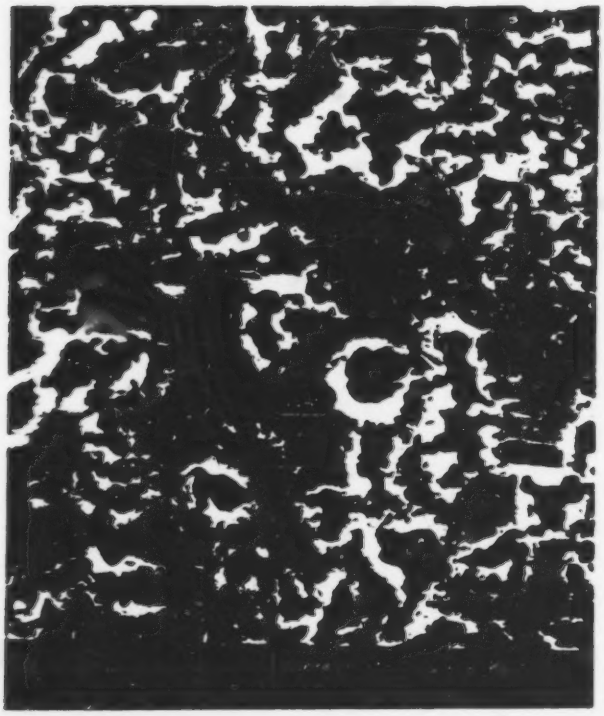

Figure 4.7.3.

SEM picture of the surface of a graphite plaque with a density of 1870 kg/m^3.
Magnification: 1200

Figure 4.7.4

SEM picture of the surface of a graphite plaque with a density of 1650 kg/m^3.
Magnification: 480

of graphite powder formation was avoided by incorporating an additional acetone wash treatment to the plaques.

After the drying process, the plaques were ultrasonically cleaned and then stored in acetone. They were taken out of the acetone and placed inside a desiccator for approximately 4 hours before an experiment. This procedure can be summarized as follows:

1 : polish with 1 μm alumina

2 : ultrasonically clean (distilled water)

3 : keep in 2N HNO_3 (24 hours)

4 : ultrasonically clean (distilled water)

5 : dry (120°C, 1 kPa, 18 hours)

6 : ultrasonically clean (acetone)

7 : store in acetone

8 : keep in dry air (3-4 hours)

9 : start experiment .

4.6 Preparation of Al_2O_3, SiO_2, ZrO_2 and BN Plaques

The SiO_2 plaques were cut from an 1/8 inch thick SiO_2 plate. They were very smooth and no surface polishing was necessary. The SiO_2 plaques were cleaned in acetone to remove any dirt or organic contaminates.

The Al_2O_3 and ZrO_2 plaques were polished with 1 μm alumina powder, followed by ultrasonically cleaning first in distilled water, then in acetone, and finally drying at 120°C in a vacuum furnace (1 kPa). Figs. 4.8.1 and 4.8.2 show SEM pictures of an Al_2O_3 plaque surface. Surface characteristics of a typical Al_2O_3 plaque are given in Appendix FOUR. The average grain size was found to be 7 μm.

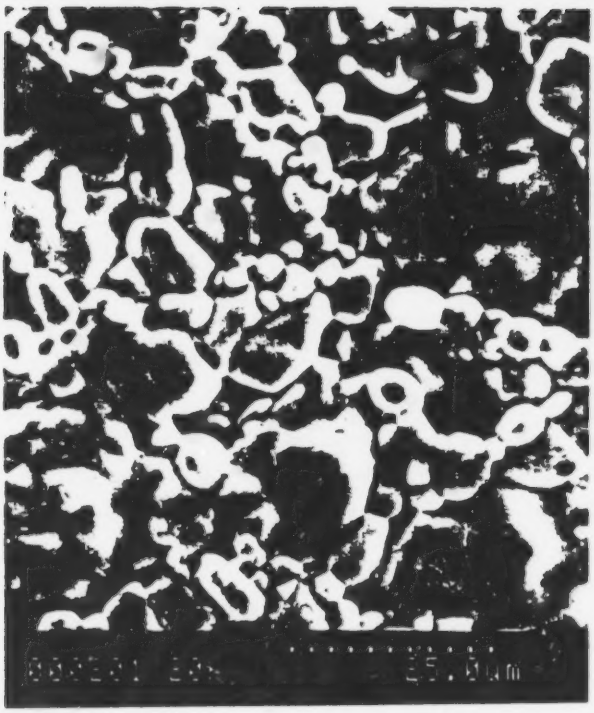

Figure 4.8.1.

SEM picture of the surface of a polycrystalline Al_2O_3 (alumina) plaque. Magnification: 1150

Figure 4.8.2.
SEM picture of the surface of a polycrystalline Al_2O_3 (alumina) plaque. Magnification: 4750

The surface of the ZrO_2 plaques was not completely smooth. Small cracks were observed in all ZrO_2 rods used to make the plaques. These cracks were on average 2-3 mm long and about 0.1 mm wide.

A BN rod of 16.9 mm diameter was used to make 3-5 mm thick plaques. The BN plaques were polished on a cloth with kerosene due to the hydroscopic nature of BN (124). Small cracks and pores were observed on the otherwise smooth surface. It was observed that liquid diffused into the plaques during the experiments because of the cracks and the porosity of the material.

4.7 Purification of Salt Mixtures

Reagent grade salts (Appendix FIVE) were weighed, mixed together and placed inside a quartz tube. This premixing was carried out because it was faster than separate purification of each salt and it reduced the number of operations necessary to purify the salt mixtures. Separate experiments showed that the weight loss, which occurred during a 3 hours period under a vacuum of about 1 Pa at 130°C for any of the pure salts, was less than 0.5%.

The salt mixture was then placed inside another quartz tube which was sealed off. This tube was first evacuated with a rotary pump and then evacuated to about 1 Pa with a molecular sieve pump (125).

Salt mixtures containing no $PbCl_2$ were heated up to about 400°C and kept under vacuum for about 20 hours to remove any moisture in the salts. Mixtures containing $PbCl_2$ were only heated to 150°C under vacuum to prevent any extensive loss of $PbCl_2$ due to vaporization. Chlorine gas (Cl_2) was then let into the tube and the salt mixture was melted.

Chlorine gas was bubbled through the melt for about 3 hours to remove any oxides and hydroxides. Purified argon gas was then bubbled through the melt for about 2 hours to remove any dissolved chlorine in the melt.

Finally, the melt was cooled rapidly by placing the outer quartz tube into a water bath and by flowing helium at a high flow rate, above the salt mixture. This solid salt mixture was taken out of the quartz tube and stored inside a desiccator containing phosphorus pentoxide. The purification system is shown in Fig. 4.9. It was found that for a salt mixture containing 40 mol % $PbCl_2$, the weight loss during the purification was less than 0.5%.

4.8 Experimental Procedure

The X-ray furnace was evacuated to 1 kPa and then filled with purified argon gas. To prevent any significant reaction between the graphite heating element and oxygen inside the furnace, this procedure was repeated twice before any heating of the furnace.

A purified plaque was taken out of the acetone and placed inside a desiccator about 4 hours before use. The required amount of salt mixture was removed from another desiccator and weighed shortly before use (5 min.). The purified plaque was placed inside the sample container (see Figure 4.5) and the salt mixture was placed on the center part of the plaque. The container was placed inside the quartz reaction tube which thereafter was sealed off and evacuated. Argon gas was admitted into the tube and then evacuated again. This was repeated 3 times before the salt was heated to about 150°C followed by another evacuation to about 1 kPa. Argon gas was let into the tube after about 1 hour and the salt was heated

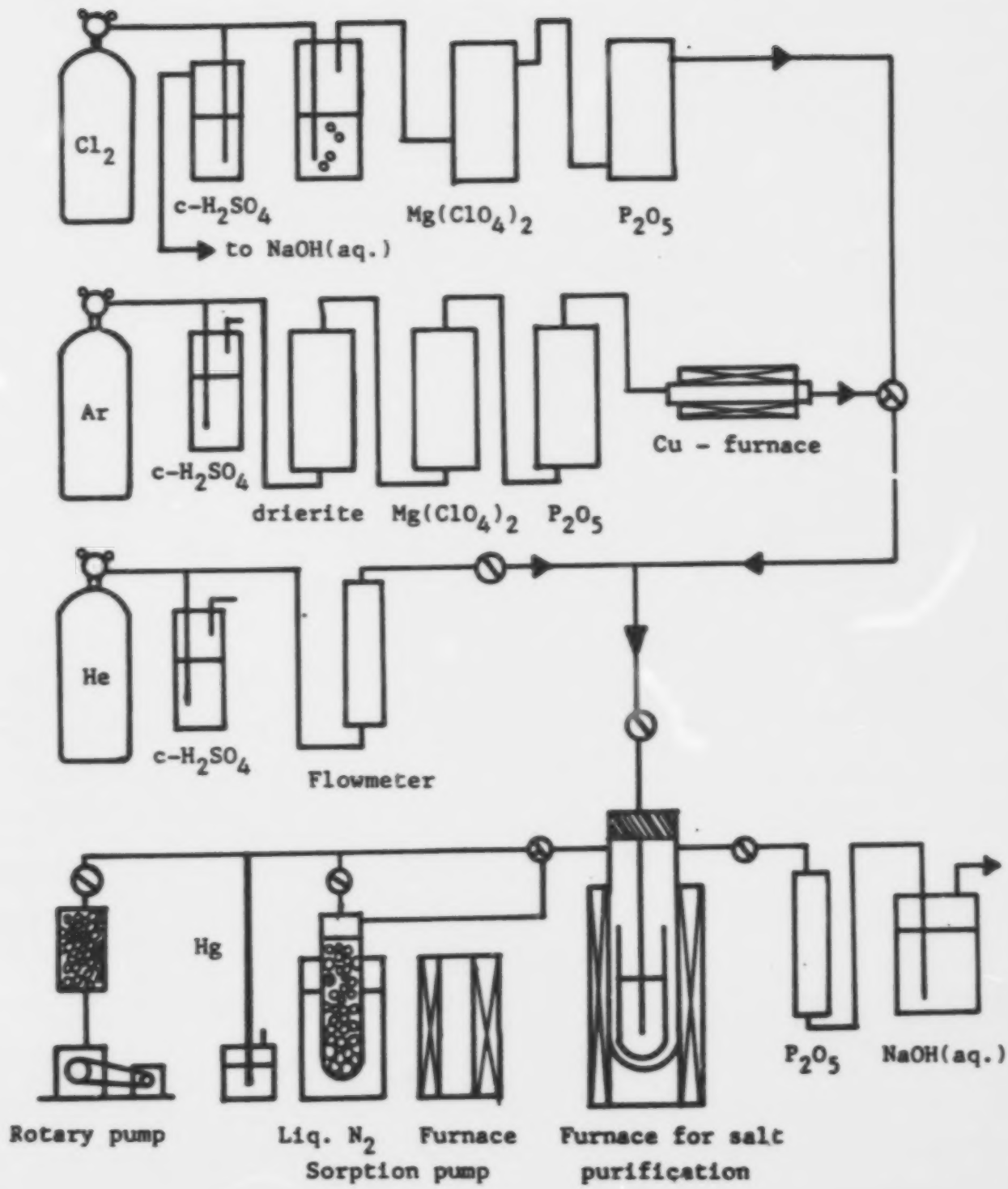

Figure 4.9. Purification system of salt mixtures.

to about 50°C above its melting point at a heating rate of 300°C per hour.

The position of the drop was checked with the TV monitor before any picture was taken. When an intensifying screen was used, a typical exposure time was 90 s at an anode voltage between 50 and 70 kV and anode current of 10 mA. Several pictures were taken in various configurations, sometimes with the drop in an unchanged position and sometimes after rotation of the drop.

The temperature effect on the contact angle was checked by taking pictures at different temperatures. The furnace was cooled down after finishing the experiment and argon gas was admitted into the furnace during the cooling, to maintain an excess pressure inside. The X-ray film was developed, following the recommendations of the manufacturer (5 min. in the developer and 5 min. in the fixer) and slides were made.

The image of the drop was magnified about 20-25 times with a photographic enlarger (Omega, Pro-Lab D6 4×5 enlarger), and the contact angle was measured with a protractor. An alternative method was to enlarge the image with the use of a slide projector in combination with a mirror. No significant difference in the contact angle was found using these two different methods. The reproducibility of the contact angle measurements was ±5°, and this is also assumed to be the accuracy limit. The diameter of the base of the drop was also measured because it was of interest to know if a change in contact angle also changed the base diameter.

The required coordinate points necessary to calculate the surface tension was found with the use of the latter method. About 30 coordinate points were recorded with the use of a digitizer. These coordinate points were later transferred to a Wylbur file (IBM, U of T Computer

Center), and the surface tension was calculated with the use of a computer program written in Fortran (61).

CHAPTER 5

RESULTS

The composition of the two ternary systems investigated are shown in Fig. 5.1. Phase diagrams of the $PbCl_2$-KCl-NaCl and the $PbCl_2$-KCl-LiCl ternary systems are shown in Appendix SIX. The compositional parameters 'y' and 't' are defined in the following way:

$$y = 1 - x_{PbCl_2}$$

$$t = \frac{x_{NaCl}}{x_{NaCl} + x_{KCl}} \qquad \text{or} \qquad t = \frac{x_{LiCl}}{x_{LiCl} + x_{KCl}}$$

where x_{PbCl_2}, x_{KCl}, x_{NaCl} and x_{LiCl} are mol fractions of the respective salts. The values of y selected were 0.0, 0.6 and 1.0. The values of t selected were 0.0, 0.5 and 1.0.

5.1 Contact Angle Measurements on Graphite

Ten different salt compositions were studied on graphite plaques with a density of 1870 kg/m^3. The measured contact angles are given in Table 5.1 as a function of time after melting of the corresponding salt mixture. Figures 5.2-5.9 show the contact angle plotted versus time for a series of these experiments with graphite. The composition is given in mol percent. The surface characteristics of these graphite plaques are given in Appendix FOUR while scanning electron microscope (SEM) pictures of these plaques are shown in Figs. 4.7.1-4.7.4. Sessile drops of different salt compositions formed on graphite plaques are shown in Figs. 5.10-5.13.

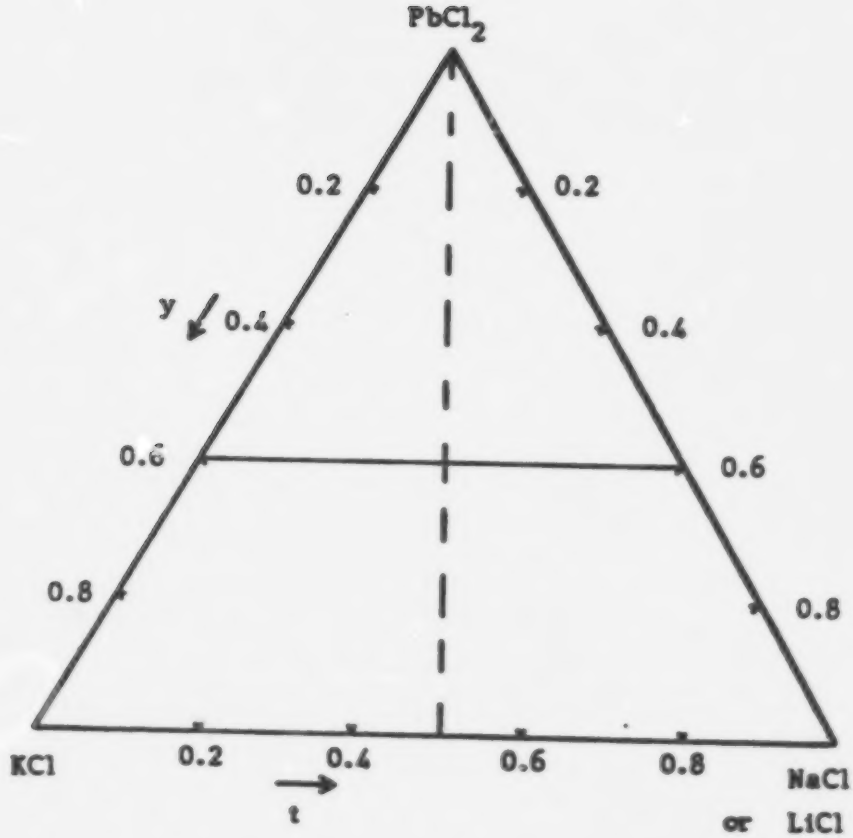

Figure 5.1. Selection of compositions for experiments.

Table 5.1. Contact angle of liquid $PbCl_2$-Alk.Chloride mixtures on graphite(Appendix FOUR) under an argon atmosphere.

Date	Composition(mol %) $PbCl_2$	KCl	NaCl	LiCl	Time (min.)	Temp. (K)	Density (kg/m^3)	Cont. Angle Left	Right	Ave.	Base Dia. (mm)
061082	100	0	0	0	2	823	4878	122	121	122	3.2
					13			105	100	103	3.7
					30			90	90	90	4.0
					58			78	85	82	4.0
					104			70	70	70	4.0
061082	100	0	0	0	2	823	4878	129	130	130	3.9
					17			115	115	115	4.3
					64			105	112	109	4.5
					83			100	105	103	4.5
220982	100	0	0	0	7	823	4878	140	136	138	4.9
					11			138	135	137	4.9
					32			125	123	124	5.0
					50	873	4803	110	112	111	5.1
					95			106	102	104	5.1
					190			92	93	93	5.3
					195			102	101	102	5.3
					248			98	97	98	5.4

Date	Composition(mol %) $PbCl_2$	KCl	NaCl	LiCl	Time (min.)	Temp. (K)	Density (kg/m^3)	Cont. Angle Left	Right	Ave.	Base Dia. (mm)
130882	100	0	0	0	4	800	4912	134	134	134	5.4
					9			118	117	118	5.7
					19			109	105	107	6.2
					28			101	100	101	6.7
					38			95	90	93	7.1
					59			90	85	88	7.4
					80			83	77	80	7.8
191082	0	100	0	0	5	1073	1511	137	133	135	4.1
					8			137	135	136	4.3
					25			135	132	134	4.3
					77			135	130	133	4.3
					89			137	133	135	4.5
130982	0	100	0	0	3	1073	1511	134	130	132	3.9
					5			130	125	128	3.9
					21			121	117	119	4.1
					25			120	114	117	4.1
					45			112	110	111	4.2
					68			112	108	110	4.3
					105			105	100	103	4.5
051082	0	0	100	0	3	1093	1546	120	115	118	4.3
					6			130	110	120	4.4
					21			117	110	114	4.4
					53			125	130	128	3.9
					120			110	120	115	4.3

Date	Composition(mol %) $PbCl_2$	KCl	NaCl	LiCl	Time (min.)	Temp. (K)	Density (kg/m^3)	Cont. Angle Left	Right	Ave.	Base Dia. (mm)
151082	0	0	100	0	2	1093	1546	143	140	142	4.3
					5			145	140	143	4.3
					19			145	145	145	4.2
					60			135	130	133	4.7
021082	0	0	0	100	6	923	1490	140	140	140	4.0
					9			135	135	135	4.0
					20			135	136	136	4.1
					50			140	135	138	4.2
240982	40	60	0	0	5	823	3120	135	140	138	5.5
					15			135	140	138	5.5
					32			131	132	132	5.5
					41			131	138	135	5.5
					56			131	138	135	5.6
					69	783	3170	132	138	135	5.6
					83			131	138	135	5.6
					134			130	133	132	5.7
					140			142	141	142	5.7
					270			134	135	135	5.8

Date	Composition(mol %) $PbCl_2$	KCl	NaCl	LiCl	Time (min.)	Temp. (K)	Density (kg/m^3)	Cont. Angle Left	Right	Ave.	Base Dia. (mm)
290982	40	60	0	0	3	783	3170	150	145	148	3.7
					7			150	145	148	3.7
					11			149	143	146	3.7
					19			150	143	147	3.7
					29	823	3120	150	145	148	3.7
					60			147	140	144	3.9
					75	873	3070	148	140	144	3.8
300982	40	0	60	0	5	923	3136	132	137	135	4.8
					18			120	135	128	5.0
					25			135	130	133	4.8
					110			112	115	114	5.0
					120			113	115	114	5.0
					160			110	119	115	5.1
					170			112	120	116	5.0
081082	0	50	50	0	5	953	1592	140	135	138	3.4
					10			137	135	136	3.4
091082	0	50	0	50	17	793	1620	139	141	140	4.1
051082	40	30	0	30	6	673	3406	148	145	147	4.9
					10			143	140	142	4.8
					18			143	140	142	5.0
					30			150	135	143	6.0
					48	723	3308	146	135	141	6.2
					94	673	3406	140	125	133	6.2

Date	Composition(mol %) $PbCl_2$	KCl	NaCl	LiCl	Time (min.)	Temp. (K)	Density (kg/m^3)	Cont. Angle Left	Right	Ave.	Base Dia. (mm)
041082	40	30	30	0	3	823	3195	150	145	148	5.5
					8			143	140	142	5.7
					12			138	138	138	5.7
					18			140	137	139	5.7
					23			143	140	142	5.6
					53	873	3148	145	140	143	5.7
					72	823	3195	145	140	143	5.7
071082	40	30	30	0	5	793	3224	135	135	135	3.8
					8			140	137	139	3.8
					12			137	137	137	3.9
					82			135	133	134	3.9
					87			130	130	130	3.9

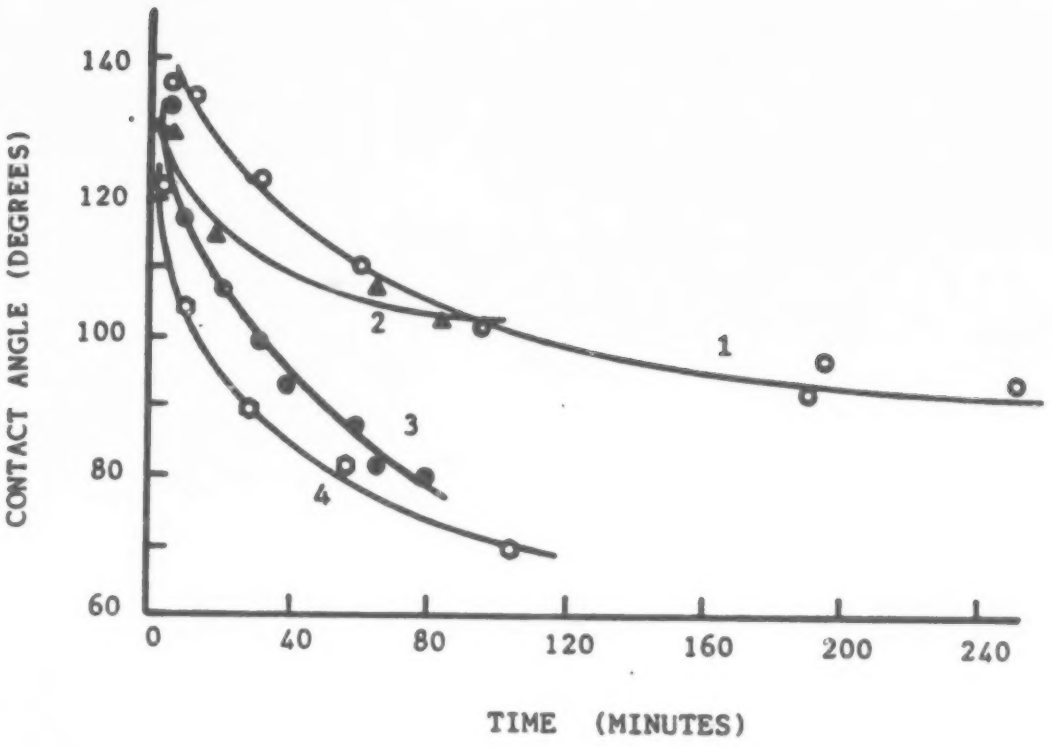

Figure 5.2. Contact angle versus time on graphite under argon atmosphere.

Salt composition; $PbCl_2$

Curve 1; date 220982, Temp.= 823 K, 873 K
Curve 2; date 061082, Temp.= 823 K
Curve 3; date 130882, Temp.= 800 K
Curve 4; date 061082, Temp.= 823 K
Solid support; graphite, density = 1870 kg/m^3.

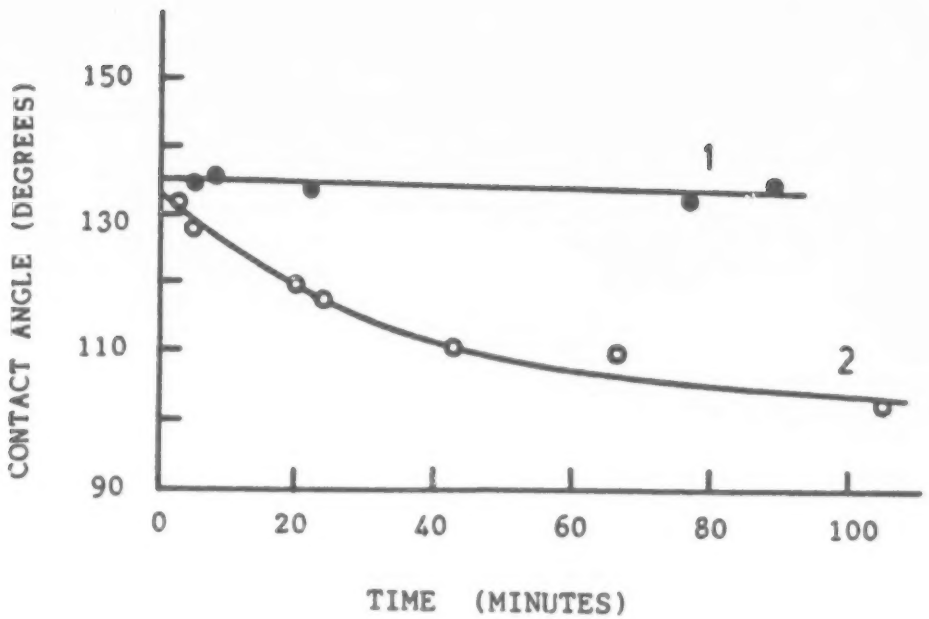

Figure 5.3. Contact angle versus time on graphite under argon atmosphere.

Salt composition; KCl

Curve 1; date 191082, Temp.= 1073 K
Curve 2; date 130982, Temp.= 1073 K
Solid support; graphite, density = 1870 kg/m^3.

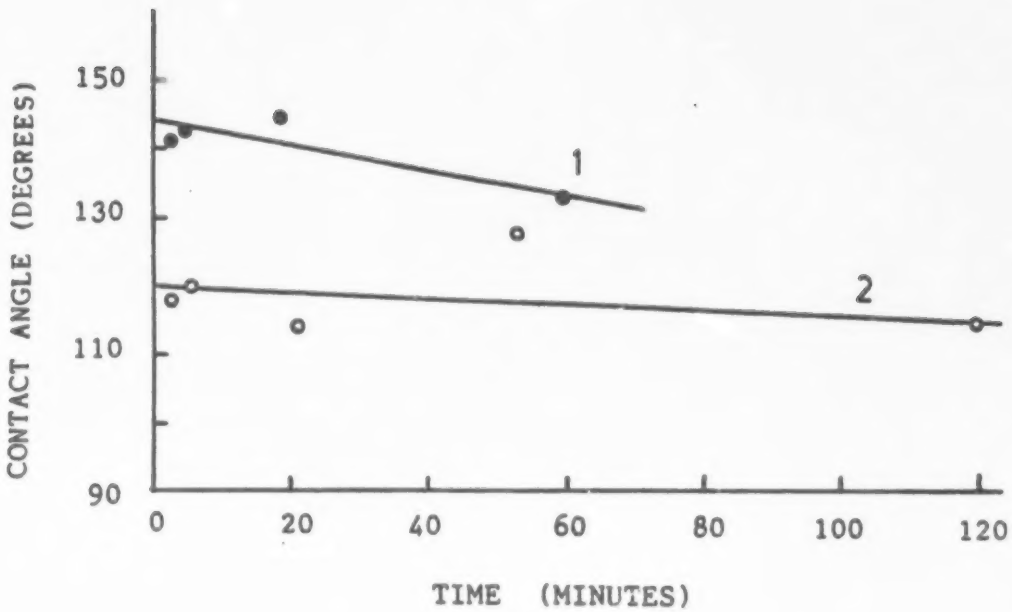

Figure 5.4. Contact angle versus time on graphite under argon atmosphere.

Salt composition; NaCl

Curve 1; date 151082, Temp.= 1093 K
Curve 2; date 051082, Temp.= 1093 K
Solid support; graphite, density = 1870 kg/m^3.

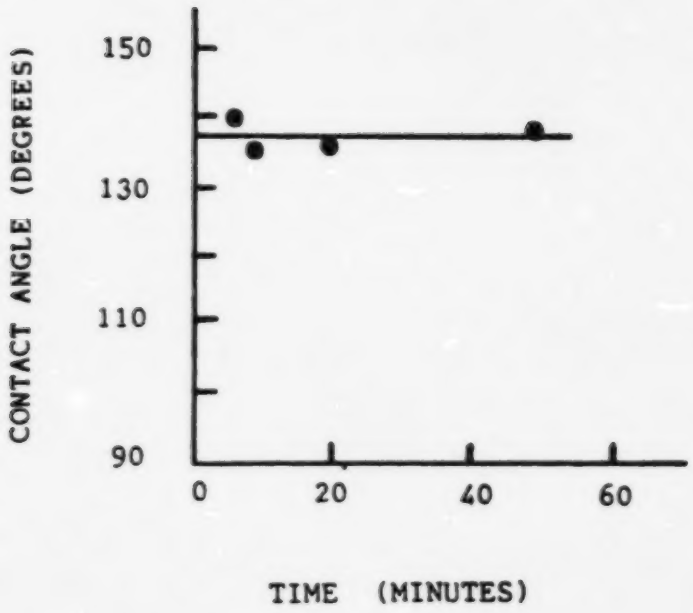

Figure 5.5. Contact angle versus time on graphite under argon atmosphere.

Salt composition; LiCl

Date 021082, Temp.= 923 K

Solid support; graphite, density = 1870 kg/m^3.

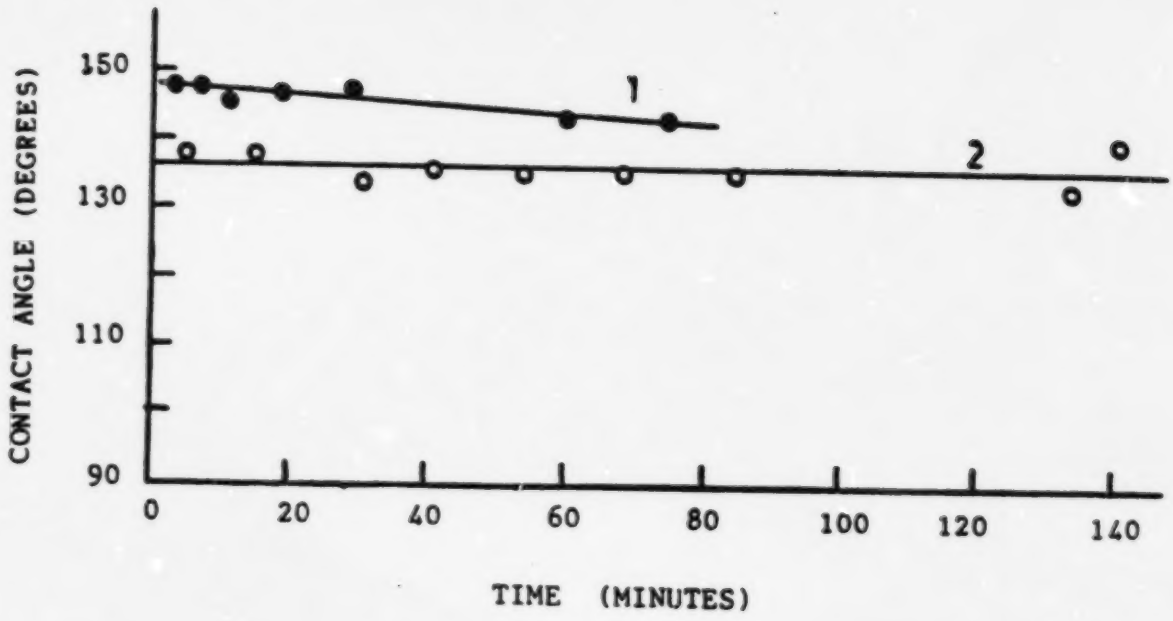

Figure 5.6. Contact angle versus time on graphite under argon atmosphere.

Salt composition; $PbCl_2$:KCl(40:60)

Curve 1; date 290982, Temp.= 783 K, 823 K, 873 K

Curve 2; date 240982, Temp.= 823 K, 783 K

Solid support; graphite, density = 1870 kg/m^3.

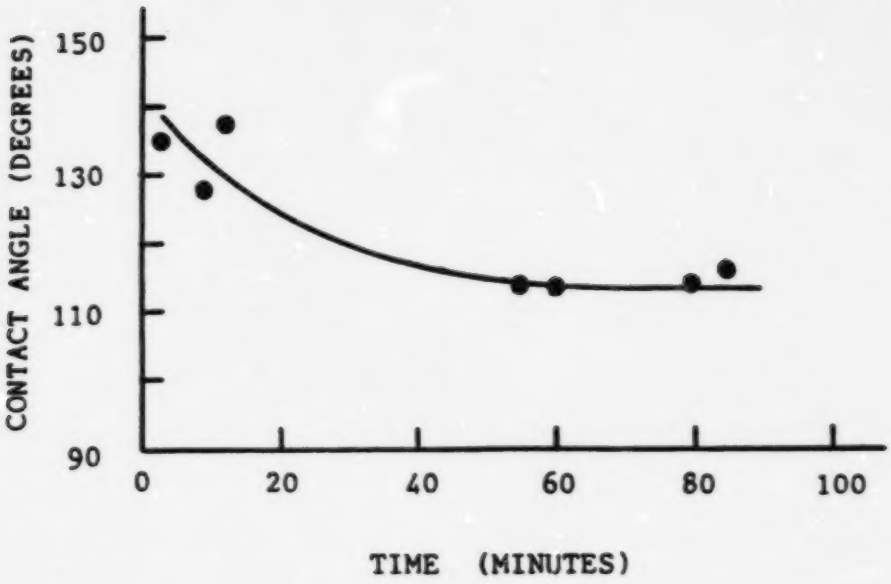

Figure 5.7. Contact angle versus time on graphite under argon atmosphere.

Salt composition; $PbCl_2$:NaCl(40:60)

Date 300982, Temp.= 923 K

Solid support; graphite, density = 1870 kg/m^3.

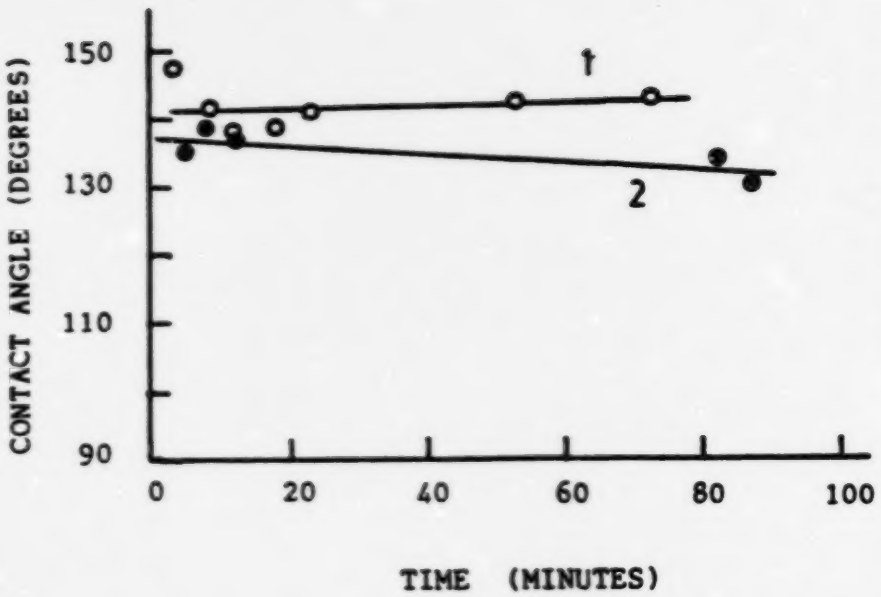

Figure 5.8. Contact angle versus time on graphite under argon atmosphere.

Salt composition; $PbCl_2$:KCl:NaCl(40:30:30)

Curve 1; date 041082, Temp.= 823 K, 873 K

Curve 2; date 071082, Temp.= 793 K

Solid support; graphite, density = 1870 kg/m^3.

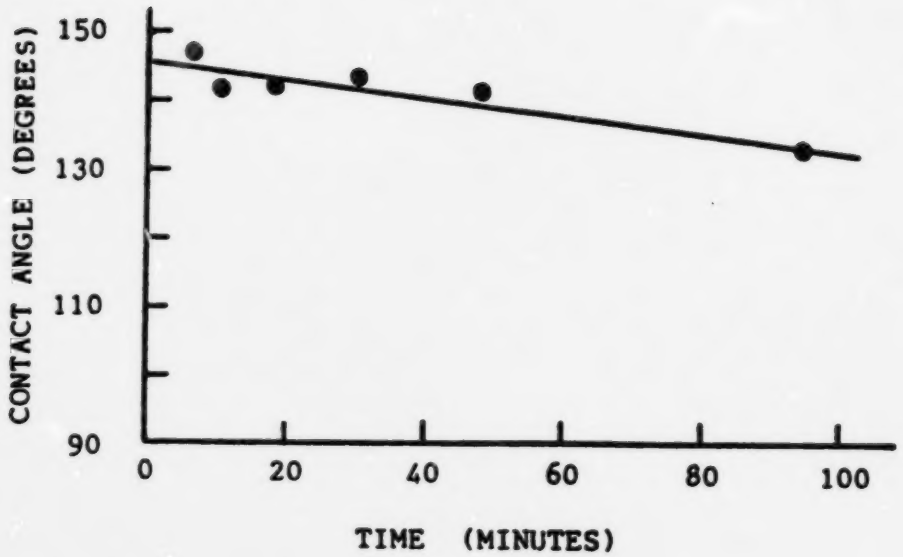

Figure 5.9. Contact angle versus time on graphite under argon atmosphere.

Salt composition; $PbCl_2$:KCl:LiCl(40:30:30)

Date 051082, Temp.= 673 K, 723 K, 673 K

Solid support; graphite, density = 1870 kg/m^3.

Figure 5.10. Sessile drop of KCl on graphite under argon atmosphere.

Salt composition; KCl
Graphite support, density = 1870 kg/m^3.
Temp. = 1073 K . Magnification: 8.8

Figure 5.11. Sessile drop on graphite under argon atmosphere.

Salt composition; $PbCl_2$-NaCl(40:60 mol %)
Graphite support, density = 1870 kg/m^3.
Temp. = 923 K . Magnification: 14

Figure 5.12 Sessile drop on graphite under argon atmosphere.

Salt composition; $PbCl_2$:KCl:LiCl(40:30:30 mol %)
Graphite support, density = 1870 kg/m^3.
Temp. = 673 K . Magnification: 13

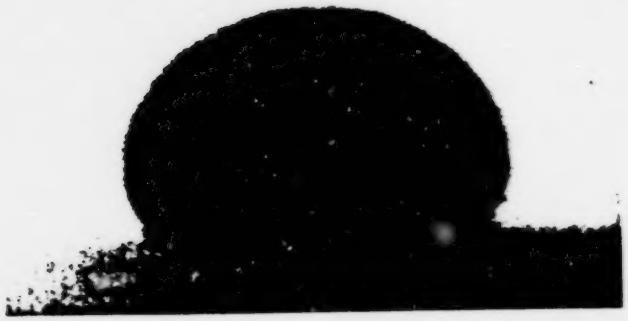

Figure 5.13. Sessile drop on graphite under argon atmosphere.

Salt composition; $PbCl_2$:KCl:NaCl(40:30:30 mol %)
Graphite support, density = 1870 kg/m^3.
Temp. = 793 K . Magnification: 8.9

For best reproducibility of the contact angle measurements, the same-size drops should be used (76). The base diameter of the different drops were therefore measured together with the contact angle and is also given in Table 5.1. No clear dependency can be found between the drop size and the contact angle from these measurements. A common trend, however, was that as the contact angle decreased with time, the base diameter increased. This increase in base diameter was small (< 5%) for all salt compositions studied with the exception of pure $PbCl_2$.

For experiments with $PbCl_2$ on graphite, the base diameter is plotted versus the contact angle in Fig. 5.14. The base diameter increased with decreasing contact angle (with increasing experimental time) for all experiments. It can also be seen that the advancing contact angle (the first measured contact angle) increases with increasing drop size up to a certain size. For drops with a base diameter smaller than about 5 mm the contact angle decreased with decreasing base diameter.

The proposed mechanism for the decreasing contact angle is that the liquid advances over the graphite surface due to vibrations or due to changes in the surface and interfacial tensions. For two of the experiments with $PbCl_2$, the base diameter became constant after some time and independent of the decreasing contact angle. This effect was observed for the smallest drops, which also have the largest area to volume ratio, and the effect can be explained by the decreasing amount of liquid due to evaporation of $PbCl_2$.

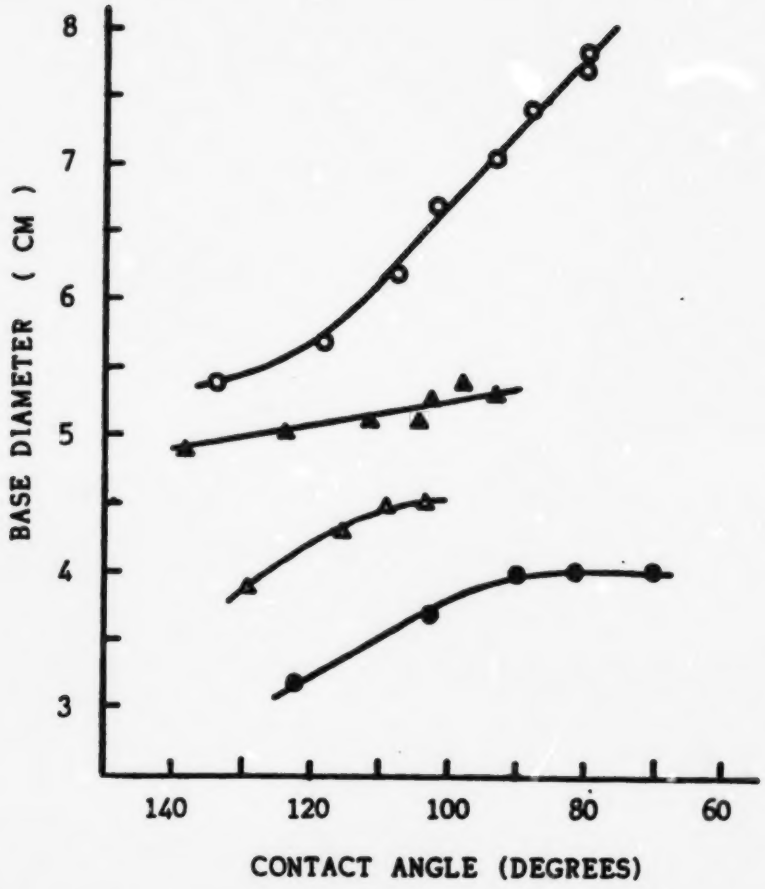

Figure 5.14. Base diameter versus contact angle for experiments with sessile drop of pure $PbCl_2$ on graphite under argon atmosphere.

5.2 Contact Angle Measurements on Al_2O_3, SiO_2, ZrO_2, BN and Inconel

Table 5.2 summarizes the contact angle measurements performed on Al_2O_3, SiO_2, ZrO_2, BN and inconel. The Al_2O_3, SiO_2 and inconel plaques are all wetted by the salt mixtures studied. With increasing time, the contact angle approached 20° in all these experiments. Two SEM pictures of the polycrystalline alumina plaque are shown in Figs. 4.8.1 and 4.8.2 and the grain size distribution is shown in Appendix FOUR. Sessile drops on BN and Al_2O_3 for different salt mixtures are shown in Figs. 5.15 and 5.16.

Table 5.2. Contact angle of liquid $PbCl_2$-Alk.Chloride mixtures on different solid supports under an argon atmosphere.

Date	Composition(mol %) $PbCl_2$	KCl	NaCl	LiCl	Solid Plaque	Time (min.)	Temp. (K)	Density (kg/m^3)	Cont. Angle Left	Right	Ave.	Base Dia. (mm)
011082	0	0	0	100	Al_2O_3	10	923	1490	20	20	20	11.4
060982	0	0	100	0	Al_2O_3	10	1093	1546	15	15	15	
060982	0	100	0	0	Al_2O_3	10	1073	1511	15	15	15	
020982	100	0	0	0	Al_2O_3	13	823	4878	15	15	15	
211082	0	0	0	100	SiO_2	5	923	1490	15	15	15	
						20			15	15	15	
241082	0	0	100	0	SiO_2	4	1093	1546	15	15	15	
231082	0	100	0	0	SiO_2	10	1073	1511	15	15	15	
						22			15	15	15	
241182	100	0	0	0	SiO_2	13	823	4878	15	15	15	
081082	40	30	0	30	SiO_2	6	673	3406	15	15	15	
						90			15	15	15	
231182	40	30	0	30	SiO_2	10	693	3386	122	125	124	4.7
						17			(120 - 40)			
						42			15	15	15	

Date	Composition (mol %) $PbCl_2$	KCl	NaCl	LiCl	Solid Plaque	Time (min.)	Temp. (K)	Density (kg/m^3)	Cont. Angle Left	Right	Ave.	Base Dia. (mm)
011082	0	0	0	100	ZrO_2	3	923	1490	35	35	35	8.0
						30			20	20	20	8.3
170982	100	0	0	0	ZrO_2	2	823	4878	90	93	92	5.0
						6			90	90	90	5.1
						11			82	83	83	5.3
						25			80	80	80	5.3
						37			80	80	80	5.3
						117			75	76	76	5.4
						180			68	68	68	5.3
130982	0	100	0	0	Inconel	10	1073	1511	15	15	15	
150982	0	0	100	0	Inconel	3	1093	1546	15	15	15	
021082	0	0	0	100	Inconel	8	923	1490	25	25	25	
						30			20	20	20	
130982	100	0	0	0	BN	5	823	4878	91	70	86	6.7
						63			70	63	67	6.8
						102			60	60	60	6.7
202882	0	50	50	0	BN	15	953	1592	100	110	105	6.1
160982	0	50	0	50	BN	13	793	1620	77	90	84	7.1
						132			85	85	85	7.1

Figure 5.15. Sessile drop on BN under argon atmosphere.

Salt composition; KCl:NaCl(50:50 mol %)
Solid support, BN
Temp. = 953 K . Magnification: 14.6

Figure 5.16. Sessile drop on Al_2O_3 under argon atmosphere.

Salt composition; $PbCl_2$ (100 mol %)
Solid support, polycrystalline Al_2O_3
Temp.= 823 K . Magnification : 8

5.3 Surface Tension Measurements

Surface tension measurements were carried out for the $PbCl_2$:KCl:NaCl(40:30:30 mol %) and the $PbCl_2$:KCl:LiCl(40:30:30 mol %) ternary systems. The obtained values are given Table 5.3 and the measured coordinate points with the corresponding Laplace curves are shown in Figs. 5.17-5.21. The density values used to calculate the surface tension are given in Appendix SEVEN. The density is given as the density difference between the liquid and the gas in the computer plots (Figs. 5.17-5.21).

For the ternary containing NaCl, the surface tension was found to be 117 mJ/m^2 with a standard deviation of 7.5 mJ/m^2 at 793 K. This value is the average value found from two different photographs taken 12 minutes after each other. For the ternary containing LiCl, the surface tension was found to be 96.2 mJ/m^2 with a standard deviation of 1.4 mJ/m^2 at 673 K. This value was found from several measurements of the same photograph.

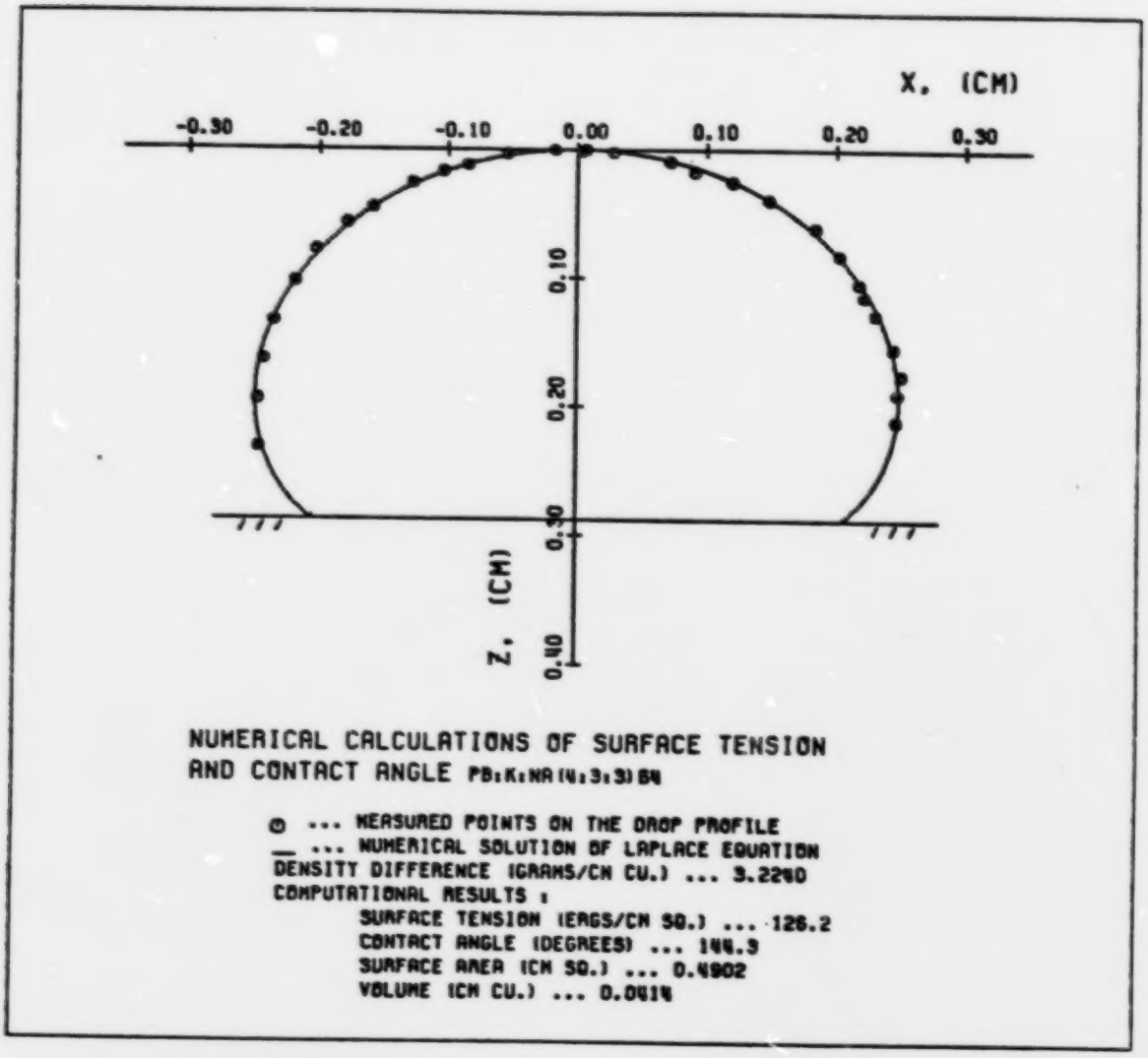

Figure 5.17. Surface tension of $PbCl_2$-KCl-NaCl(40:30:30 mol %) at 793 K.

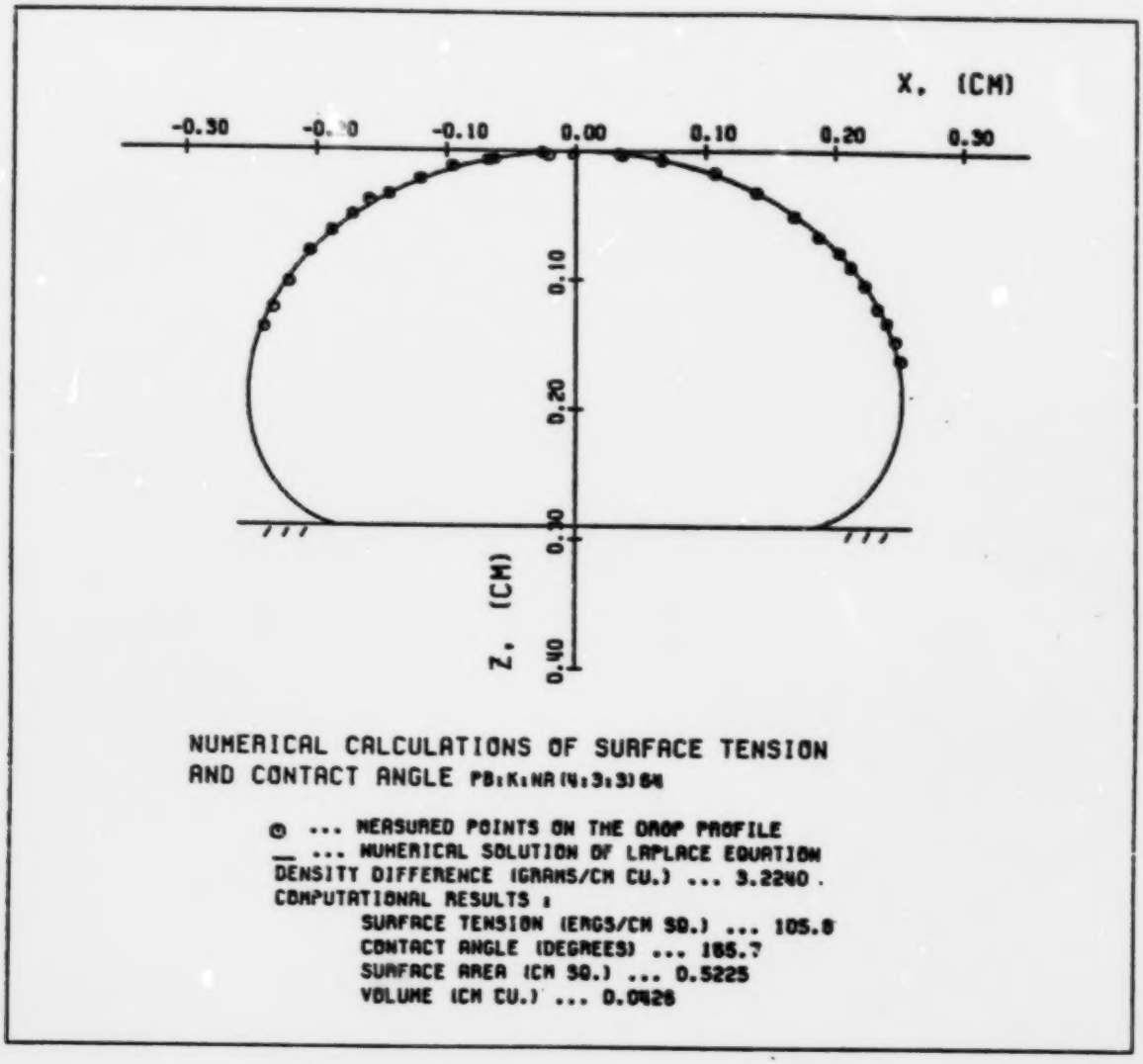

Figure 5.18. Surface tension of $PbCl_2$-KCl-NaCl(40:30:30 mol %) at 793 K.

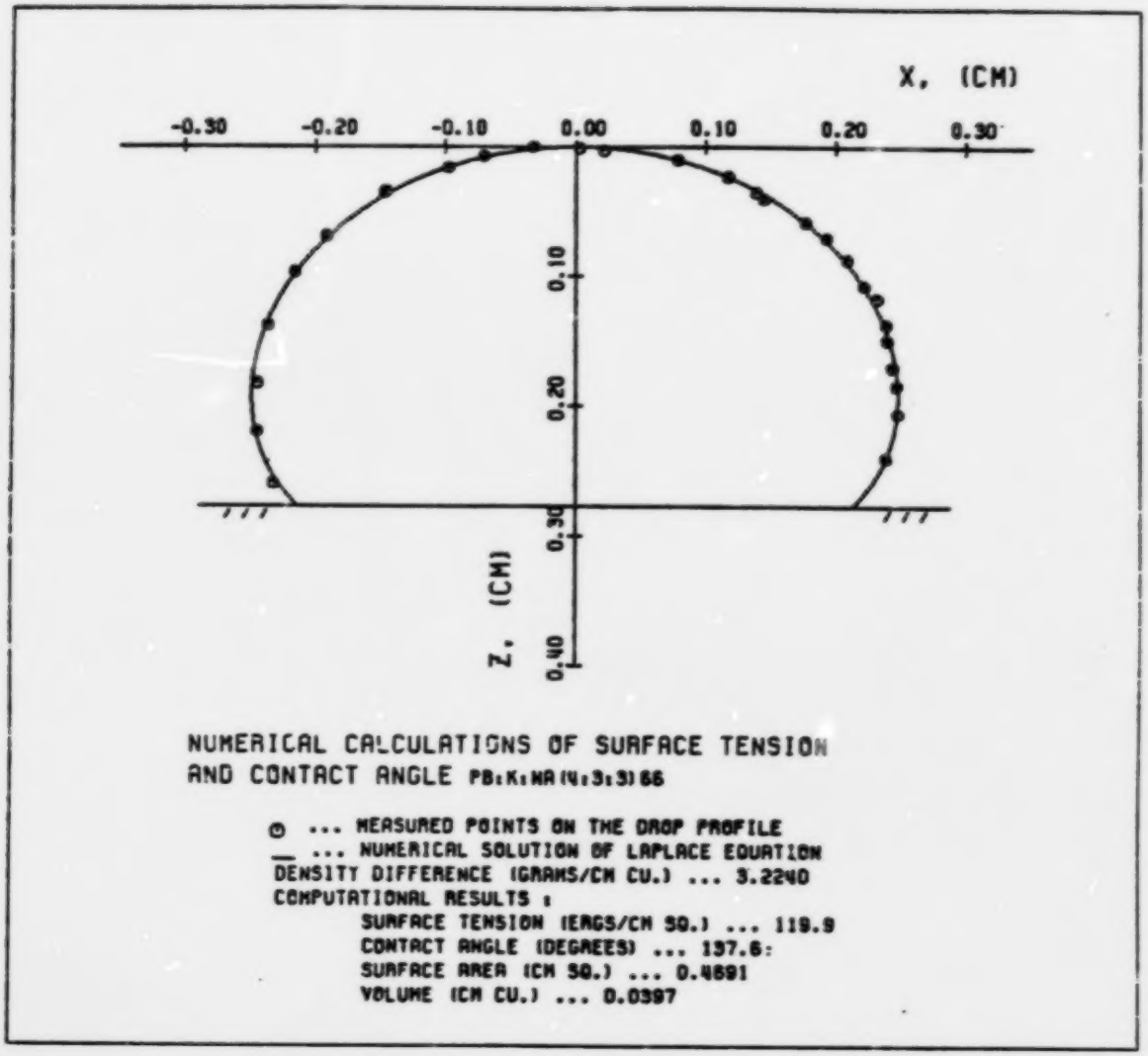

Figure 5.19. Surface tension of $PbCl_2$-KCl-NaCl(40:30:30 mol %) at 793 K.

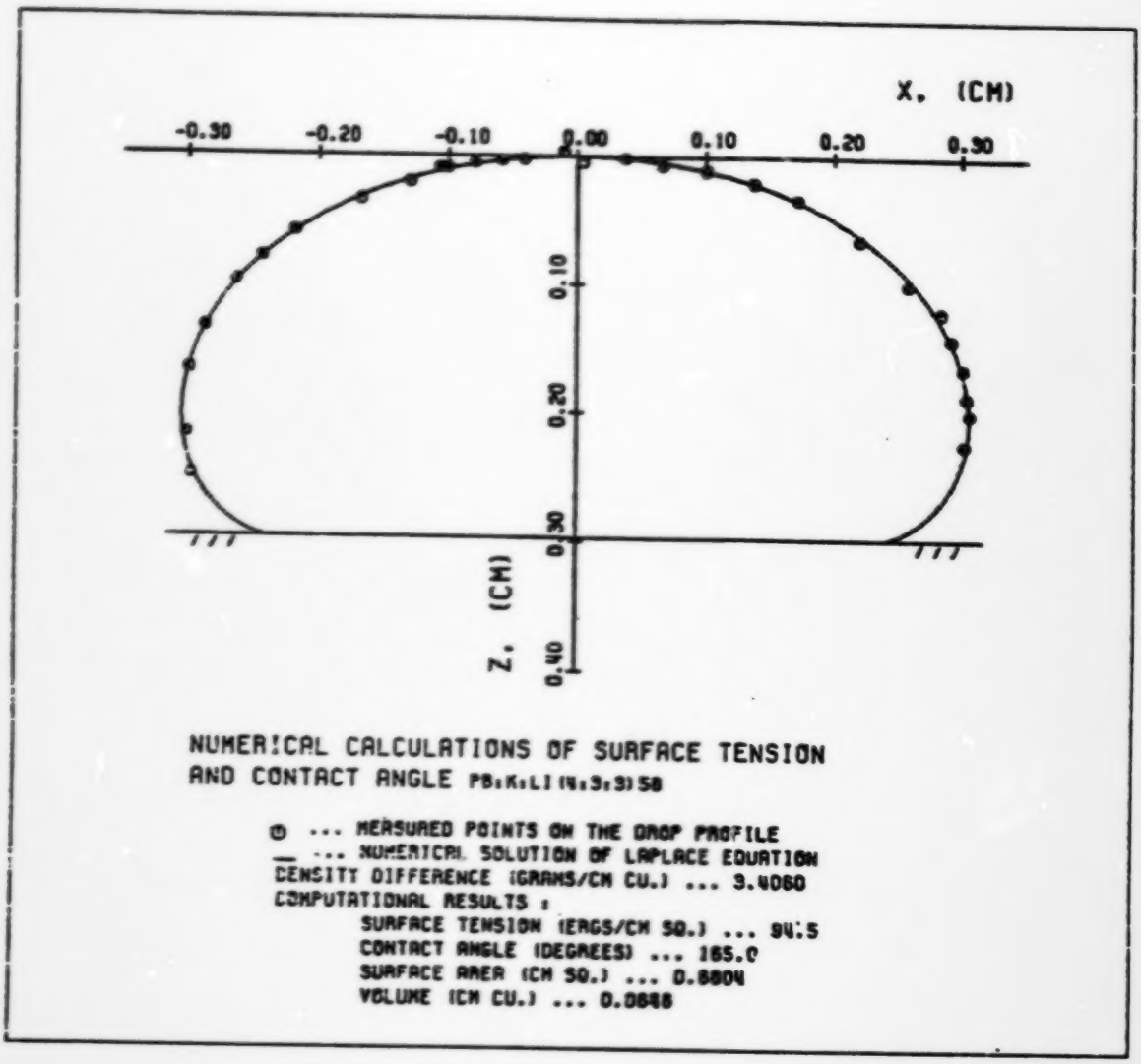

Figure 5.20. Surface tension of $PbCl_2$-KCl-LiCl(40:30:30 mol %) at 673 K.

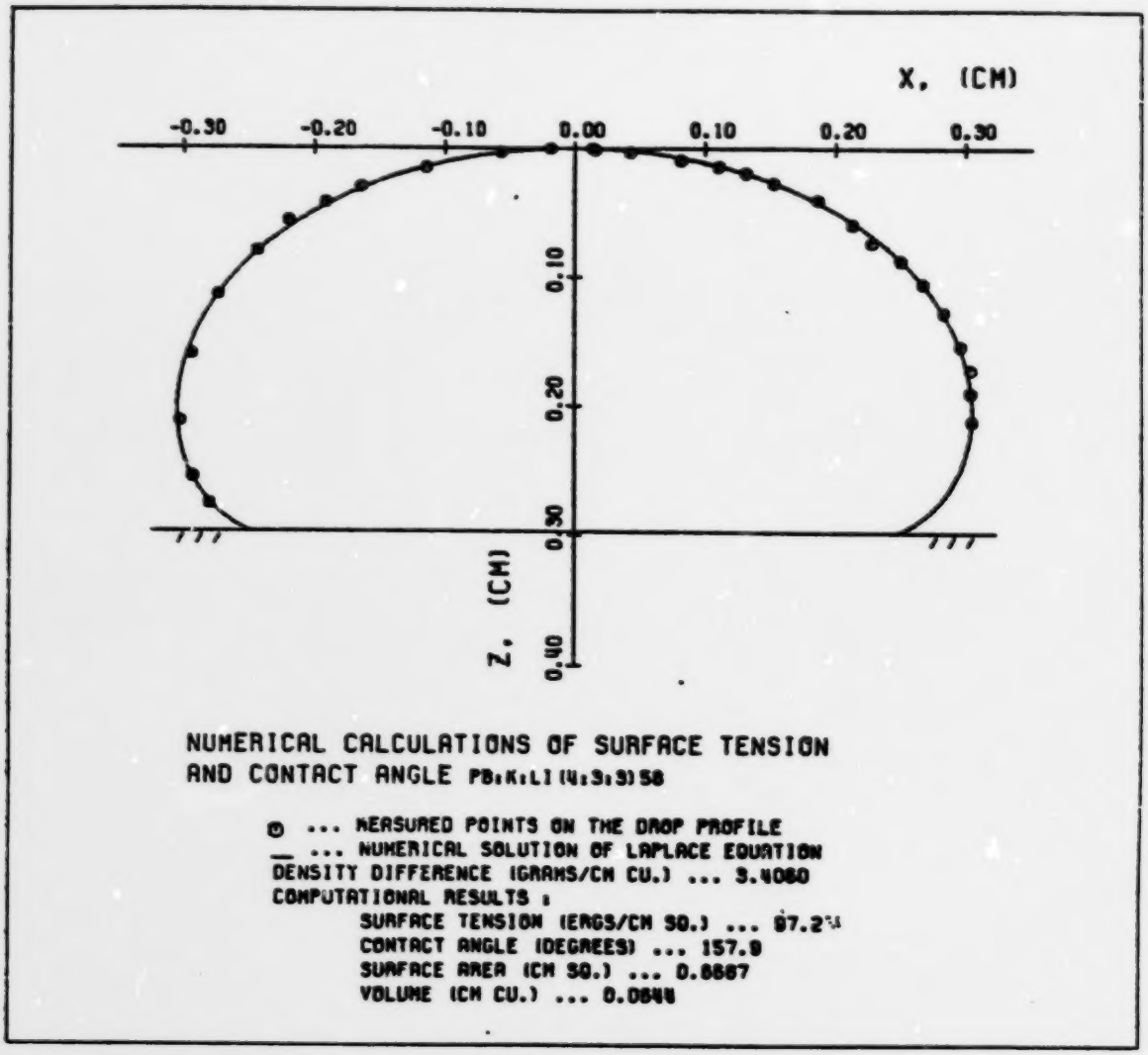

Figure 5.20. Surface tension of $PbCl_2$-KCl-LiCl(40:30:30 mol %) at 673 K.

Table 5.3. Surface tension of $PbCl_2$:KCl:NaCl(40:30:30 mol %) and $PbCl_2$:KCl:LiCl(40:30:30 mol %).

Salt composition; $PbCl_2$:KCl:NaCl(40:30:30 mol %)

Temperature = 793 K

Density = 3224 kg/m^3

Values obtained from a photograph taken 5 min. after melting.

Surface tension (mJ/m^2): 126, 125, 122, 115, 112, 106 and 105

Average value: 115.9 mJ/m^2

Standard deviation: 8.7 mJ/m^2

Values obtained from a photograph taken 18 min. after melting

Surface tension (mJ/m^2): 123, 120 and 115

Average value: 119.3 mJ/m^2

Standard deviation: 4.0 mJ/m^2

Average value from both photographs: 116.9 mJ/m^2

Total standard deviation: 7.5 mJ/m^2

Salt composition; $PbCl^2$:KCl:LiCl(40:30:30 mol %)

Temperature = 673 K

Density = 3406 kg/m^3

Values obtained from a photograph taken 6 min. after melting

Surface tension (mJ/m^2): 97.3, 96.6 and 94.6

Average value: 96.2 mJ/m^2

Standard deviation: 1.4 mJ/m^2

Figure 5.22 shows the numerical solution of the Laplace equation for two sets of measured coordinate points from the same photograph of a liquid containing 40 mol % $PbCl_2$. The surface tension values for the two solutions were 126 and 105 mJ/m^2, and the calculated contact angle values were 144° and 166° respectively.

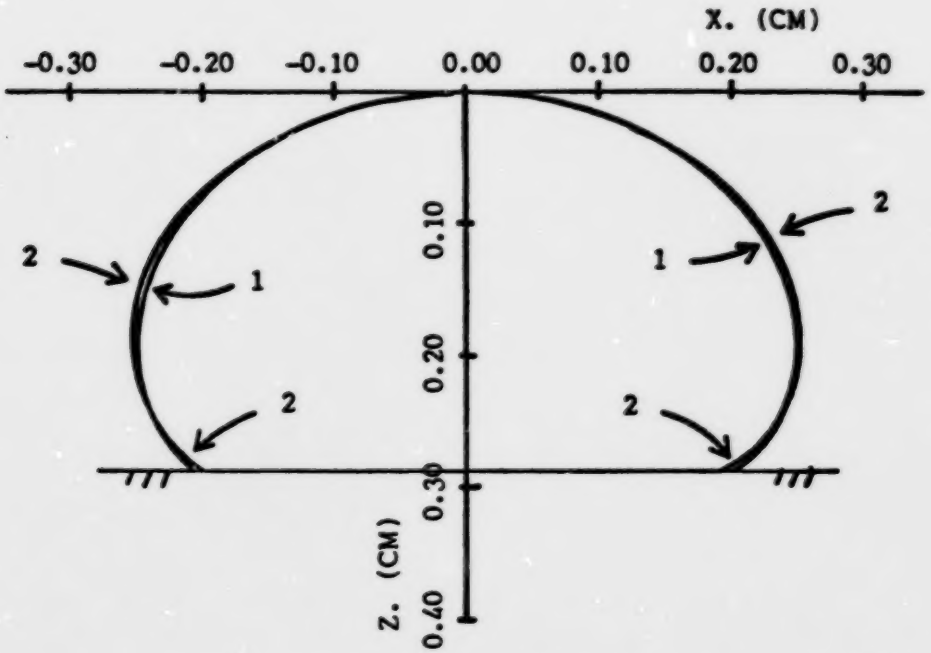

Figure 5.22. Numerical calculations of surface tension and contact angle for two set of coordinate points from the same photograph of a liquid drop of $PbCl_2$:KCl:NaCl(40:30:30 mol %). Temp. = 793 K

First solution (curve 1); Surf. tension = 126.3 mJ/m^2
Cont. angle = 144.3 degrees

Second solution (curve 2); Surf. tension = 105.8 mJ/m^2
Cont. angle = 165.7 degrees

CHAPTER 6

DISCUSSION

6.1 Contact Angle Measurements on Graphite

The results of the sessile drop experiments using graphite as the solid substrate are given in Table 5.1, and the contact angles for the different liquids are plotted versus time in Fig. 5.2-5.9. Shortly after the melting of the different salt mixture, the contact angle was in the range from 118° to 148° for all the systems. The contact angle decreased with time for most of the liquids and was most pronounced for pure $PbCl_2$.

The first and last measured contact angles for the different experiments are shown in Table 6.1 together with the experimental temperature and the given or estimated surface tension value of the corresponding liquids. A plot of the first and last measured contact angles versus temperature for all the liquids is shown in Fig. 6.1. The first measured value (shortly after melting) is termed the advancing contact angle. When the contact angle became constant after a certain time as seen for pure $PbCl_2$, the contact angle is termed the receding contact angle. The difference between the first measured contact angle (usually also the largest) and the last measured contact angle is termed contact angle hysteresis. This contact angle hysteresis is less than 20° for most of the liquids with the exception of pure $PbCl_2$, where the hysteresis is 60°.

As shown in Figure 6.1 there is a tendency for the contact angle to decrease with increasing temperature. However, from the experiments with different specific liquids, no general effect of the temperature

Table 6.1. The first and last measured contact angle formed by liquid $PbCl_2$-Alk.Chloride mixtures on graphite under an argon atmosphere.

Date	Composition (mol %) $PbCl_2$	KCl	NaCl	LiCl	Temp. (K)	Contact Angle (degrees) First meas.	Last meas.	Surf. Tension (mJ/m^2)
061082	100	0	0	0	823	122	70	131
061082	100	0	0	0	823	130	103	131
220982	100	0	0	0	823	138		131
					873		98	125
130882	100	0	0	0	800	134	80	134
191082	0	100	0	0	1073	135	135	96.3
130982	0	100	0	0	1073	132	103	96.3
051082	0	0	100	0	1093	118	115	113
151082	0	0	100	0	1093	142	133	113
021082	0	0	0	100	923	140	138	127
290982	40	60	0	0	783	148		113
					873		144	105
240982	40	60	0	0	823	138		109
					783		135	113
300982	40	0	60	0	923	135	116	117
081082	0	50	50	0	953	138	136	111
091082	0	50	0	50	793	140	140	123
051082	40	30	0	30	673	147	133	134
071082	40	30	30	0	793	135	130	122
041082	40	30	30	0	823	148	143	119

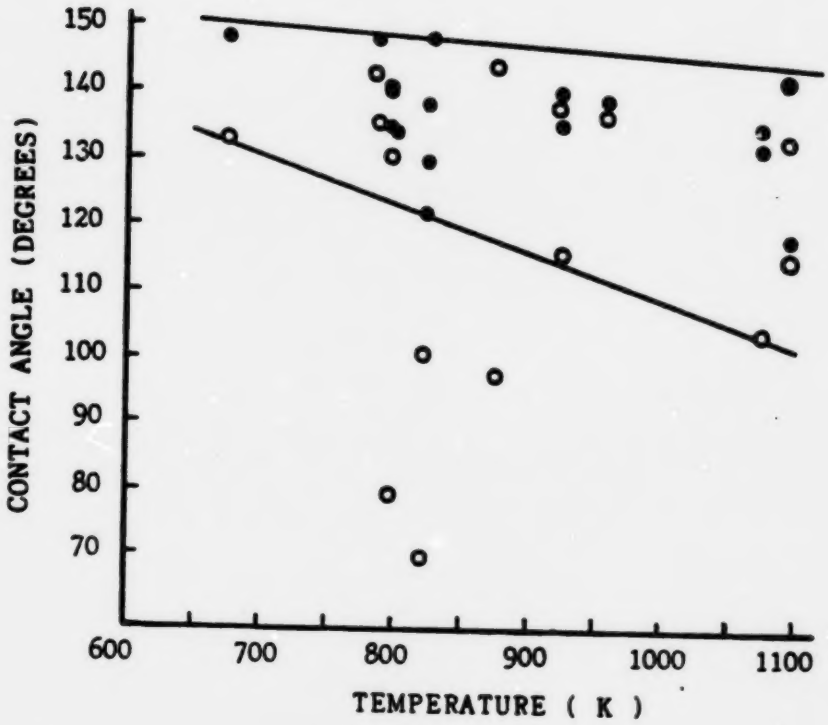

Figure 6.1. Variation of the contact angle with temperature for $PbCl_2$-Alk.Chloride mixtures on graphite under an argon atmosphere.

Case 1(●): Contact angle measured shortly after melting.

Case 2(○): Last measured contact angle in each particular experiment.

was observed in the temperature range studied for each liquid. The reproducibility of the measured contact angle for a given photograph is ±5°. A smaller change than 5° could therefore not be observed.

Due to the higher vapour pressure of pure $PbCl_2$, the evaporation loss of pure $PbCl_2$ is much more siginificant than for the other liquids (see Appendix EIGHT). This phenomena can explain in part the significant decrease in the contact angle with time for pure $PbCl_2$. As the amount of liquid decreases, the size and shape of the drop change and the contact angle decreases from one metastable state to another. For all the other liquids, no significnat loss of liquid occurred due to the lower vapour pressure (see Appendix EIGHT) and also due to the lower experimental temperature of the ternary and binary systems. The contact angle remained therefore more constant and only vibrations or changes in the temperature altered the contact angle to another metastable state. Even if the receding contact angle (the smallest possible equilibrium contact angle) for these liquids had approximately the same value as for pure $PbCl_2$(70° - 100°), it could not be observed in these experiments. To study the receding contact angle of these liquids, another experimental setup is necessary where the liquid is forced to recede.

Due to this hysteresis, these contact angles cannot be interpreted in terms of Young's contact angles. The use of these contact angles in Young's equation is not strictly correct. In these experiments where the contact angle hysteresis is at least 60° for pure $PbCl_2$ and unknown for the other liquids, the use of the measured contact angles in Young's equation cannot be justified.

Assuming that the hysteresis is due to roughness (porosity), the global equilibrium contact angle is given by Wenzel's equation (eq. 6.1),

but as previous mentioned several metastable states exist on both sides of Wenzel's contact angle (76). It can therefore be assumed that Wenzel's contact angle has a value somewhat smaller than the first recorded contact angle (below 130° - 140°). It can be seen from Wenzel's equation that if Wenzel's contact angle is larger than 90°, then Young's contact angle is also larger than 90° but smaller than Wenzel's contact angle. If Wenzel's contact angle is smaller than 90°, then Young's contact angle is also smaller than 90° but larger than Wenzel's contact angle. If we assume that Wenzel's contact angle is in the range from 80° to 130° then Young's contact angle must also be in the same or smaller range around 90°.

$$r \cos \theta_y = \cos \theta_w \tag{6.1}$$

$$r : \frac{\text{actual area}}{\text{geometric area}} \geq 1$$

θ_w: Wenzel's contact angle

θ_y: Young's contact angle

The first measured contact angle (the advancing contact angle) for different liquids is plotted versus the surface tension of the corresponding liquids in Fig. 6.2. The contact angle seems to be constant and independent of the value of the surface tension. However, the scatter in the contact angle values is too large and also the range of surface tension values is too small to propose any definite relation.

The reproducibility of the actual contact angle measurements from the sessile drop photographs was found to be ±5°, which also corresponds to the uncertainty limit. The same reproducibility (±5°) was found when the contact angle was measured from two different photographs of the same liquid drop, taken shortly after each other.

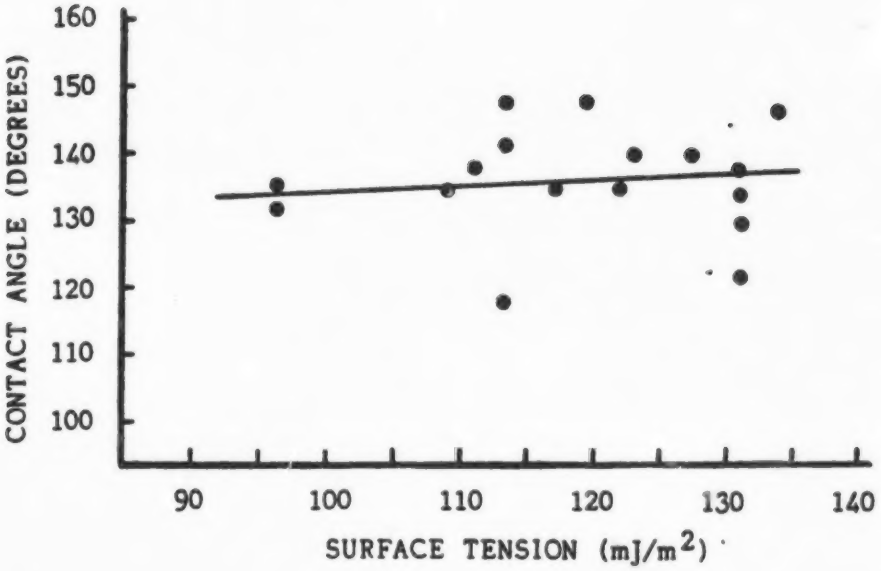

Figure 6.2. Contact angle versus surface tension for liquid $PbCl_2$-Alk.Chloride sessile drops on graphite under an argon atmosphere.

It can be seen from Table 5.1 that the difference between the contact angle on the left or right side of the drop was usually less than 5°, although in certain cases it was as large as 20° (Fig. 6.4). This drop asymmetry is assumed to be formed upon melting of the salt because of the surface roughness and inhomogeneity (93, 126, 127). The difference in the advancing contact angle for two sets of experiments with the same liquid can be explained in the same manner.

The reproducibility of the first recorded contact angle (the advancing contact angle) was found to improve by increasing the height to the base diameter ratio of the solid salt. When the solid had a large base diameter compared to the height, asymmetrical drops were obtained as shown in Figs. 6.3 and 6.4. Any intermediate contact angle between the advancing and receding angle could be formed during the melting.

6.2 Effect of Time on the Contact Angle

In all the experiments with pure $PbCl_2$ (Fig. 5.2), the contact angle decreased significantly with time. This is assumed to be due to the high vapour pressure and corresponding loss of $PbCl_2$ at these temperatures. It is therefore interesting to see if there exists a correlation between the vapour pressure and the decrease in contact angle with time for the different liquids. The vapour pressure of binary mixtures of $PbCl_2$-Alk. Chloride decreases with increasing size of the cation (7). Mixtures of $PbCl_2$-LiCl have therefore higher vapour pressure than mixtures of $PbCl_2$-NaCl (or KCl) at the same temperature. The same trend exists also for ternary systems where additions of KCl decreases the vapour pressure more than the corresponding additions of NaCl and LiCl.

Figure 6.3. Sessile drop on graphite under argon atmosphere.

Salt composition; $PbCl_2$-KCl(40:60 mol %)
Graphite support, density = 1870 kg/m^3.
Temp. = 823 K. Magnification: 16

Figure 6.4. Sessile drop on BN under argon atmosphere.

Salt composition; KCl:NaCl(50:50 mol %)
Solid support, BN
Temp. = 953 K. Magnification: 16

6.2.1 $PbCl_2$-KCl and $PbCl_2$-NaCl Binary Systems

As seen in Fig. 5.6, the contact angle for the $PbCl_2$-KCl (40:60 mol %) mixture hardly decreased with time. The experimental temperature was in the range from 783 to 873 K and the $PbCl_2$ vapour pressure is in the range from 22 to 224 Pa (128). For the corresponding mixture of $PbCl_2$-NaCl the contact angle decreased from about 135° to 114° (Fig. 5.7). The temperature was 923 K with a vapour pressure of $PbCl_2$ equal to 573 Pa (128). The much larger decrease in the contact angle for the $PbCl_2$-NaCl binary mixture can be correlated to both the higher experimental temperature and also to the higher vapour pressure of $PbCl_2$ above the $PbCl_2$-NaCl mixture. The same increase in wettability on graphite going from KCl to NaCl was also found by Yamamoto and Fujisawa (129) in their experiments with $PbCl_2$-Alk. Chlorides in graphite crucibles. Yamamoto used shallow graphite crucibles in his measurements of the $PbCl_2$ vapour pressure above different binary and ternary systems and he found that $PbCl_2$-KCl (60:40 mol %) mixtures did not wet the crucibles while the $PbCl_2$-NaCl (60:40 mol %) salt mixtures sticked readily to the graphite walls and were difficult to remove.

6.2.2 $PbCl_2$-KCl-Nacl and $PbCl_2$-KCl-LiCl Mixtures

A slight but not a significant decrease in the contact angle was observed for both of the two ternary systems (Figs. 5.8 and 5.9). The experimental temperature for the $PbCl_2$-KCl-NaCl (40:30:30 mol %) ternary system was in the range from 793 K to 873 K and the vapour pressure of $PbCl_2$ varied between approximately 6 Pa to 92 Pa (3). The decrease in the contact angle was more prounounced (from 147° to 133°) for the

$PbCl_2$-KCl-LiCl(40:30:30 mol %) ternary mixture, even though the operating temperature was lower (from 673 to 723 K) and the vapour pressure of $PbCl_2$ was in the range from 0.3 Pa to 2.2 Pa (3) (see Appendix EIGHT). At equal temperatures, the vapour pressure of $PbCl_2$ would have been highest for the ternary containing LiCl and the largest decrease in the contact angle would have been expected to occur for this system. As discussed later, the surface tension of the $PbCl_2$-KCl-LiCl was found to be lower (96 mJ/m^2) than the values found by estimation (linear extrapolation) from the binary systems (134 mJ/m^2), while the surface tension of the ternary containing NaCl was found to be close to the estimated value. This lowering of the surface tension is most probably due to contamination of the liquid and it probably also affects the solid-liquid interfacial tension which together could cause the contact angle to decrease.

6.3 Surface Tension of Graphite

Table 6.2 shows some measured or calculated values of the surface free energy of graphite with values ranging from 130 to 230 mJ/m^2, which are much lower than the values for most solid metals and oxides. The surface tension of Al_2O_3 is about 900 mJ/m^2 and the value of SiO_2 is about 593 mJ/m^2 as shown in Table 6.3.

Table 6.2. Some values of surface free energy of graphite.

Surface free energy (mJ/m^2)	Ref.	Method used
230	99	Wetting of graphite by Al-Mg alloys
225	130	Heat of immersion of graphite in benzene
165	131	From energy of adhesion across the basal plane of graphite
130	132	Wetting data

If the following inequality described by Bondi (133)

$$\gamma_{LV} < \gamma_{SV} \qquad (6.2)$$

is considered a necessary condition for complete spreading of the liquid on the solid substrate, it should be possible for these salt mixtures to wet graphite. The surface tension of the chloride mixtures is in the range from about 95 to 130 mJ/m^2. The observed contact angles were, however, in the range from about 100° to 145°, and the contact angle was smaller than 90° only for pure $PbCl_2$, after a certain time. These high angles indicate that the above condition may be necessary but is not sufficient. Another possibility is that the surface tension of graphite is even lower than the lowest value (130 mJ/m^2) given in Table 6.3. Neumann et al (98) developed an equation-of-state for low energy solids. Their equation are based on experimental data for liquids with low surface tension (less than 72.8 mJ/m^2) and these equations can not be used for liquids with higher surface tension. The high values of the contact angle on graphite compared to Al_2O_3 and SiO_2 confirm that the solid surface tension of graphite is lower than that of these oxides but an exact value cannot be given from these experiments.

6.4 Contact Angle on Al_2O_3, SiO_2, ZrO_2, BN and Inconel

The polycrystalline Al_2O_3 plaques used in this study were all completely wetted by all the liquids ($PbCl_2$, KCl, NaCl and LiCl) used in this study. The average grain size was about 7 μm but the corresponding roughness did not seem to affect the wetting of these plaques.

The SiO_2 plates were all wetted by the pure salts and also by a

$PbCl_2$-KCl-LiCl(40:30:30 mol %) ternary mixture, with the exception of one single experiment where the contact angle was as high as 124° before the liquid suddenly collapsed. This large unstable contact angle could have been caused by contamination of the solid surface or by the existence of several metastable equilibrium values. If several metastable states exist, the activation energy required to go from one equilibrium position to another must be small because the SiO_2 plates were wetted in all the other experiments.

The inconel plaques were completely wetted by all the alkali chlorides, and it was also difficult to remove the salt from the solid after the experiments. Due to the high solid-vapour surface tension of most metals (134), a complete wetting is expected for all molten salts. If the metal surface is oxidized, non-wetting might occur due to the lower surface tension of the solid oxide.

The contact angle varied from 105° to 60° for the different liquids on boron nitride. Due to the porosity of the BN solid, asymmetrical drops were formed as shown in Fig. 6.4, and the roughness makes it impossible to estimate any equilibrium contact angle for the different liquids.

The ZrO_2 plaques were the least wetted of the oxides. For pure $PbCl_2$ on ZrO_2, the contact angle decreased from 92° to 68° after 180 minutes of the experiment. This slow decrease in the contact angle was expected due to the surface roughness, and the obtained contact angles are expected to be more a function of the surface roughness than of the solid-vapour surface tension of the ZrO_2. In these experiments with solid oxides, the Al_2O_3 plaques were the most readily wetted which also apriori is expected due to its higher solid-vapour surface tension (Table 6.3).

Table 6.3. Some typical values of surface free energy at room temperature (after C.B. Alcock (134)).

Substance	Surface energy (mJ/m^2)
Fe	1900
Cu	1600
Sn	1200
Ag	1100
Zn	105
MgO	1100
Al_2O_3	900
ZrO_2	797*
SiO_2	593**

*Value given by Livey and Murray (30) at 0 K.

**Value estimated by Harding and Rossington (135) at 25°C.

6.5 Surface Tension

The surface tension was measured for the two ternary systems: $PbCl_2$-KCl-NaCl(40:30:30 mol %) and $PbCl_2$-KCl-LiCl(40:30:30 mol %). Due to the diffuse outline of the drop profile of salt mixtures with no $PbCl_2$ content (Fig. 5.10), no surface tension measurements were carried out for these mixtures. The use of the X-ray radiographic technique to study surface tension from sessile drops, was found to be not suitable for liquids with low density and low X-ray absorptivity. For salts containing 40 mol % $PbCl_2$, at least an indication of the value of the surface tension can be obtained. For the $PbCl_2$-KCl-NaCl mixture, the obtained values varied from 105 to 126 mJ/m^2 with an average value of 117 mJ/m^2. The calculated Laplace curves from these two extreme

sets of coordinate points are shown in Figure 5.22. As can be seen from the two very similar curves, the surface tension is very sensitive to the curve shape. The maximum diameter and the height of these two curves are almost identical and the use of these to calculate the surface tension as used in Dorsey's method (63) and in the method by Ashfort and Adams (64) is not recommended.

[illegible] points, the reproducibility of the measurements increases. This does not necessarily mean, however, that the obtained values are closer to the true value. Another problem is the possibility of personal manipulation during digitizing of the coordinate points. Even by recording coordinate points from within the diffuse part of the drop outline, the surface tension can be changed by ±10% depending on the manner in which the coordinate points are recorded.

Even with these difficulties, the surface tension of the $PbCl_2$-KCl-NaCl(40:30:30 mol %) was found to be close to the value estimated from the binary systems. The average value at 793K was found to be 117 mJ/m^2 with a standard deviation of 7.5 mJ/m^2. For the $PbCl_2$-KCl-LiCl (40:30:30 mol %) the obtained value was 96.2 mJ/m^2 at 673 K which is much lower than the estimated value of 134 mJ/m^2. The error limit in both these measurements is ±10 %. LiCl is very hygroscopic and this low surface tension value indicates that the salt mixture has not been sufficiently purified or that the surface became contaminated during the experiment.

6.6 Error Sources due to Image Recording and Analysis

Given a photograph of a sessile drop, several different factors are important is calculating the surface tension. Due to the magnification of the drop, a reference subject with known dimensions must be used to calculate the real size of the drop. In these experiments a 1/4 inch steel ball was used, and separate photographs of this steel ball was used to calibrate the magnification. A better system would have been to record the image of the reference ball and the sessile drop on the same photograph. This will prevent any possibility of change in relative magnification during image processing and analysis.

To record the coordinate points of the drop profile, a reference coordinate system was used. It was assumed that the solid support was in a horizontal position. The recorded axis system need not necessarily be perfectly correct and the calculated surface tension will deviate from the correct value. In the computer program where the surface tension is calculated, the error function which is defined as the sum of the squares of the shortest distance between the measured points and the Laplace curve, is minimized. It is therefore possible to rotate the axis of the system by an angle θ and recalculate both the surface tension and the error function until a minimum in the error function occurs. At this point the recorded drop profile is most similar to the calculated Laplace curve which describes the drop profile. Thus this calculated surface tension can be assumed to be the best value.

The last main error source in the image recording process is due to the X-ray penetration of the edges of the sessile drop. This leads to a diffuse edge around the drop outline as described in Appendix ONE. Figure 5.22 shows two solutions of the surface tension calculated from

the same photograph. Due to the diffuse image, values between 105 and 126 mJ/m^2 were obtained. To improve this, lower X-ray voltage must be used. By reducing the thickness of the construction materials, the voltage limit has been reduced to about 45-50 kV. However, an even lower limit would be preferable.

CHAPTER 7

CONCLUSIONS

1) An apparatus based on an X-ray radiographic technique has been constructed. The image of the system under study could be recorded on an X-ray film or displayed on a TV screen. The use of the TV system was very useful in determining the correct position for the sessile drop before any X-ray photograph was taken. This system can also be used to study dynamic effects such as bubble formation during the electrolysis of fused salt.

2) A discussion of the theory and the different equations commonly used in studies of surface tensions and contact angles, has been given. Data have been collected in an attempt to find an empirical relation between the surface tension of the liquid and the contact angle it forms on specific solids. Due to the non-ideality of most solid surfaces such a relation could not be obtained, and the thermodynamic status of a measured contact angle on such surfaces is not clear. However, it can be concluded that as a trend, the liquid with the highest surface tension will wet a specific solid surface least.

3) The contact angles of different mixtures of $PbCl_2$, KCl, NaCl and LiCl on different solid materials have been measured. The oxides used in this study (Al_2O_3, SiO_2 and ZrO_2) were all wetted by these mixtures. The contact angle was largest on the ZrO_2 plaques, which is partly due to the roughness of these plaques and partly due to the lower solid surface tension of ZrO_2 compared to that of Al_2O_3 and SiO_2. Inconel was completely wetted by these liquid mixtures with contact

angles less than 25°. The contact angles varied between 105° and 60° on BN. The BN plaques used in this study had a high porosity and asymmetrical drops were formed. No physical interpretation of the contact angle could therefore be given.

4) The largest part of the experiments were carried out with graphite plaques. Symmetrical drops were obtained in most cases. The contact angle was between 118° and 148° shortly after melting of the salt mixtures for all systems studied. The contact angles decreased slightly with time for most of the systems. With liquids of pure $PbCl_2$, the contact angle decreased rapidly with time and then approached a constant value. This decrease in contact angle for pure $PbCl_2$ was explained by the loss of $PbCl_2$ due to vaporization. Pure $PbCl_2$ has a much higher vapour pressure than the other mixtures used in this study. The first measured contact angle for these mixtures on graphite was interpreted as the advancing contact angle. This angle is the highest metastable equilibrium contact angle, which develops due to the roughness (porosity) of the surface.
A slight decrease in contact angle with increasing temperature was observed when all the liquid mixtures were considered as a whole, independent of the surface tension. For each particular experiment no temperature dependency was observed in the temperature range studied.

5) The surface tension was measured for two ternary mixtures. A numerical solution method was used and found to give more reproducible and accurate values than methods based on measurements of specific properties such as height and diameter of the drop. The error limit in these experiments is ±10%, which is mainly due to the diffuse outline

of the drop image.

6) For liquids with higher absorptivity of X-rays and also with higher density, it is expected that the error limit due to the diffuse outline of the drop will be lower than with liquids used in this study. The X-ray radiographic technique is therefore assumed to be suitable for studying interfacial tension between metals and salts or between metals and slags, while other methods are recommended in studies of surface tension of any liquid-gas systems.

Appendix ONE. Radiation intensity across a spherical drop.

Intensity: $I = I_o \cdot \exp(-\mu\rho 2(R^2-x^2)^{\frac{1}{2}})$, for $x < R$

Where : ρ = density of liquid

: μ = X-ray absorbtivity coefficient

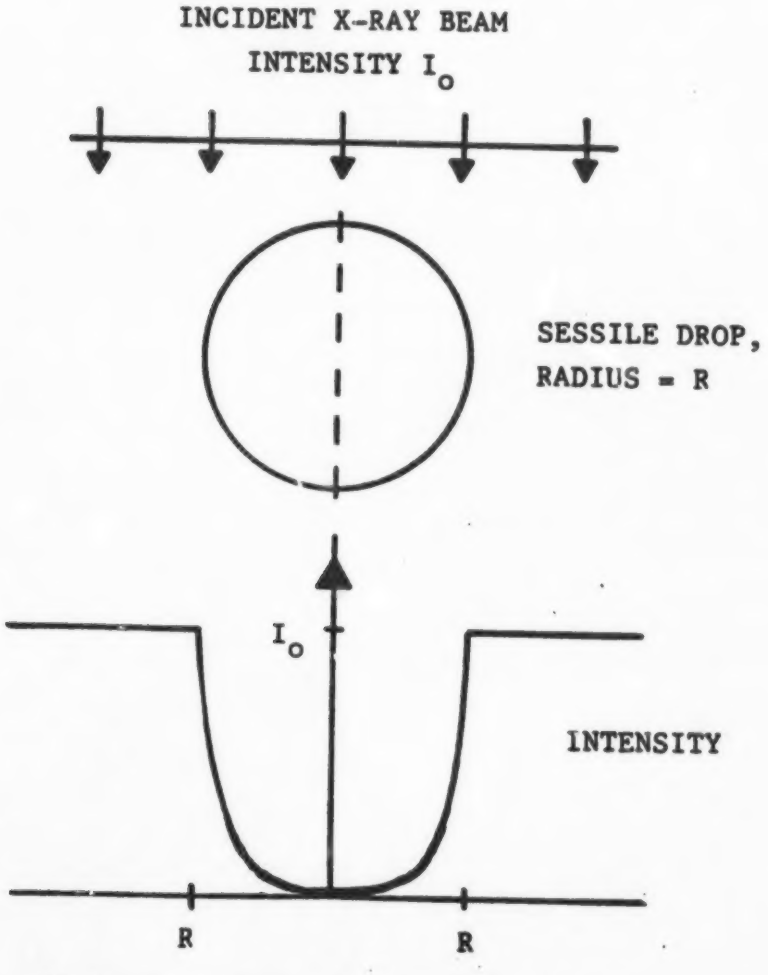

Appendix TWO. Effect on focal spot on the intensity distribution.

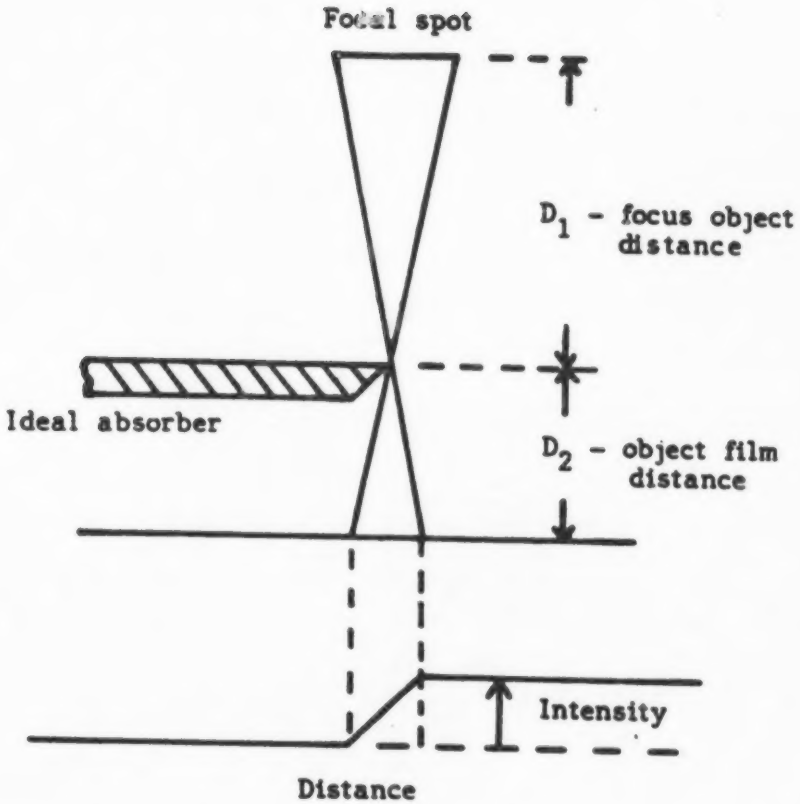

Appendix THREE. Specifications for the X-ray anode.

The X-ray anode is an oil cooled anode (PX-2A) from Picker X-ray.

Anode: 1 piece hollow cast copper with tungsten target imbedded.
Oil cooled. Effective size of focal spot - 3.8 mm.

Cathode: Line focus with tungsten filament.

Target: angle 45°

Insert tube: Part No. T40-7, Focal spot B-3.8

Maximum voltage - 100 kV

Maximum current - 10 mA

On these old X-ray anodes the focal spot may be as large as 5.0 mm instead of 3.8 mm as specified.

Appendix FOUR. Surface characteristics of two different graphite disks and of a polycrystalline alumina (Al_2O_3) disk.

Graphite, density = 1870 kg/m^3

Minimum pore size	=	0.43 μm
Maximum pore size	=	2.93 μm
Average pore size	=	1.77 μm
Standard deviation	=	0.99 μm
Area fraction	=	0.15

Graphite, density = 1650 kg/m^3

Minimum pore size	=	2.61 μm
Maximum pore size	=	50.6 μm
Average pore size	=	14.3 μm
Standard deviation	=	11.8 μm

Polycrystalline alumina

Minimum grain size	=	1.30 μm
Maximum grain size	=	25.2 μm
Average grain size	=	7.15 μm
Standard deviation	=	5.92 μm

Appendix FIVE. Stated purity and analysis of chemicals.

Lithium Chloride (LiCl), produced by CERAC

Grade; 99.8% pure, high-purity

Main cation impurity; Na less than 0.1%

Lead Chloride ($PbCl_2$), produced by J.T. Baker Chemical Co.

Grade; reagent grade, 100.0%

Insoluble matter 0.003%, Nitrate(0.003%), Sulphate(0.005%),

Copper(0.0001%), Iron(0.0005%)

Potassium Chloride(KCl), produced by J.T. Baker Chemical Co.

Grade; reagent grade, assay 100.1%

Insoluble matter 0.002, Iodide (0.002%), Bromide (0.01%),

Chlorate and Nitrate (0.003%), Nitrogen compounds (0.001%),

Sulphate (0.0006%), Barium (0.001%), Calsium and Magnisium (0,002%),

Sodium (0.006%)

Sodium Chloride (NaCl), produced by J.T. Baker Chemical Co.

Grade; reagent grade, assay 99.5%

Insoluble matter 0.003%, Iodide (0.002%), Bromide (0.005),

Chlorate and Nitrate (0.001%), Sulphate (0.002%), Barium (0.001%)

Calsium and Magnisium (0.003%), potassium (0.0025%)

Appendix SIX. Ternary phase diagram of $PbCl_2$-KCl-LiCl and $PbCl_2$-KCl-NaCl (3).

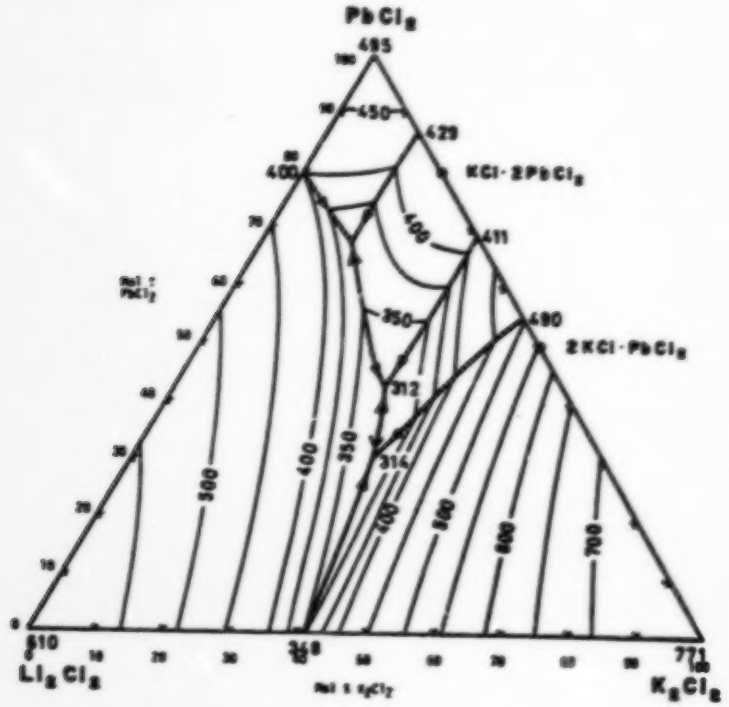

Calculated ternary phase diagram of LiCl-KCl-$PbCl_2$

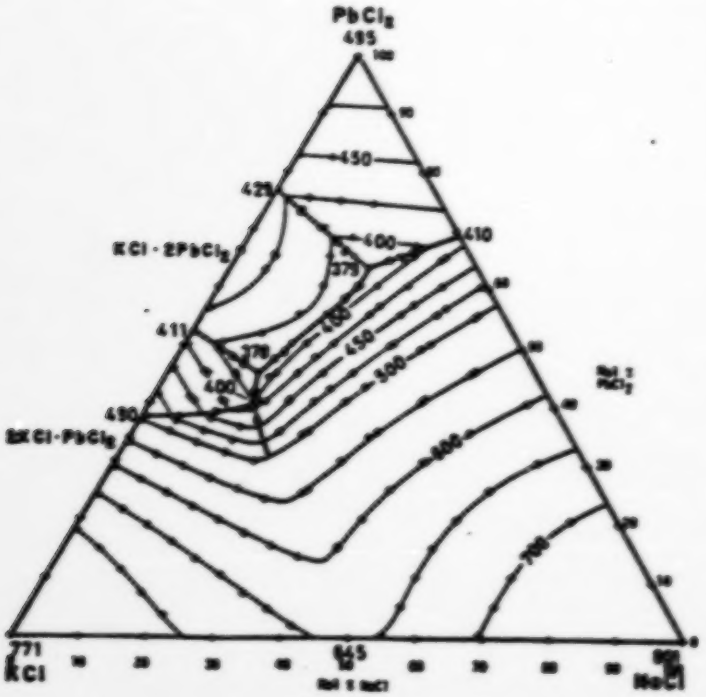

Calculated ternary phase diagram of $PbCl_2$-KCl-NaCl

Appendix SEVEN. Density of two ternary mixtures (136).

Composition: 40% mol $PbCl_2$, 30% mol KCl, 30% LiCl

Density (kg/m^3)	Temp.(K)
331.6	777
325.2	802
318.5	887
314.3	929
303.8	1053

Density (kg/m^3): $\rho = 406.6 - 0.98 \cdot T$

Composition: 40% mol $PbCl_2$, 30% mol KCl, 30% mol NaCl

Density (kg/m^3)	Temp. (K)
315.7	855
311.3	898
309.8	943
304.0	976
299.9	1020

Density (kg/m^3): $\rho = 396.9 - 0.94 \cdot T$

Appendix EIGHT. Vapour pressure of pure and mixed chlorides.

Vapour pressure of pure chlorides (Pa)

T(K)	$PbCl_2$	KCl	NaCl	LiCl
700	11			
800	84			
900	940		4.0	3.9
1000	6000	16	7.0	41
1100	26000	102	68	265

Vapour pressure of $PbCl_2$ for mixed chlorides (Pa)

T(K)	$PbCl_2$:KCl(40:60 mol %)
783	22
873	224

T(K)	$PbCl_2$:NaCl(40:60 mol %)
923 K	573

T(K)	$PbCl_2$:KCl:NaCl(40:30:30 mol %)
793	≈ 6
873	92

T(K)	$PbCl_2$:KCl:LiCl(40:30:30 mol %)
673	0.32
723	2.2

Appendix NINE. Effect of the gas atmosphere on the wetting of graphite.

The contact angle formed on graphite for a liquid mixture of $PbCl_2$:KCl:NaCl(40:30:30 mole %) under an argon atmosphere was around 140° at 793 K. The gas atmosphere was changed from pure argon to a 1/1 mixture of argon and chlorine gas, but no change in the contact angle was observed. However, when the argon gas was replaced with air or dried air, the contact angle decreased rapidly as shown in Fig. A9. This effect was observed both on graphite with a density of 1870 kg/m^3 and on amorphous carbon.

Due to the oxidation of the graphite substrate, fine graphite powder was formed on the surface. To test if this powder could cause the fast wetting, an experiment with a preoxidized graphite substrate was carried out. The salt mixture formed a contact angle of 45° instead of the normal $130-140^{\circ}$ under an argon atmosphere. After the experiment, graphite powder was partially covering the edge of the sessile drop, while the rest of the surface was completely white with no sign of oxide formation. With experiment where air was introduced, a red-brownish material was found to cover the surface of the sessile drop. This substance was identified as PbO by means of x-ray diffraction.

The effect of air was also studied with the above salt composition on substrates of BN. In one experiment where a symmetrical drop forming a contact angle of about 130° on the BN under argon atmosphere, the introduction of dry air lead to only a slight decrease in the contact angle of about 15°.

It is therefore concluded that air will lead to wetting of graphite by liquid mixtures of $PbCl_2$, KCl and NaCl. The reason may partly be due to oxidation of the graphite surface and partly be due to the formation of PbO.

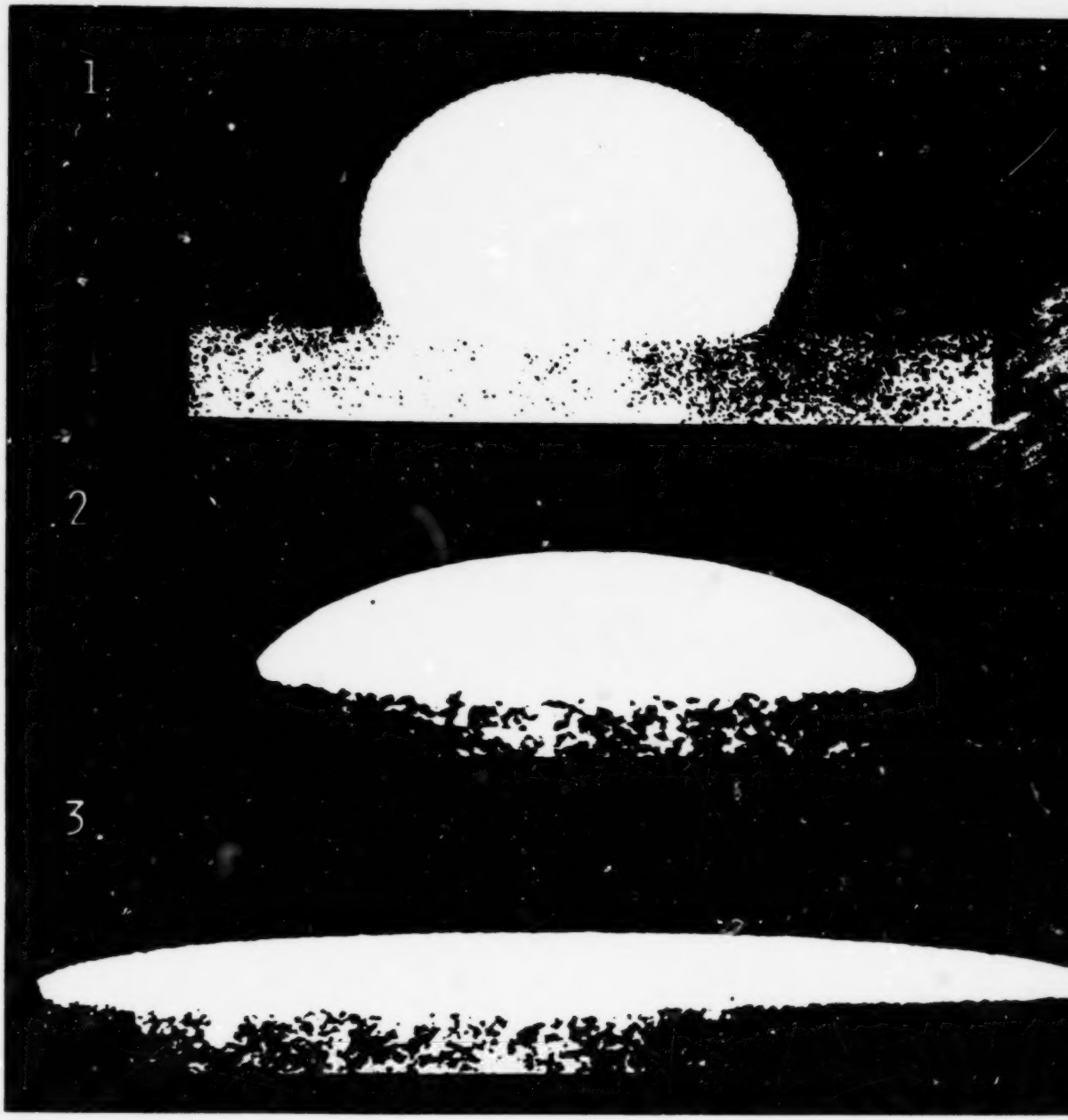

Figure A9. Sessile drop of $PbCl_2$:KCl:NaCl (40:30:30 mole %) on graphite at 793 K.

1) Argon atmosphere
2) 1 min. after dry air was introduced
3) 5 min. after dry air was introduced

REFERENCES

1. M.M. Wong and F.P. Hauer. Symposium on Molten Salt Electrolysis in Metal Production. Editor: I.M.M. (1977).

2. F.P. Hauer, C.H. Elges and M.M. Wong. Report of Investigations 8166, U.S. Bureau of Mines (1976).

3. J.M. Skeaff, C.W. Bale, A.D. Pelton and W.T. Thompson, "Selection of ternary fused chlorides for the electrowinning of lead and zinc based on calculation of thermodynamic properties", CANMET Report 79-23 (1979).

4. G.A. Abramov and V.S. Zernyakov. J. Appl. Chem. USSR, 23, 1123 (1950).

5. J.J. Egan. J. Phys. Chem., 65, 2222 (1961).

6. I. Barin, O. Knacke and O. Kubaschewski. Thermochemical properties of Inorganic Substances. Springer-Verlag, New York, 1973 and Supplement (1977).

7. H. Bloom. The Chemistry of Molten Salts. Editor: W.A. Benjamin, Inc. (1967).

8. S.N. Flengas and N.R. Carmichael. J. Electrochem. Soc., 126, 2104 (1979).

9. B.F. Markov, I.K. Delimarskii and I.D. Pachenko. J. Polymer Science, 31, 263 (1958).

10. H. Bloom, F.G. Davis and D.W. James. Trans. Farady Soc., 56, 1179 (1960).

11. J.L. Dahl and F.R. Duke. J. Phys. Chem., 62, 1498 (1958).

12. G.J. Janz, R.P.T. Tomkins, C.B. Allen, J.R. Downey Jr., G.L. Gardner, U. Krebs and S.K. Singer. J. Phys. Chem. Ref. Data, 4, 871-1178 (1975).

13. R.B. Ellis and A.C. Freeman. J. Phys. Chem., 69, 1443 (1956).

14. K. Grjotheim, J.L. Holm, B. Lillebuen and H.A. Øye. Acta Chem. Scand., 26, 2050 (1972).

15. G. Bertozzi. J. Phys. Chem., 69, 2606 (1965).

16. I.D. Sokolova and N.K. Voskresen-Skaya. Russ. J. Phys. Chem., 36, 502 (1962).

17. D.A. Nissen and R.W. Carlsten. J. Electrochem. Soc., 121, 500 (1974).

18. R.B. Ellis. Prog. Rep. USAEC Contract No. AT-(40-1)-2073 (1961).

19. O.G. Desyatnikov. Zhur. Priklack. Klum., 29, 870 (1956).

20. Kh. L. Strelets, "Electrolytic production of magnisium", Keter Publishing House Jerusalem Ltd. (1977).

21. S.N. Flengas and P. Pint. Can. Met. Quart., 8, 151 (1969).

22. A.S. Russell. Met. Trans. 13, 12B, 203 (1981).

23. F.D. Richardson. Can. Met. Quart., 21, 111 (1982).

24. E.T. Turkdogan. Physical Chemistry of High Temperature Technology, Academic Press (1980), pp. 168-171.

25. R. Minto and W.G. Davenport. Trans. Inst. Min. Metall., 81, C36 (1972).

26. C.F. Cooper and J.A. Kitchener. J. Iron Steel Inst., 193, 48 (1959).

27. G.R. Belton. Can. Met. Quart., 21, 137 (1982).

28. J. Berg. Can. Met. Quart., 21, 121 (1982).

29. F.D. Richardson, Physical Chemistry of Melts in Metallurgy, Academic Press (1974), pp. 452-455, Volume 2.

30. D.T. Livey and Murray, "The wetting properties of solid oxides and carbides by liquid metals", Plansee Proc., 2nd Seminar, Reuttle-Tyrol (1955), p. 375 (published 1956).

31. S.K. Rhee. J. Amer. Ceramic. Soc., 53, 386 (1970).

32. D.R. Rossington and F.L. Harding. Rev. High Temp. Mater., 1, 9 (1971).

33. J.A. Champion, B.J. Keene and J.M. Sillwood. J. Materials Sci., 4, 39 (1969).

34. Yu. P. Nesterov, S.F. Vazhenin and L.N. Antipin. "Surface Phenomena in Metallurgical Processes", Editor: A.I. Belyaev, Consultants Bureau, New York (1965), pp. 114-119.

35. A.I. Belyaev, ibid., p. 3 (1965).

36. V.N. Eremenko and V.I. Nizhenko, ibid., pp. 28-45.

37. L. Rayleigh. Proc. Roc. Soc. (London), 92A, 184 (1915).

38. S. Levine, J. Lowndes, E.J. Watson and G. Neale. J. Colloid Interface Sci., 73, 136 (1980).

39. Z. Moser, M. Kucharski and K. Rzyman. J. Electrochem. Soc., 125, 692 (1978).

40. K. Grjotheim, T. Naterstad and H.A. Øye. Acta Chem. Scand., 30, 429 (1976).

41. G. Bertozzi and G. Soldani. J. Phys. Chem., 72, 353 (1968).

42. G. Bertozzi and G. Soldani, ibid, 70, 1838 (1966).

43. P. Kozakevitch and G. Urbain. J. Iron Steel Inst., 186, 167 (1957).

44. B. Gallois and C.H.P. Lupis. Met. Trans. B., 12B, 549 (1981).

45. J.F. Elliott and M. Mounier, "Surface and Interfacial Tensions in Copper Matte-Slag Systems, 1200°C", CIM, Hamilton Aug. (1981).

46. D.H. Bradhurst and A.S. Buchanan. J. Phys. Chem., 63, 1486 (1959).

47. A. Kasama, A. McLean and W.A. Miller. Can. Met. Quart., 19, 399 (1981).

48. H. Soda, A. McLean and W.A. Miller. Trans. JIM, 18, 445 (1977).

49. W.D. Harkins and F.E. Brown. J. Amer. Chemc. Soc., 41, 499 (1919).

50. T. El Gammal and R.-D. Mullenberg. Arch. Eisenhuttenw., 6, 51 (1980).

51. C.E. Stauffer. J. Phys. Chem., 69, 1933 (1965).

52. R.-J. Roe, V.L. Bacchetta and P.M.G. Wong, ibid, 71, 4190 (1967).

53. A.W. Neumann and R.J. Good. Surface and Colloid Science, Editors: R.J. Good and R.S. Stromberg, Plenum Press, New York (1979), pp. 31-88, Volume 2.

54. B.C. Allena and W.D. Kingery. Trans. Met. Soc. AIME, 215, 30 (1959).

55. K. Ogino, A. Nishiwaki and S. Hara. Osaka Yakinkai Kaishi, 13, 110.

56. G. Jurchison, B.A.Sc. Thesis, University of Toronto, Canada (1973).

57. V.N. Eremenko. The Role of Surface Phenomena in Metallurgy, Editor: V.N. Eremenko, Consultants Bureau, New York (1963), pp. 41-45.

58. B.C. Allen. Trans. Met. Soc. AIME, 227, 1175 (1963).

59. J.W. Gibbs, "The Scientific Papers", Dover, New York, 1961, pp. 55-371, Volume 1.

60. A.W. Adamson, "Physical Chemistry of Surfaces", 2nd edition, Interscience Publisher (1967), pp. 9,10.

61. Y. Rotenberg, L. Boruvka and A.W. Neumann. J. Colloid Interface Sci., in press.

62. P. Nikolopoulos and G. Ondracek. Z. Werkstofftech., 13, 60 (1982).

63. N.E. Dorsey. J. Wash. Acad. Sci., 18, 505 (1928).

64. F. Bashforth and J.C. Adams. "An attempt to test the theory of capillary action", Cambridge University Press and Deighton Bell and Co., Cambridge (1892).

65. J.F. Padday. J. Colloid Interface Sci., 48, 170 (1974).

66. R.S. Burdon, "Surface tension and the spreading of liquids", Cambridge University Press (1949), p. 15.

67. C. Maze and G. Burnet. Surface Sci., 13, 451 (1969).

68. C. Maze and G. Burnet, ibid, 24, 335 (1971).

69. F. Neumann. Varlesung uber die theorie der capillaritat. B.G. Teubner, Leipzig (1893).

70. J.J. Bikerman. Suface Chemistry (2nd edition), Academic Press, New York (1958), p. 343.

71. C.R. Manning Jr. and T.B. Gurganus. J. Amer. Ceramic Soc., 52, 115 (1969).

72. R.J. Good and M.N. Koo. J. Colloid Interface Sci., 71, 283 (1979).

73. L. Buruvka and A.W. Neumann, ibid, 65, 315 (1978).

74. A.W. Neumann. Z. Physik. Chem. N.F., 41, 339 (1964).

75. D.D. Jordon and J.E. Lane. Aus. J. Chem., 17, 7 (1964).

76. A.W. Neumann. Advances in Colloid and Interface Science, 4, pp. 105-191 (1974).

77. A.W. Neumann and W. Tanner. J. Colloid Interface Sci., 34, 1 (1970).

78. B. Gallois and C.H.P. Lupis. Metall. Trans., 2, 555 (1971).

79. David Jenkis, "Radiographic Photography and Image Processes", MTP Press Ltd., Lancaster, England (1980).

80. R.L. Durant. Brit. J. Nondestruct. Test., 12, 125 (1970).

81. Miroslav Macecek, Ph.D. Thesis, University of Toronto (1976).

82. I.T. Gul'din and Buzhinskaya. Surface Phenomena in Metallurgical Processes. Editor: A.I. Belyaev, Consultants Bureau, New York (1965), pp. 177-178.

83. Yu. V. Naidich and G.A. Kolesnichenko, ibid, pp. 218-223.

84. L. Boruvka and A.W. Neumann. J. Chem. Phys., 60, 5464 (1977).

85. K. Grjotheim, T. Østvold and H.A. Øye. "Applied Chemical Thermodynamics", NTH, Trondheim, Norway (1977), pp. 24, 25, Volume 2.

86. F.P. Buff, J. Chem. Phys., 25, 146 (1956).

87. F.P. Buff and Howard Saltsburg, ibid, 26, 23 (1957).

88. F.P. Buff and Howard Saltsburg, ibid, 26, 1526 (1957).

89. R.N. Wenzel. Ind. Eng. Chem., 28, 988 (1936).

90. A.B.D. Cassie and S. Baxter. Trans. Faraday Soc., 40, 546 (1944).

91. A.B.D. Cassie. Disc. Farad. Soc., 3, 11 (1948).

92. R.J. Good. J. Amer. Chem. Soc., 74, 5041 (1952).

93. A.W. Neumann and R.J. Good. J. Colloid Interface Sci., 38, 341 (1972).

94. J.D. Eick, R.J. Good and A.W. Neumann. J. Colloid Interface Sci., 53, 235 (1975).

95. J.J. Gilman. J. Appl. Phys., 31, 2208 (1960).

96. H. Udin, A.J. Shaler and J. Wulff. Trans. Met. Soc. AIME, 185, 186 (1949).

97. C.A. Ward and A.W. Neumann. J. Colloid Interface Sci., 49, 286 (1974).

98. A.W. Neumann, R.J. Good, C.J. Hope and M. Sejpal. J. Colloid Interface Sci., 49, 291 (1974).

99. S.K. Rhee. J. Amer. Ceramic Soc., 54, 376 (1971).

100. S.K. Rhee. J. Amer. Ceramic Soc., 53, 639 (1970).

101. J.G. Eberhart. J. Phys. Chem., 71, 4125 (1967).

102. H.D. Samarasekera and Z.A. Munir. J. Less-Common Metals, 64, 255 (1979).

103. L.A. Girifalco and R.J. Good. J. Phys. Chem., 61, 904 (1957).

104. S. Wu. J. Colloid Interface Sci., 71, 605 (1979).

105. D.T. Livey and P. Murray. J. Amer. Ceramic. Soc., 39, 363 (1956).

106. D. McCammond, A.W. Neumann and N. Natarajan. J. Amer. Ceramic Soc., 58, 15, 175.

107. A.S. Skapski, R. Billups and D. Casavant. J. Chem. Soc., 31, 1431 (1959).

108. J.B. Jones and A.W. Adamson. J. Phys. Chem., 72, 646 (1968).

109. J.W. Whalen and W.H. Wade. J. Colloid Interface Sci., 24, 372 (1967).

110. S.W. Mayer. J. Phys. Chem., 67, 2160 (1963).

111. S.W. Mayer. J. Chem. Phys., 40, 2429 (1964).

112. H. Reiss and S.W. Mayer, ibid, 34, 2001 (1961).

113. H. Reiss and S.W. Mayer and J.L. Katz, ibid, 34, 820 (1961).

114. G.J. Janz, "Proceedings of the third international symposium on molten salts", Edited by G. Mamantov, M. Blander and G.P. Smith. The Electrochemical Soc. Inc. (1982), pp. 52-67.

115. E.A. Guggenheim, "Mixtures", Oxford, London (1952).

116. B. Berge and J.L. Holm, Rapport til Norges Tekniske Hoegskoles Fond, NTH, Trondheim, Norway (1970).

117. J.G. Eberhart. J. Phys. Chem., 70, 1183 (1966).

118. G. Bertozzi and G. Sternheim. J. Phys. Chem., 68, 2908 (1964).

119. O.J. Kleppa and L.S. Hersch. Disc. Farad. Soc., 32, 99 (1961).

120. J. Goodisman. J. Colloid Interface Sci., 73, 115 (1980).

121. H.A. Johansen and S. May. Rev. Sci. Inst., 24, 1147 (1953).

122. R.H. Herz, "The Photographic Action of Ionizing Radiation", John Wiley and Sons (1969).

123. H. Harttig and K.J. Huttinger. J. Colloid Interface Sci., 78, 295 (1980).

124. Iwanami's Dictionary of Physics and Chemistry, 3rd edition, edited by Tamamushi et al., Iwanami Publishing Co., Tokyo (1976).

125. M. Yamamoto. Private communication, Toronto (1983).

126. S.J. Hitchcock, N.T. Carroll and M.G. Nicholas. J. Mat. Sci., 16, 714 (1981).

127. J.F. Oliver and S.G. Mason, ibid, 15, 431 (1980).

128. JANAF Thermochemical Tables, Second edition, D.R. Stull and H. Prophet et al., NSRDS-NBS 37 (1971). (Data was calculated by assuming ideal behaviour of KCl (or NaCl) in $PbCl_2$.)

129. T. Fujisawa and M. Yamamoto. Private communication, Toronto (1983).

130. G.E. Boyd and W.D. Harkins. J. Amer. Chem. Soc., 64, 1190 (1942).

131. L.A. Girifalco and R.A. Lad. J. Chem. Phys., 25, 693 (1956).

132. L.A. Girifalco, Ph.D. Thesis, University of Cincinnati (1954).

133. A. Bondi, "Spreading of Liquid Metals on Solid Surfaces: Surface Chemistry of High-Energy Substances", Chem. Rev., 52, 417 (1953).

134. C.B. Alcock, "Principles of Pyrometallurgy", Academic Press Inc. (London) Ltd. (1976).

135. F.L. Harding and D.R. Rossington. J. Amer. Ceramic Soc., 53, 87 (1970).

136. A. Gutierrez and J.M. Toguri. J. Chemical and Engineering Data, 27, 109 (1982).

POOR

QUALITY

ORIGINAL